

## Cavity quantum electrodynamics

This content has been downloaded from IOPscience. Please scroll down to see the full text.

2006 Rep. Prog. Phys. 69 1325

(<http://iopscience.iop.org/0034-4885/69/5/R02>)

View [the table of contents for this issue](#), or go to the [journal homepage](#) for more

Download details:

IP Address: 129.94.115.114

This content was downloaded on 30/09/2015 at 00:07

Please note that [terms and conditions apply](#).

# Cavity quantum electrodynamics

**Herbert Walther<sup>1</sup>, Benjamin T H Varcoe<sup>2</sup>, Berthold-Georg Englert<sup>3</sup> and Thomas Becker<sup>1</sup>**

<sup>1</sup> Max-Planck-Institut für Quantenoptik, Hans-Kopfermann-Str. 1 and Department of Physics, University of Munich, 85748 Garching, Germany

<sup>2</sup> Department of Physics and Astronomy, University of Sussex, Brighton, East Sussex BN1 9QH, UK

<sup>3</sup> Department of Physics, National University of Singapore, Singapore 117542, Singapore

E-mail: [herbert.walther@mpq.mpg.de](mailto:herbert.walther@mpq.mpg.de)

Received 10 February 2006

Published 3 April 2006

Online at [stacks.iop.org/RoPP/69/1325](http://stacks.iop.org/RoPP/69/1325)

## Abstract

This paper reviews the work on cavity quantum electrodynamics of free atoms. In recent years, cavity experiments have also been conducted on a variety of solid-state systems resulting in many interesting applications, of which microlasers, photon bandgap structures and quantum dot structures in cavities are outstanding examples. Although these phenomena and systems are very interesting, discussion is limited here to free atoms and mostly single atoms because these systems exhibit clean quantum phenomena and are not disturbed by a variety of other effects. At the centre of our review is the work on the one-atom maser, but we also give a survey of the entire field, using free atoms in order to show the large variety of problems dealt with. The cavity interaction can be separated into two main regimes: the weak coupling in cavity or cavity-like structures with low quality factors  $Q$  and the strong coupling when high- $Q$  cavities are involved. The weak coupling leads to modification of spontaneous transitions and level shifts, whereas the strong coupling enables one to observe a periodic exchange of photons between atoms and the radiation field. In this case, atoms and photons are entangled, this being the basis for a variety of phenomena observed, some of them leading to interesting applications in quantum information processing. The cavity experiments with free atoms reached a new domain with the advent of experiments in the visible spectral region. A review on recent achievements in this area is also given.

(Some figures in this article are in colour only in the electronic version)

## Contents

	Page
1. Introduction	1327
2. Modification of the spontaneous emission rate (weak coupling—real transitions)	1328
3. Modification of atomic energies in confined space (weak coupling—virtual transitions)	1329
4. Oscillatory exchange of photons between an atom and a cavity field (strong coupling)— the one-atom maser or micromaser	1334
4.1. Experimental set-up of the one-atom maser	1337
4.2. One-atom maser as a source of non-classical light	1338
4.3. Review of experiments on basic properties of the one-atom maser	1340
4.4. Statistics of detector clicks	1343
4.5. Trapping states	1344
4.6. Trapping state stabilization	1347
4.7. Fock states on demand	1350
4.8. Dynamical preparation of $n$ -photon states in a cavity	1352
4.9. The one-atom maser spectrum	1355
5. Other microwave cavity experiments	1357
5.1. Collapse and revival of the Rabi oscillations in an injected coherent field	1358
5.2. Atom–photon and atom–atom entanglement	1358
5.3. Atom–photon phase gate	1359
5.4. Quantum nondestructive-measurement of a photon	1359
5.5. Wigner function of a one-photon state	1359
5.6. Multiparticle entanglement	1359
5.7. Schrödinger cats and decoherence	1360
6. Slow atoms	1360
6.1. Jaynes–Cummings dynamics for slow atoms	1360
6.2. The maser	1365
7. Cavity QED experiments in the visible spectral region	1367
7.1. The one-atom laser	1368
7.2. Atoms pushed by a few photons	1369
7.3. Single-photon sources	1371
7.4. Single-atom laser using an ion trap	1372
8. Conclusions and outlook	1375
Acknowledgments	1377
References	1377

## 1. Introduction

The quantization of the electromagnetic field in quantum electrodynamics is in general achieved by starting with a finite volume defined by conducting walls where the field appears in a discrete, though infinite, set of modes (see, for example, [1]). Introducing canonical variables casts the Hamiltonian into a form similar to that for the harmonic oscillator which can easily be quantized by imposing canonical commutation relations. Finally, the customary continuous spectrum results when the volume is increased to infinity. For a long time this continuous and unlimited spectrum of the electromagnetic field has been exclusively considered. To obtain solutions for actual physical problems, the formalism of quantum field theory together with all its potentials to overcome divergences had to be developed.

For some time the modification of atomic properties in the presence of conducting walls has been gaining considerable interest. Introducing conductors into a physical system imposes boundary conditions on the electromagnetic field and leads back to a discrete spectrum in the case of a finite volume enclosed in a cavity. In principle, there are two distinct cases to be discussed. The first is the situation of an atom in close proximity to a conducting plate [2–6]. An oscillating atomic dipole induces image charges on the surface leading to a van der Waals type force adding up to the inner atomic forces, thus leading to position-dependent level shifts. Second, there are, in addition to these direct effects, the retarded phenomena from a discrete mode structure of the electromagnetic field inside a cavity due to its geometry. Of course, it is not possible to consider one of these phenomena without the other, but in most cases only one of the two produces the major influence.

In what follows, we restrict our attention to the effects of the discrete mode structure of a cavity; this means we limit our discussion to the retarded case. The related phenomena are usually summarized under the field of cavity quantum electrodynamics. The effects observed are

- (a) modification of the spontaneous emission rate of a single atom in a resonant cavity,
- (b) modification of the energy levels of atoms (modification of the Lamb shift) and
- (c) oscillatory energy exchange between a single atom and the cavity mode, showing pure quantum behaviour such as, for example, the disappearance and revival of Rabi nutation induced in a single atom by a resonant field.

The phenomena under (a) and (b) can be observed in weak coupling between radiation and atom, whereas case (c) requires strong coupling in the ideal situation. The strong coupling is characterized by the fact that a real and periodic photon exchange occurs between the cavity field and the atom during the interaction time. In case (a) a real photon is emitted and absorbed by the surrounding cavity before it can interact with the atom again, whereas in case (b) a virtual interaction affects the atomic system.

The situation for the experimental observation of those phenomena has drastically changed since frequency-tuneable lasers have become available, making it possible to create large populations of highly excited atomic states characterized by a high principal quantum number  $n$  of the valence electron. These states are generally called Rydberg states since their energy levels can be described by the simple Rydberg-type formula. Such excited atoms are very well suited to observing quantum effects in radiation–atom coupling for three reasons. Firstly, the states are very strongly coupled to the radiation field (the induced transition rates between neighbouring levels scale as  $n^4$ ); secondly, transitions are in the millimetre wave region so that low-order mode cavities can be made large enough to allow rather long interaction times; finally, Rydberg states have relatively long lifetimes with respect to spontaneous decay [7,8]. In recent years, it has also become possible to use optical cavities with extremely small volume

for these experiments so that resonance transitions of atoms also can now be investigated. Such experiments will also be discussed in this review.

The strong coupling of Rydberg states to the radiation resonant with transitions to neighbouring levels can be understood in terms of the correspondence principle: with increasing  $n$  the classical evolution frequency of the highly excited electron becomes identical with the transition frequency to the neighbouring level. The atom can therefore be seen as a large dipole oscillating with resonance frequency; the dipole moment is very large since the atomic radius scales as  $n^2$ .

Historically, cavity QED started when Purcell published an abstract of a paper presented at the 1946 Spring Meeting of the American Physical Society [9]. It dealt with transitions in nuclear magnetic resonance where the spins were coupled to a resonance circuit, and he showed that the spontaneous emission probability is increased by a factor  $3Q\lambda^3/4\pi^2 V$ , where  $Q$  is a quality factor and  $V$  the volume of the resonator. For  $V \approx \lambda^3$  the increase in the emission probability corresponds roughly to the quality factor of the resonator. The influence of the vacuum field on atoms is well summarized and described in a book on quantum electrodynamics by Power [10]. The first experimental work on inhibited spontaneous emission was done by Drexhage, Kuhn and Schäfer (the work is reviewed in [4]). In this work, the fluorescence of a thin dye film near a mirror was investigated. A reduction in the fluorescence decay by up to 25% results from the standing-wave pattern near the mirror. Much later, similar experiments were conducted by de Martini *et al* [11]. Early theoretical work on this has already been mentioned above.

This review is mainly focused on cavity quantum electrodynamics of free atoms because these systems provide the basis for the study of quantum phenomena in a very neat and largely unperturbed way. Cavity quantum electrodynamics in other systems such as, for example, semiconductor devices is mentioned but not treated in detail.

In the following, we would like to start with a brief review of the experiments on the modification of the spontaneous transition rate in confined space.

## 2. Modification of the spontaneous emission rate (weak coupling—real transitions)

In order to understand the modification of the spontaneous emission rate in an external cavity, we have to remember that in quantum electrodynamics this rate is determined by the density of modes of the electromagnetic field at the atomic transition frequency  $\omega_0$ , which depends on the square of the frequency. If the atom is not in free space but in a resonant cavity, the continuum of modes is changed into a spectrum of discrete modes, as discussed above, whereby one of them may be tuned into resonance with the atom. The spontaneous decay rate of the atom in cavity will then be enhanced in relation to that in free space by a factor given by the ratio of the corresponding mode densities [9] (see also the discussion above in connection with the proposal of Purcell):

$$\gamma_c/\gamma_f = \rho_c(\omega_0)/\rho_f(\omega_0) = 2\pi Q/V_c\omega_0^3 = Q\lambda_0^3/4\pi^2 V_c, \quad (2.1)$$

where  $V_c$  is the volume of the cavity and  $Q$  is the quality factor of the cavity, which expresses the sharpness of the mode. For low-order cavities in the microwave region one has  $V_c \approx \lambda_0^3$ , which means that the spontaneous emission rate is increased by roughly a factor of  $Q$ . However, if the cavity is detuned, the decay rate will decrease. In this case, the atom cannot emit a photon, since the cavity is not able to accept it, and therefore the energy has to stay with the atom.

In order to demonstrate experimentally the modification of the spontaneous decay rate, it is not necessary to consider single-atom densities in both cases. The experiments where spontaneous emission is inhibited can also be performed with large atom numbers. However,

in the opposite case, when the increase in the spontaneous rate is observed, a large number of excited atoms may disturb the experiment by induced transitions. The first experimental work on inhibited spontaneous emission by Drexhage, Kuhn and Schäfer (for a review see Drexhage [4]) has already been mentioned above. Inhibited spontaneous emission was also observed by Gabrielse and Dehmelt [12]. In these neat experiments, with a single electron stored in a Penning trap, they observed that cyclotron orbits show lifetimes which are up to 10 times as large as that calculated for free space. The electrodes of the trap form a cavity which decouples the cyclotron motion from the vacuum radiation field leading to a longer lifetime. Experiments with Rydberg atoms on inhibition of spontaneous emission have been conducted by Hulet *et al* [13] and Jhe *et al* [14]. In the latter experiments a  $3.4\ \mu\text{m}$  transition was suppressed. The experiment by Hulet *et al* follows a much earlier proposal by Kleppner [15].

The first observation of enhanced atomic spontaneous emission in a resonant cavity was published by Goy *et al* [16]. This experiment was conducted with Rydberg atoms of sodium excited in the 23s state in a niobium superconducting cavity resonant at 340 GHz. Cavity tuning-dependent shortening of the lifetime was observed. The cooling of the cavity had the advantage of totally suppressing the black-body field. The latter effect is completely absent if optical transitions are observed. The first experiments on optical transitions were conducted by Feld and collaborators [17, 18]. They succeeded in demonstrating the enhancement of spontaneous transitions even in higher-order optical cavities.

In modern semiconductor devices both electronic and optical properties can be tailored with a high degree of precision. Electron-hole systems producing recombination radiation analogous to radiating atoms can therefore be localized in cavity-like structures, e.g. in quantum wells. Optical microcavities of half or full wavelength size are thus obtained. Both suppression and enhancement of spontaneous emission in semiconductor microcavities were demonstrated in experiments by Yamamoto and collaborators [19]. Similar structures were used by Yablonovitch *et al* [20–22], exhibiting a photonic band gap with spontaneous emission forbidden in certain frequency regions.

### 3. Modification of atomic energies in confined space (weak coupling–virtual transitions)

In the previous section, we focused on changes in radiation rates of atoms near conducting walls or in cavity-like structures. We now discuss the more subtle phenomenon of energy shifts. While radiation rates are modified by the component of the field in phase quadrature with the atomic dipole, energy shifts are caused by the dispersive part of the interaction or, in other words, by the field part in phase.

Resonant and nonresonant phenomena have to be distinguished. The resonant self-energy shift of a decaying atomic dipole in the vicinity of a conducting wall can be determined from the average polarization energy produced by the image dipole field. For distances  $z$  comparable to the wavelength the near-field condition is satisfied, resulting in the  $z^{-3}$  dependence of the static dipole–dipole interaction characteristic for the van der Waals energy; under far field conditions the distance dependence is given by  $z^{-4}$ . The polarization of the atom by the nonresonant parts of the broadband electromagnetic field causes energy shifts, the Lamb shift being the most prominent one. In the spirit of the nonrelativistic treatment by Bethe [23] we can describe the major contribution of that shift as being a result of the emission and reabsorption of virtual photons. It is plausible that just as the real emission of a photon is modified in confined space, so also is the virtual process. The latter ‘real’ radiation energy shift is thus a consequence of vacuum fluctuations only. It is identical with the energy shift predicted by Casimir and Polder [24] and is analogous to the better-known result of Casimir [25] on the force between two plane neutral conducting plates.

The question of modification of atomic energies in confined space has recently found considerable interest and many calculations of the phenomenon have been made (for reviews see [26, 27]). Direct application to the energy shift of Rydberg atoms, which are of special interest for experimental studies, such as the one discussed below, was performed by Barton [28]. In that paper, the direct electrostatic interaction with a conducting wall and the radiation-induced (retarded) effects was estimated. The result is that in the case of two parallel plates the electrostatic effect is dominant when the distance  $L$  between the conducting plates is small,  $L < n^3 a_0 / \alpha$  ( $n$  is the principal quantum number,  $a_0$  the Bohr radius and  $\alpha$  the fine-structure constant), and the radiative effect plays a major role when large distances are used,  $L > n^3 a_0 / \alpha$ .

Experiments to measure the transition from the van der Waals type energy shift to the Casimir–Polder shift have been performed by the Hinds group [29, 33]. The results demonstrate reasonably well the change from a  $1/z^3$  to a  $1/z^4$  dependence of the energy shift.

Since the pioneering work of Casimir and Polder [24, 25] many authors have tried to improve the understanding of vacuum effects; particularly, shifts in atomic energy levels in a parallel-plate geometry have been calculated [28, 30–32], some of which have already been mentioned above. The amount of theoretical work available is in contrast to the total absence of efforts on the experimental side, even though the planar cavity is considered to be the prototype geometry. Its special feature is the extreme selectivity of the wave vectors  $\mathbf{k}$  and the creation of a field cutoff frequency  $\nu_{\text{cutoff}}$  for a particular polarization, with the result that only a discrete spectrum of the radiation field with frequencies greater than  $\nu_{\text{cutoff}}$  is present inside the cavity. The modification of the field between two parallel plates allows one to isolate the contribution to the atomic frequency shift resulting from a single  $\mathbf{k}$ . This modification is resonantly enhanced when the plate distance reaches either  $d = \lambda_0/2$  (cutoff) or small odd multiples of  $\lambda_0/2$ , where  $\lambda_0$  is the transition wavelength to a neighbouring atomic level. The restriction of the measurement to a particular contribution presents a special challenge owing to the tiny level shift expected.

There have been experimental attempts to determine radiative shifts for other cavity geometries [18, 33, 34]. In [18], a low- $Q$  concentric resonator was used to observe a resonant frequency shift of 1 MHz in the fluorescence spectra of an optical transition of Ba atoms inside the resonator. The experiment of Hinds *et al* [33], where ground-state Na atoms were transmitted through a wedge, has already been mentioned above. From the atomic opacity of the wedge the authors derived information on the potential and used that to determine the energy shift. In [34] the authors used an open resonator with curved mirrors. The shift obtained from the dispersive interaction between superpositions of circular states in Rb was measured for different cavity detunings. Although the experiment was carried out at low temperature, the outcome included a non-negligible thermal influence which had to be corrected.

In the following, we describe an experiment performed in our laboratory [35] using two plane copper plates to modify the vacuum field. Rydberg atoms are suitable probes since the transitions to neighbouring levels are in the microwave region, resulting in a resonant plate distance in the mm range. With the analysis limited to atomic states between 20S and 30S, these atomic level changes are expected to be a few hundred hertz when thermal radiation at room temperature is additionally present within the cavity and is resonantly coupled to the relevant Rydberg transition. In a cavity without thermal radiation the effect is only of the order of 100 Hz [28, 31, 32]. Measurement of these cavity-induced resonances were the main aim of the work described in the following.

The spectroscopic technique involves Doppler-free two-photon absorption in combination with the method of successive oscillatory fields [36]. This high-precision spectroscopy needed to measure the expected small shifts requires a highly frequency-stabilized laser system. It is based on the phase modulation method and has a residual frequency noise on the hertz level [37].

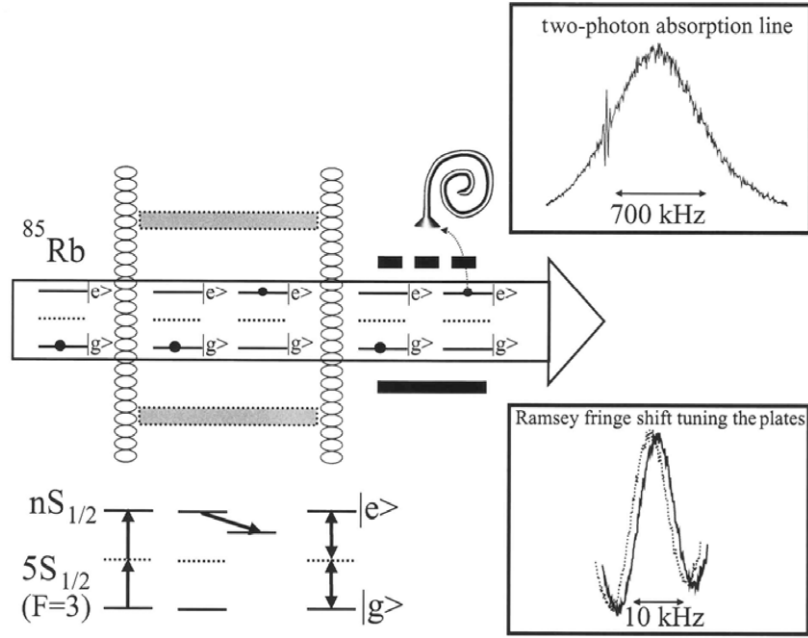


**Figure 1.** Scheme of the experimental set-up. The plate structure is placed between the two laser beams crossing the atomic beam in the vertical direction. The laser beams form a standing-wave field. The field ionization region is located downstream from the second laser beam. The insets on the right side show the Doppler-free two-photon absorption line with the Ramsey fringe (top) and the displacement of the Ramsey fringe on changing the plate distance (bottom). Note that the Ramsey fringe is not in the centre of the two-photon absorption line because of its different ac Stark shift (measured to be 8 Hz for a reference intensity of  $1 \text{ W cm}^{-2}$ ) compared with that of the Ramsey peak (220 mHz for the same reference intensity). This difference results from the fact that in the Ramsey two-field method the atom passes through the laser-free region most of the time. This figure is taken from [35].

The experimental scheme is shown in figure 1 [35, 38]. A beam of rubidium atoms is produced via an atomic oven collimated via liquid-nitrogen-cooled circular apertures located approximately 2.6 cm from the first laser interaction region formed by a standing wave.  $^{85}\text{Rb}$  atoms are excited into a superposition of the  $5S_{1/2}$  ground state and the  $nS_{1/2}$  excited state with  $n \geq 22$ . Afterwards the beam passes through the centre of the region containing the plate structure (grey rectangles in the picture) and then enters the second interaction region. Both excitations are in the low-saturation regime. After the second standing-wave laser field the atoms are detected by field ionization, with the ejected electron being multiplied by means of a channeltron. A spectrum is recorded by counting the channeltron pulses via a computer which also controls the laser frequency. The field ionization region is within a Faraday cage. This ensures that no electric fields from there can leak into the region with laser interaction and plate structure. Additionally, the whole area is shielded from external electric and magnetic fields by a copper tube surrounded by two layers of mu metal. The copper tube is in contact with a cryostat that can be cooled to either 77 or 4 K. Inchworms (piezo-driven devices) can move the plates perpendicularly to the direction of the atomic beam in a precise and reproducible manner which allows exact symmetric positioning of the plates relative to the beam. The interplate distances, ranging from 0.5 to 3 mm, can be monitored by means of an interferometric measuring device with a maximum uncertainty of  $\pm 1 \mu\text{m}$ .



Besides the careful shielding of external fields, it is also necessary to avoid any potential differences between the plates. To eliminate any shift from contact potentials, the two plates and their connection via thin and deformable lamellas were machined from a single piece of copper. To avoid adsorbates, the plates could be baked during the preparation stage of the experiment.

A folded optical resonator with active stabilization provided a stable phase between the two Ramsey zones. This was achieved by a piezo-mounted mirror and the phase modulation method (similarly to the method used to stabilize the dye laser). Additionally, the resonator enhanced the laser power in the two interaction zones.

Scanning the laser frequency and detecting the excited-state atoms reveal a two-photon peak with Ramsey fringes, as displayed in the upper inset of figure 1. The width of the central peak of the Ramsey structure is limited by the time of flight between the two zones. The mean time of flight was  $28 \mu\text{s}$ , which is slightly greater than the lifetime of the excited Rydberg states. Only the zero-order fringe is seen because a thermal atomic beam source was used, and higher-order fringes were therefore washed out owing to the longitudinal velocity distribution. The position of this Ramsey fringe was monitored as a function of the relative distance between the plates.

The experimental protocol was as follows. The plates were initially set at a position which served as a reference distance  $d_{\text{ref}}$  and the laser frequency was scanned across the central Ramsey fringe. Then the plates were moved to a new distance  $d$  and the laser was scanned again. This process was reiterated for other distances  $d$  relative to the same reference distance  $d_{\text{ref}}$ . The central fringe position was determined by a least-squares fitting routine which detected the peak centre with an accuracy between approximately 20 and 100 Hz, depending on the Ramsey fringe contrast, which was limited by the background pressure at different temperatures.

Careful control of the drift of the reference frequency (which is provided by the supercavity in the locking scheme of the dye laser) in the course of the measurement had to be exercised. Because the measurement of the level shift is given relative to a reference frequency, its drift has to be considered. Although there were two temperature isolation stages, the residual thermal length change of the supercavity resulted in a drift ranging between zero and  $100 \text{ Hz s}^{-1}$ . A measure of this drift as a function of time could be derived from the data obtained from the Ramsey spectra at the plate distance  $d_{\text{ref}}$ .

Retardation effects in the interaction of the atomic dipole with the cavity walls are dominant only when the distance between the plates is larger than the wavelength of the relevant Rydberg transition, i.e.  $d > n^3 a_0 / \alpha$ , where  $n$  is the principal quantum number,  $a_0$  the Bohr radius and  $\alpha$  the fine-structure constant. In this regime the round-trip time for a photon leaving the atom, reaching the cavity walls and returning to the atom is larger than the oscillation period of the relevant transition, and the shift is caused by the interaction of the atom with the cavity field. In the opposite case,  $d < n^3 a_0 / \alpha$ , the atom would interact with its mirror image in the cavity walls, giving rise to a van der Waals interaction. Therefore, the condition  $d > n^3 a_0 / \alpha$  has to be satisfied.

It is important to investigate the temperature influence on the energy shift in order to discriminate the thermal and vacuum contributions to the shift itself. This aim was pursued by scanning the plates at three different temperatures  $T = 292, 77$  and  $4 \text{ K}$  over interplate distances close to  $d_{\text{res}} = 3\lambda_0/2 = 1.173 \text{ mm}$ , where  $\lambda_0$  is the wavelength associated with the transition  $24\text{S}_{1/2} \rightarrow 23\text{P}_{3/2}$ . The average number of thermal photons,  $n_{\text{th}}$  per mode, is slightly above 15 at room temperature and thus a large thermal content is expected, whereas at  $T = 4 \text{ K}$ ,  $n_{\text{th}}$  is only 0.01.

Of special interest are the level shifts at low temperature. Two different experiments using the transitions  $22\text{S}_{1/2} \rightarrow 21\text{P}_{3/2}$  and  $26\text{S}_{1/2} \rightarrow 25\text{P}_{3/2}$  were prepared at  $4 \text{ K}$ . The frequency

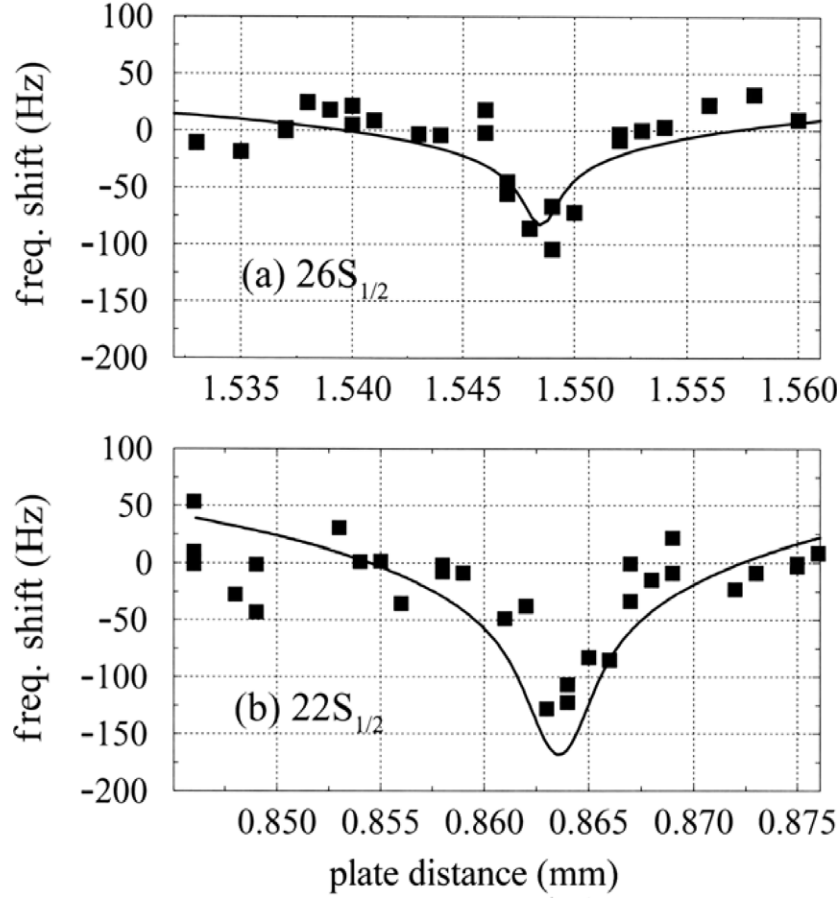


**Figure 2.** Comparison of the level shift with theory for two different transitions resonantly coupled into the cavity at  $T = 4$  K: (a)  $26S_{1/2} \rightarrow 25P_{3/2}$  and (b)  $22S_{1/2} \rightarrow 21P_{3/2}$ .

shift as a function of the plate distance for both cases is shown in figure 2. The resonance corresponding to  $3/2$  of the wavelength of the transition  $26S_{1/2} \rightarrow 25P_{3/2}$  has a peak value of about 100 Hz. In figure 2(b) the measured resonance for the level  $22S_{1/2}$  shows a shift of 120 Hz.

The theoretical treatment of quantum electrodynamic level shifts between parallel conducting plates in resonance with atomic transitions is very involved. According to [28,31,32,39] the relevant dependences of the shift  $\Delta$  on the distance and principal quantum number  $n$  are given (in atomic units) by the approximate formula

$$\Delta \approx \frac{4\alpha^2}{3d} \sum_{n' < n} E_{n'n}^2 R_{n'n}^2 \ln \left\{ 2 \left[ \cos^2 \left( \frac{E_{n'n}d}{2\hbar c} \right) + \Gamma^2 \right]^{1/2} \right\}, \quad (3.1)$$

where  $E_{n'n}$  is the energy difference between the states  $n$  and  $n'$ , and  $R_{n'n}$  is the radial matrix element between the same states.  $\Gamma = \sinh(\beta/2)$  expresses the damping due to the attenuation of the field upon one reflection so that  $\beta = -\ln(\rho/2)$ , with  $\rho$  being the reflectivity of the mirrors. In equation (3.1) the main contribution to the shift comes from the transitions to the first neighbouring levels and, because  $E_{n'n}^2 \approx 1/n^6$  and  $R_{n'n}^2 \approx n^4$ , the changes in  $\Delta$  with

$n$  and  $d$  are then given (in Hz) approximately by

$$\Delta \approx \frac{2.47 \times 10^4}{n^2 d} \ln \left\{ 2 \left[ \cos^2 \left( \frac{E_{n'n} d}{2\hbar c} \right) + \Gamma^2 \right]^{1/2} \right\}, \quad (3.2)$$

where  $d$  is measured in mm. On resonance the argument of the cosine function approaches  $\pi/2$  and equation (3.2) contains a logarithmic divergence, which is smoothed to a finite value by the imperfect reflectivity of the copper mirrors [39]. The curves in figure 2 are drawn by averaging equation (3.2) over a Gaussian distribution of the interplate distances. The standard deviations have been determined to be roughly 0.5 and 1  $\mu\text{m}$  for the 26S and 22S states, respectively, thereby reflecting the different values of the uncertainty in the distance determination owing to the different driving distances of the piezo motors in the two measurements. The frequency-dependent reflectivities were calculated from the copper conductivity at 4 K to be better than  $R = 0.9999$ . With these parameters the agreement between theory and experiment is satisfactory. The widths of the experimental resonances are also well reproduced. There is a further correction due to the finite size of the atomic beam diameter  $\Phi$  relative to the transition wavelength  $\lambda_0$  ( $\Phi/\lambda_0 = 0.26$  for the 22S state and 0.15 for the 26S state). This correction should affect more the calculation for the 22S state as a result of a pointlike beam approximation assumed in equation (3.1). Although the model described is based on a QED approach, one should be aware of the fact that part of the effect investigated here might also be understood in terms of classical arguments [39].

It is interesting to emphasize that the method described here is suitable for probing the effect of particular frequencies of the vacuum spectrum on the level shift. The shifts measured for vanishing thermal photon numbers for the states  $22\text{S}_{1/2}$  and  $26\text{S}_{1/2}$  show good agreement with theory.

In recent years quite a few experiments on the Casimir force between macroscopic objects have been conducted. These experiments are remarkable insofar as they allow a quantum electrodynamic effect to be measured with a classical macroscopic apparatus where no atom or quantum particle is involved [40–43]. The experiments were conducted for a distance between the objects ranging from 0.1 to 6  $\mu\text{m}$ . The first two experiments measured spherical objects against a plate [40, 41] and the third one measured the force between two plates [42]. In the paper by Chen and Mohideen [43] the lateral Casimir force is determined. For this purpose the force between a sinusoidally corrugated gold-coated plate and a large sphere was determined. The agreement between experiment and theory in all these experiments is in the per cent range, which is remarkable in view of the fact that these experiments are very difficult.

#### 4. Oscillatory exchange of photons between an atom and a cavity field (strong coupling)—the one-atom maser or micromaser

The single-mode radiation field of the one-atom maser [48], or *micromaser*, is the prototype of an open driven quantum system. It has been successfully used for studies—both experimental and theoretical—of the quantum interaction between two-level Rydberg atoms and one privileged microwave mode of the radiation field.

In a one-atom maser (or laser)<sup>4</sup>, simple two-level atoms are strongly coupled to a single mode of the radiation field that is resonant, or nearly resonant, with the atomic transition. This situation is described by the Jaynes–Cummings Hamiltonian [44],

$$H = \hbar\omega a^\dagger a + \hbar(\omega + \Delta)\sigma^\dagger \sigma - \hbar g(t)(a^\dagger \sigma + \sigma^\dagger a), \quad (4.1)$$

<sup>4</sup> For laser see section 7.1.

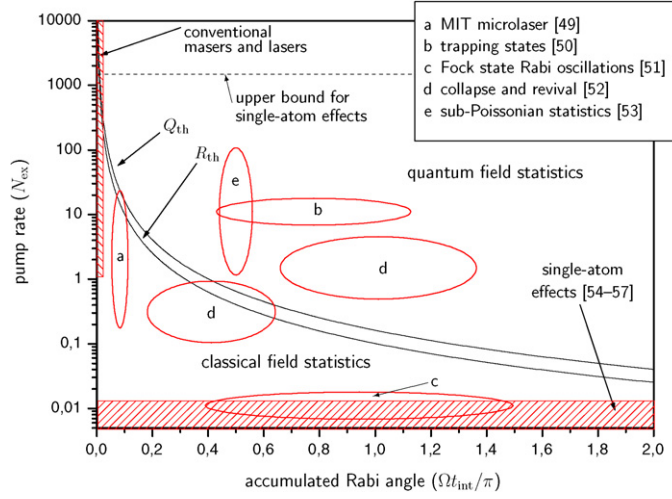


**Figure 3.** Parameter space accessible in cavity QED for single-atom masers and lasers. The lines denoted  $R_{th}$  and  $Q_{th}$  indicate the threshold pump rates of a one-atom maser/laser for building a true maser field and the pump rate for which this field acquires quantum mechanical statistics. The thin region on the left axis shows the domain of the conventional maser or laser. Note that, typically, conventional sources operate with many atoms or molecules in the cavity at one time and thus the thresholds indicated do not strictly apply. The ellipse-shaped regions indicate in a rough manner the range of parameters achieved for the respective references. The experiments in the optical region described in chapter 7 operate with a very large accumulated Rabi angle and are outside the range of this plot.

where  $a$ ,  $a^\dagger$  are the photon annihilation and creation operators,  $\sigma^\dagger$  and  $\sigma$  are the raising and lowering operators of the atomic transition and  $g(t)$  is the time-dependent coupling strength between the atomic transition and the cavity mode. The frequency of the cavity mode is  $\omega$  and the atomic transition differs from this by the detuning  $\Delta$ . The time dependence of  $g(t)$  originates in the passage of the atom through the resonator. Typically, the simple form,

$$g(t) = \begin{cases} 2\Omega & \text{for } t_0 < t < t_0 + t_{int}, \\ 0 & \text{otherwise,} \end{cases} \quad (4.2)$$

describes matters sufficiently well. Here  $\Omega$  is the (effective) Rabi frequency,  $t_0$  is the instant when the atom in question enters the cavity and  $t_{int}$  is the duration of the interaction.

Although several experiments have been published in which the strong coupling between atoms and a single cavity mode is exploited (see, for example, the review papers [67], [68], [45] and [46] published in 1994, 1995 and 1999, respectively), the micromaser [48] is the only strongly coupled system in which a steady-state quantum field has been created with single atoms or less simultaneously in the cavity. The experiment on the realization of the two-photon maser-oscillator [47] also produces a steady-state field; however, the average number of atoms at threshold is about five. Excited-state atoms entering the cavity drive the micromaser field, each atom contributing to the quantum cavity field. Above the threshold of maser action, the steady-state field can be strongly non-classical.

A map of atom cavity systems is shown in figure 3, a pictorial summary of the data in table 1 (the CalTech experiments [58], [140] or [149] and other experiments described in chapter 7 are beyond the parameter range covered by the figure except for the MIT microlaser experiment). This map compares two features of these systems, the normalized pump rate ( $N_{ex}$  = average number of atoms traversing the resonator during one photon lifetime) and the product  $\Omega t_{int}$ , the

**Table 1.** Parameters of the various experiments summarized in figure 3.

				Coupling			
	Atomic flux rate ( $\text{s}^{-1}$ )	Photon lifetime (ms)	Interaction duration $t_{\text{int}}$ ( $\mu\text{s}$ )	$\Omega/\pi$ (kHz)	Accumulated Rabi angle $\Omega t_{\text{int}}/\pi$	Normalized flux $N_{\text{ex}}$	
a	MIT microlaser [49]	$7.62 \times 10^5 - 7.62 \times 10^6$	0.000 837	0.131	110	0.092	0.64–6.4
b	Trapping states [50]	50–75	200	14–110	14	0.509–1.40	10–15
c	Fock state Rabi oscillation [51]	0.333	30	40–140	14	0.509–1.78	0.01
d	Collapse and revival [52]	500	0.5	30–140	7	0.191–0.891	0.25
d	Collapse and revival [52]	500–3000	2	40–160	14	0.509–2.04	1–6
e	Sub-Poisson statistics [53]	5–300	200	35	14	1.4	1–60
	Single-atom effects [54–57] <sup>1</sup>	0.1–1	0–90	50	0–4		
	CalTech experiments [58] <sup>2</sup>	0.0001	0.3	14 400	4.3		

<sup>1</sup> Performed with pulsed excitation, so that the atomic flux rate and the normalized flux are ill-defined.

<sup>2</sup> Not indicated in figure 3 as well as other experiments described in chapter 7 (except for MIT microlaser).

Rabi phase accumulated during the interaction. Two lines are shown on this plot, indicating the threshold for a steady-state maser/laser field ( $R_{\text{th}}$ ) and the threshold for the appearance of quantum statistics ( $Q_{\text{th}}$ ). The one-atom maser or micromaser is currently the only experimental apparatus that distinctly passes the quantum threshold and enters the non-classical regime. The single atom laser recently described by Kimble and coworkers [149] also reaches the quantum limit. The quantum threshold strictly applies only to systems with only one atom at a time in the cavity, since collective atom effects act to destroy quantum effects (see, for example, [59]). A good definition of the upper bound is when the average number of atoms in the cavity exceeds 0.2. This line is shown in figure 3 for current micromaser parameters. For other experiments this line is more than two orders of magnitude lower. This shows that the very high  $Q$  factor of the micromaser cavity is the feature that allows a steady-state field to be generated with properties that can only be described by quantum mechanics. The cavity lifetime of the one-atom maser is more than two orders of magnitude larger than in other related experiments [60]. Work in the optical spectral region is being very actively pursued at the moment (see chapter 7). Furthermore, quantum dots embedded in a semiconductor micro-cavity [61–63] are another important field as well as semiconductor cavity systems [64].

An important feature of the one-atom maser is its ability to generate steady-state sub-Poissonian (and hence non-classical) fields in the cavity. The extreme sub-Poissonian state is a Fock state or number state. A Fock state is a state with a fixed number of photons and is maximally distant from what is typically known as a classical light field. These states are the quantum mechanical basis states of the electromagnetic field and are used in nearly all aspects of quantum optics. However, the extreme non-classical nature of these states has made them difficult to produce experimentally, and current sources are limited to the production of single photons [65] (see also chapter 7). The one-atom maser, with its high  $Q$  factor and hence long photon lifetime, is the most suitable experimental apparatus to produce such states, and their production has therefore been a major focus of recent work on this apparatus, culminating in many realizations with evidence of up to 5-photon Fock states. We will describe the micromaser in some detail and provide a review of the recent work on the production of Fock states.

Another regime that can be pursued in microwave cavity QED is that of dispersive measurements in which the off-resonant, rather than the resonant, interactions with the field

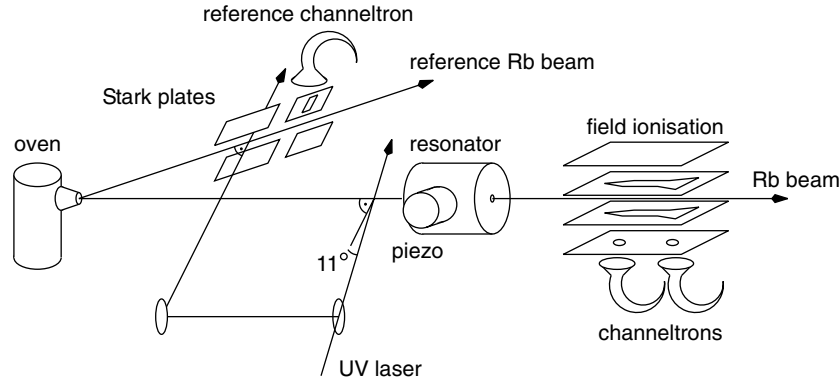


**Figure 4.** The one-atom maser apparatus; see text. (Reproduced from [70].)

are important. Work of this kind is only briefly covered in this review; more details of such measurements can be found in [67] and in section 5.4.

#### 4.1. Experimental set-up of the one-atom maser

The scheme of the experimental set-up of the one-atom maser used in our laboratory is displayed in figure 4. The first realization of the one-atom maser was described in [48]. The standard set-up of the one-atom maser employs the effusive output of a rubidium oven, which is collimated into two atomic beams: a central one passing directly into a  $^3\text{He}$ – $^4\text{He}$  dilution refrigerator and a second one directed to an auxiliary excitation region. The central beam passes through the superconducting niobium cavity and the state-selective field ionization apparatus housed in the cryostat. The superconducting cavity has a  $Q$ -factor of up to  $4 \times 10^{10}$ , which corresponds to an average lifetime of a photon in the cavity of 0.3 s [69]. The photon lifetime is therefore much longer than the interaction time of an atom with the maser field, being approximately 30–130  $\mu\text{s}$  for a thermal atomic beam, and therefore the atomic beam is sufficiently weak to make the probability of two atoms being in the cavity at the same time negligible.

The two-level transitions used in the experiments are between  $^{85}\text{Rb}$  Rydberg levels. The rubidium atoms are excited by laser excitation into the  $63\text{P}_{3/2}$  upper maser level. A frequency-doubled dye laser ( $\lambda = 297 \text{ nm}$ ) is used to excite the atoms to the Rydberg state from the  $5\text{S}_{1/2}$  ( $F = 3$ ) ground state. The lower maser level is either  $61\text{D}_{5/2}$  or  $61\text{D}_{3/2}$  for cavity frequencies of 21.456 GHz and 21.506 58 GHz and the vacuum Rabi frequencies of these transitions are 44 kHz and 20 kHz, respectively. Surface impurities in the cavity tend to alter the values of these parameters and therefore some calibration is required. In more recent experiments, trapping states (see below) have been used to provide accurate values of the parameters. Velocity selection is provided by angling the excitation laser towards the main atomic beam at  $11^\circ$  to the normal. The dye laser was locked, by means of an external feedback control [71], to the  $5\text{S}_{1/2}(F = 3)$ – $63\text{P}_{3/2}$  transition of the reference atomic beam excited at normal incidence. The exciting laser light from the frequency-doubled laser is linearly polarized and aligned with the linear polarization of the microwave cavity. Only transitions  $\Delta m = 0$  are thus allowed. This guarantees the two-level nature of the microwave interaction. For a recent paper on this fact see [72].

Tuning the laser, which changes the velocity of the beam and thus the interaction time, was performed by Stark shifting the resonance frequency with a stabilized voltage source. This enabled the laser to be tuned while remaining locked to an atomic transition.

Collective effects caused by the entry of more than one atom into the cavity reduce the appearance of quantum effects in the cavity field. An upper limit for the one-atom condition can be arbitrarily considered to be 0.2 atoms on average in the cavity. For a cavity decay time of 0.3 s this is the dashed line marked in figure 3 ( $N_{\text{ex}} = 1500$ ). Above this limit collective effects play an increasingly larger role in the maser dynamics and the detailed predictions of the theory become increasingly inaccurate [59, 73–76]. In fact, for some special conditions of strongly quantum mechanical states (for example, the trapping states discussed below) even this limit is too high. Some care therefore needs to be taken to ensure that these collective effects do not significantly influence the maser field statistics.

#### 4.2. One-atom maser as a source of non-classical light

In the typical operation of the one-atom maser, when collective effects can be ignored and the interaction time is much shorter than the cavity photon lifetime, the strategy to describe the one-atom maser is straightforward. While an atom flies through the cavity the coupled atom field system is described by the Jaynes–Cummings Hamiltonian (4.1) and during the intervals between the successive atoms the evolution of the field is governed by the master equation of a harmonic oscillator damped by a thermal bath. The derivation of the steady-state photon statistics has turned from a research topic [77, 78] to a textbook matter (see, for example, [79, 80]; while [81] is a tutorial on micromaser physics). The problem can be solved analytically, and one obtains the following probability for finding  $n$  photons in the cavity when the maser has reached the steady state:

$$P_n = P_0 \left( \frac{n_{\text{th}}}{1 + n_{\text{th}}} \right)^n \prod_{k=1}^n \left( 1 + \frac{N_{\text{ex}} \mathcal{A}_k}{k n_{\text{th}}} \right), \quad (4.3)$$

where  $\mathcal{A}_k = \sin^2(\Omega t_{\text{int}} \sqrt{k+1})$  is the emission probability and  $n_{\text{th}}$  is the thermal photon number. The normalized pump rate  $N_{\text{ex}}$  is the dimensionless parameter that is used in figure 3 to compare different operating conditions of the one-atom maser. It is given by  $N_{\text{ex}} = R \tau_{\text{cav}}$ , where  $R$  is the atomic rate and  $\tau_{\text{cav}}$  is the cavity photon lifetime. The probability of zero photons,  $P_0$ , is determined by normalization to unit total probability,  $\sum_{n=0}^{\infty} P_n = 1$ .

With the probabilities  $P_n$  at hand, one can calculate moments of the photon number, in particular the mean photon number  $\langle n \rangle$  and the variance  $\langle n^2 \rangle - \langle n \rangle^2$ . Following Fano [82] and Mandel [83], we use the normalized variance, the so-called  $Q$  parameter,

$$Q = \frac{\langle n^2 \rangle - \langle n \rangle^2}{\langle n \rangle} - 1, \quad (4.4)$$

as a convenient numerical measure of the photon number variance. A Poissonian distribution has  $Q = 0$ ; for  $Q < 0$  one speaks of a sub-Poissonian distribution and for  $Q > 0$  one has a super-Poissonian distribution. Figure 5 shows the normalized mean photon number ( $\langle n \rangle / N_{\text{ex}}$ ) and the normalized variance ( $Q$ ) as functions of (top) the interaction time of the atoms with the cavity photons and (bottom) the pump rate, which are the two experimentally variable parameters.

A parameter that provides a good qualitative comparison of different one-atom maser regimes is the so-called *pump parameter*, given by  $\Theta = \sqrt{N_{\text{ex}}} \Omega t_{\text{int}}$ . It is useful for locating features of the maser operating under a wide variety of conditions. For example, one can see in figure 5 that maxima of the  $Q$  parameter occur when  $\Theta$  is (roughly) a multiple of  $2\pi$ .

When the value of the pump parameter is  $\Theta = 1$ , the average photon number starts to rise steeply, the photon-statistical parameter  $Q$  reaches a local maximum and the one-photon probability  $P_1$  becomes larger than the no-photon probability  $P_0$  for the first time. This



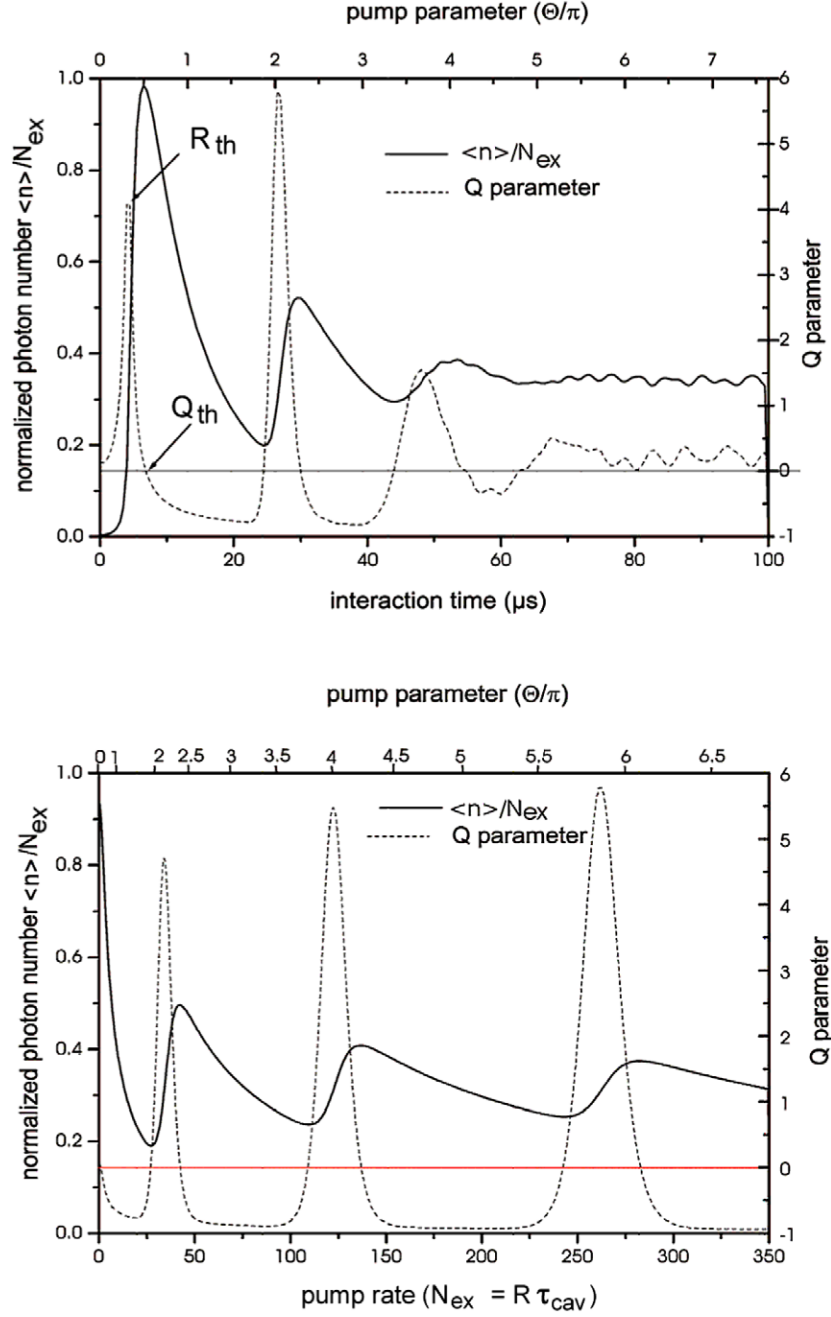


**Figure 5.** The pump curve of the one-atom maser as obtained from equation (4.3). In both the plots, the temperature is set at 0.5 K, which corresponds to  $n_{\text{th}} = 0.1$  thermal photons. Top: the normalized photon number as a function of the interaction time (bottom axis), for a pump rate  $N_{\text{ex}} = 40$ . Bottom: the normalized photon number as a function of the pump rate  $N_{\text{ex}}$  (bottom axis), for an interaction time  $t_{\text{int}} = 30 \mu\text{s}$ . The top axis of both plots shows the equivalent value of the pump parameter,  $\Theta$ , for these conditions (see text). The thresholds of maser action ( $R_{\text{th}}$ ) and quantum field statistics ( $Q_{\text{th}}$ ) are indicated. Note that the micromaser exhibits thresholdless behaviour for the parameters of the bottom plot.



point is therefore known as the *maser threshold*. Another position of interest is where the statistical parameter  $Q$  crosses zero for the first time. There the photon distribution passes from a classically shaped super-Poissonian distribution to a sub-Poissonian distribution. This quantum threshold lies at approximately  $\Theta = \pi/2$ . At this point nearly all atoms deposit photons in the cavity and the field has a Poissonian distribution with an average value equal to that of the atomic pump rate  $N_{\text{ex}}$ . Above this point the maser field becomes sub-Poissonian and therefore distinctly quantum mechanical, since the average energy in the cavity field is stabilized by the one-atom maser interaction. Some super-Poissonian peaks appear above this position; these are bistable points in which quantum jumps between two sub-Poissonian distributions occur. The statistics are therefore quantum mechanical in origin, even if they lie in a classical region. The atomic rate, as a function of the interaction time, required to cross the maser threshold and quantum thresholds are indicated in figure 3 by the lines  $R_{\text{th}}$  and  $Q_{\text{th}}$ , respectively.

The threshold for quantum behaviour is really only applicable to the single-atom regime in which the possibility of collective effects is very low. When collective effects cannot be ignored, the position of this line is somewhat modified. Moreover, while some basic parameters may still apply at this value, the upper bound of collective effects for more exotic states such as trapping states is considerably lower since they are completely obliterated by even low levels of collective effects.

Above the threshold ( $R_{\text{th}}$ ), the field in the cavity is a steady-state phenomenon and is thus available for study in some detail. Below threshold, the cavity field is dominated by cavity decay and is therefore a transient effect lasting for a cavity decay time after the interaction of the atom. This is the single-atom-effect region indicated in figure 3. As the evolution of the atom and cavity field is fully coherent, the atom and cavity field are entangled after their interaction. This entanglement is used, for example, to probe the cavity field in the normal operation of the maser. In the single-atom regime this can be exploited to create a transient field that exists in the cavity for a photon lifetime. As the atomic beam has a Poissonian distribution of arrival times, it can happen that, even in operation well below threshold, several atoms enter the cavity within a cavity decay time. Post-selective detection of such events has been used to observe the interaction of the field with up to three atoms under these conditions [51, 54–57].

#### 4.3. Review of experiments on basic properties of the one-atom maser

Atoms interacting with the cavity field undergo Rabi oscillations and their emission probability is determined by the accumulated Rabi phase when they leave the cavity. When the cavity field is initially in a coherent field state, the photon probability distribution is Poissonian, which results in dephasing of the Rabi oscillations causing their subsequent collapse. After collapse, the evolution of the atom and quantized cavity field results in a revival of the Rabi oscillations. These revivals occur periodically with a period determined by the square root of the average photon number. This phenomenon is known as ‘collapse-and-revival’ and is a purely quantum mechanical feature with no classical counterpart [84].

Collapse-and-revival can also occur in the case of a thermal Bose–Einstein field, where the spread in the photon number is much larger than that in the coherent state. In this case, the pattern of oscillations is more complicated, and the pattern never collapses quite completely—but this is also an inherently quantum mechanical phenomenon since the classical counterpart to this field would cause the oscillation to decay to zero with no revival at all. Collapse-and-revival in the presence of a thermal field was first observed by Rempe *et al* in 1987 [52]. Elmfors *et al* [85] subsequently performed a theoretical analysis of the experimental conditions

and found excellent agreement between theory and experiment, thus clearly showing that the interpretation of the data as collapse-and-revival was accurate. In 1996, collapse-and-revival was also observed in the presence of a coherent field by Brune *et al* [86] (see also section 5.1).

The coherent interaction of atoms with the cavity field produces non-classical states in the cavity. Figure 3 shows that over a wide range of interaction times a relatively low  $N_{\text{ex}}$  is sufficient to generate a non-classical maser field. This is the case because the vacuum field initiates transitions to the lower maser level. The sub-Poissonian statistics can be understood from figure 5, where the normalized average photon number  $\langle n \rangle / N_{\text{ex}}$  is shown on the right as a function of the pump rate  $N_{\text{ex}}$ . An increase in the photon number decreases the emission probability, driving the photon number to a smaller value. A decrease in the photon number, by contrast, increases the emission probability, driving the photon number up. This is a coherent interaction and is therefore a quantum mechanical stabilization of the photon number, producing sub-Poissonian statistics. As the atoms are the source of the field, the field statistics can be related to the atomic statistics in a systematic manner [87]. The observation of sub-Poissonian atomic statistics was reported by Rempe *et al* [53], and its relation to the sub-Poissonian photon distribution was first studied by Rempe *et al* [88] and later by Briegel *et al* [87].

The reason for the sub-Poissonian atomic statistics is as follows: a changing flux of atoms changes the Rabi frequency via the stored photon number in the cavity. Adjusting the interaction time allows the Rabi nutation cycle to be chosen such that the probability of the atoms leaving the cavity in the upper maser level increases when the flux, and hence the photon number in the cavity, is raised. This leads to sub-Poissonian atomic statistics since the number of atoms in the lower state decreases with increasing flux and photon number in the cavity. This feedback mechanism can be neatly demonstrated through the anticorrelation of atoms leaving the cavity in the lower state. The fact that anticorrelation is observed indicates that the atoms in the lower state are more equally spaced than expected for a Poissonian distribution of the atoms in the beam. This means that when, for example, two atoms in the upper state enter the cavity close to each other, the second one performs a transition to the lower state with reduced probability.

The interaction with the cavity field thus leads to an atomic beam with atoms in the lower maser level showing number fluctuations which are up to 40% below those of a Poissonian distribution usually found in atomic beams. This is interesting because atoms in the lower level have emitted a photon to compensate for cavity losses inevitably present. Although this process is induced by dissipation giving rise to fluctuations, the atoms still obey sub-Poissonian statistics. As discussed above, this can also be seen as a consequence of the quantum-non-demolition situation achieved in the region  $\Theta \approx 2\pi$  and multiples thereof.

The field strongly fluctuates at positions where phase transitions occur, these being caused by the presence of two maxima in the photon number distribution  $P(n)$  at photon numbers  $n_l$  and  $n_h$  ( $n_l < n_h$ ) (see figure 6). The phenomenon of two coexisting maxima in  $P(n)$  was also studied in a semiheuristic Fokker–Planck (FP) approach [77]. There, the photon number distribution  $P(n)$  is replaced by a probability function  $P(v, \tau)$  with continuous variables  $\tau = t/\tau_{\text{cav}}$  and  $v = n/N_{\text{ex}}$ , the latter replacing the photon number  $n$ . The steady-state solution obtained for  $P(v, \tau)$ ,  $\tau \gg 1$ , can be constructed by means of an effective potential  $V(v)$  showing minima at positions where maxima of the probability function  $P(v, \tau)$  are found. Close to  $\Theta = 2\pi$  and multiples thereof, the effective potential  $V(v)$  exhibits two equally attractive minima located at stable gain–loss equilibrium points of maser operation (see figure 6). The mechanism at the phase transitions is always the same: a minimum of  $V(v)$  loses its global character when  $\Theta$  is increased and is replaced in this role by the next one. This reasoning is a variation of the Landau theory of first-order phase transitions, with  $\sqrt{v}$  being

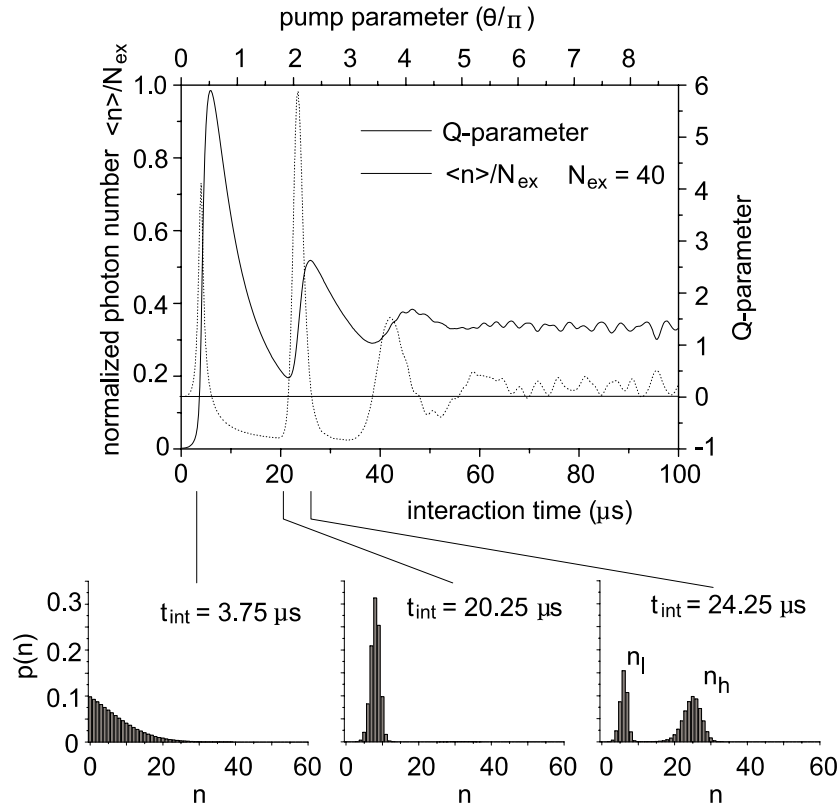


**Figure 6.** One-atom maser or micromaser characteristics. The upper part of the figure shows the average photon number versus interaction time (—) and the photon number fluctuations represented by the  $Q$ -factor (·····). In the lower part of the figure the steady-state photon number distribution  $P(n)$  is shown for three values of  $t_{int}$ . The distribution on the left side corresponds to the maser threshold and that on the right gives an example of the double-peaked distribution associated with the quantum jump behaviour. In this situation, the atom is back in the excited state and can again emit, leading to a higher steady-state photon number  $n_h$ . With increasing  $t_{int}$  this part will grow and  $n_l$  will decrease and disappear. A new jump occurs for pump parameters  $\theta > 3\pi$ .

the order parameter. This analogy actually leads to the notion that, in the limit  $N_{ex} \rightarrow \infty$ , the change of the micromaser field around integer multiples  $\Theta = 2\pi$  can be interpreted as first-order phase transitions [89].

Close to first-order phase transitions long time constants of the field evolution are expected. This phenomenon was experimentally demonstrated, along with related phenomena such as spontaneous quantum jumps among equally attractive minima of  $V(\nu)$ , bistability and hysteresis. Some of these phenomena are also predicted in the two-photon micromaser, for which qualitative evidence of first-order phase transitions and hysteresis has been reported. One example of this switching behaviour will be discussed in the following. The maser was operated under steady-state conditions close to a first-order phase transition. The two maxima in  $P(n)$  are manifested in spontaneous jumps of the maser field between the two maxima, with a time constant of 10 s. This fact, and the relatively large pump rate, led to the clearly observable field jumps shown in figure 7. The two discrete values of the counting rates correspond to the metastable operating points of the maser, these being ca 70 and ca 140 photons: these two values correspond to two equally attractive minima in the FP potential  $V(\nu)$ . If one considers, for

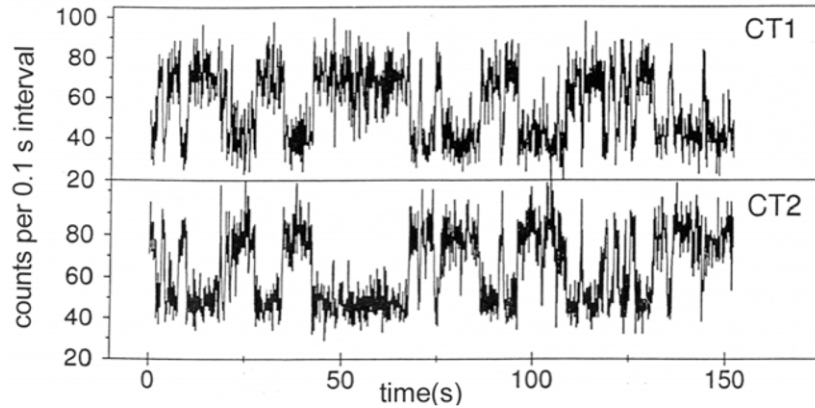


**Figure 7.** Quantum jumps between two equally stable operation points of the one-atom-maser field. CT1 is the measurement of the upper state atoms and CT2 that of the lower state atoms. It can be seen that both signals show counterphase behaviour.

instance, the counting rate of lower-state atoms (CT2 in figure 7), the lower (higher) plateaus correspond to time intervals in the low (high)-field metastable operating point. If the actual photon number distribution is averaged over a time interval containing many spontaneous field jumps, the steady-state result  $P(n)$  of the micromaser theory is recovered [89].

As noted above, between the regions of sub-Poissonian statistics, there are narrow regions of super-Poissonian statistics coinciding with thresholds in the photon number. These features are due to photon number phase transitions. In these regions, the steady-state photon distribution of equation (4.3) has two sub-Poissonian peaks that are well separated, so that the Fano–Mandel  $Q$  parameter is positive (and relatively large). A photon number distribution of this particular kind gives rise to quantum jumps between these two sub-Poissonian peaks. This effect and the associated bistability that one would expect from this system have indeed been observed in the one-atom maser [90, 91].

#### 4.4. Statistics of detector clicks

In these experiments all information about the radiation field is second-hand, inasmuch as the experimenter can examine only atoms emerging from the resonator but not the field itself. The Fock-state Rabi oscillations clearly show this. Although we do not measure the field itself, we are able to determine the photon distribution by analysis of an atom used as a probe of the field. Accordingly, in the steady-state maser dynamics, the atoms play a double role: (i) they pump the cavity and (ii) they provide the interaction diagnostics. The two roles interfere with one another because detection of the atom in a known final state leads to a quantum mechanical reduction of the photon state inside the resonator. Frequent detection is accompanied by quasi-permanent state reduction which can prevent the cavity field from relaxing to the steady state that would be reached if the atoms were left unobserved. Nevertheless, the steady-state properties determine the statistics of clicks recorded by atom detectors. This method of calculation has been used rather successfully for determining the photon distribution in the cavity in recent experiments [51, 92]. Furthermore, an extended analysis [93] predicts the probabilities of specific sequences of atoms (or, rather, of detector clicks) and therefore provides predictions of correlations between the internal state of the atoms that are successively detected in the field ionization zone. Measurement of these correlations therefore provides a

method of assessing the accuracy of the formalism, and then other predictions of the model, which cannot be readily observed, such as the presence of entanglement, can be trusted as well.

The so-called ‘damping-bases method’ [94] has been instrumental in extracting predictions about atomic correlations and observed photon distributions from one-atom-maser theory [95, 51, 92]. These correlations have recently been observed and the correspondence between theory and experiment determined [95]. The success of this correspondence strongly suggests that other aspects of the theory, such as predictions of multiple atom entanglement, are also true.

#### 4.5. Trapping states

Trapping states are a feature of steady-state operation of the one-atom maser, in which the field is peaked at a single photon number [69]. They occur in the one-atom maser as a direct consequence of the quantization of the cavity field. In fact, in the trapping states the quantum states of the radiation field become directly visible. The one-atom maser is the only system we know that allows us to observe the quantum states of the radiation field directly. At low cavity temperatures the number of black-body photons in the cavity mode is reduced and trapping states begin to appear [50, 96]. Under these conditions the sharp spikes appear that were not present in figure 5. These are the signatures of the trapping states that occur at low temperatures because the emission probability  $\mathcal{A}_k$  of equation (4.3) is then a dominant effect. The top plots in figures 8 and 9 show the effect of reduced temperature on the shape of the normalized photon number and the  $Q$  parameter by comparing the curves expected for 100 mK ( $n_{\text{th}} = 10^{-4}$ ) and 500 mK ( $n_{\text{th}} = 0.1$ ). The two bottom plots show blown-up sections of the top plots to make the details clearer. In this case all of the curves are calculated for a cavity temperature of 100 mK, and we compare two pump rates,  $N_{\text{ex}} = 20$  and  $N_{\text{ex}} = 40$ . With a change in the pump rate, the trapping states remain fixed in position but their visibility changes dramatically. In the bottom plot of figure 9 the trapping states are manifested as regions of sub-Poissonian statistics with super-Poissonian regions on either side (this is seen more clearly in the curve for the lower pump rate).

Trapping states occur when  $\mathcal{A}_k = 0$ , i.e. when, for zero thermal photons, emission of an atom is forbidden, so that the Fock space is effectively truncated and the photon number therefore naturally accumulates at this upper limit. Zero emission occurs when the atoms perform an integer number ( $k$ ) of Rabi cycles, i.e. when

$$\sqrt{n_k + 1} \Omega t_{\text{int}} = k\pi \quad (4.5)$$

holds.

In fact, even for certain realistic steady-state operating conditions with a non-zero thermal photon number, the photon distribution can approximate a Fock state very well. Trapping states are characterized by the number of photons  $n_k$  and the number of Rabi cycles  $k$ . The trapping state  $(n_k, k) = (1, 1)$  therefore refers to the one-photon, one-Rabi-oscillation trapped-field state. Equation (4.5) shows that a reliable indication of trapping states is that, unlike other features of the maser pump curve, they are independent of the pump rate, and thus a signature of trapping states is the observation of features in the maser pump curve, as a function of the interaction time, which will not move as a function of the pump rate. A second indication is the characteristic oscillation of the  $Q$  parameter, as shown in figure 9.

The effect of thermal photons (always present at finite temperatures) is to violate the trapping condition, so that the Fock space is no longer truncated. To observe trapping states, one therefore requires very low temperatures and highly stable conditions. Avoiding collective

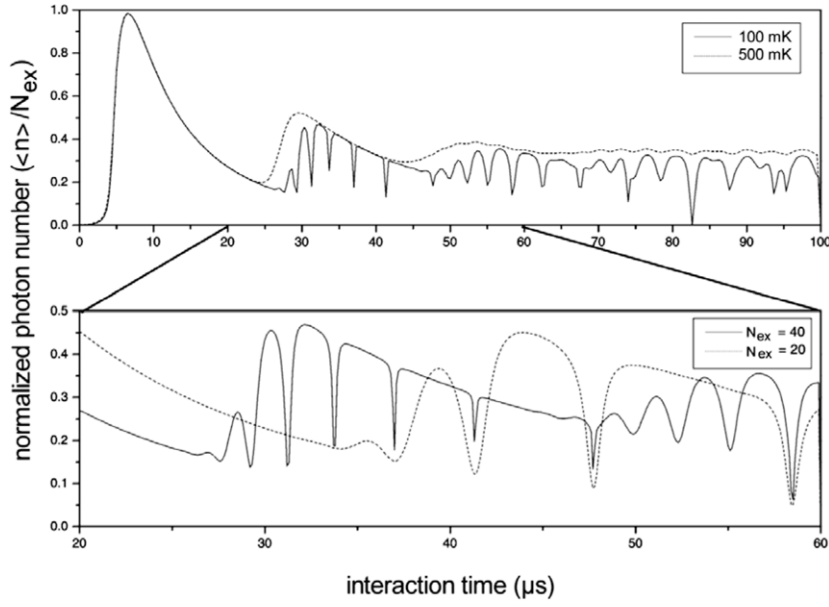


**Figure 8.** One-atom maser at low temperature and high temperature. The top plot shows the effects of reduced temperature on the normalized photon number by comparing the expected curves for 100 mK ( $n_{\text{th}} = 10^{-4}$ ) and 500 mK ( $n_{\text{th}} = 0.1$ ). The bottom plot, which shows a blown-up section of the top plot to make the details clearer, refers to 100 mK and the curves compare two pump rates,  $N_{\text{ex}} = 20$  and  $N_{\text{ex}} = 40$ . The trapping states remain fixed in position but their visibility changes dramatically.

atomic effects and the effect of a finite atomic lifetime is also critically important for the realization of trapping states [59, 73–76, 97]. Trapping states are self-stabilizing against the decay of photons from the mode, since atoms are always available to replace photons lost to decay, thus restoring the trapping condition. With a careful choice of parameters, this self-stabilization can be exploited to produce photon number states in a wide range of operating conditions. This has recently been exploited for producing stable trapping state features [98] and also for creating photon number states on demand [99, 100].

The one-atom maser is the ideal system to realize trapping states. The cavity is operated at a temperature of 0.3 K, leading to a thermal field of about  $3 \times 10^{-2}$  photons per mode.

The first indication of trapping states in the maser field was reported in [50]. These results (corrected for the finite atomic lifetimes) are presented in figure 10 for two values of  $N_{\text{ex}}$  as a function of the interaction time. The cavity temperature was about 340 mK, which corresponds to a thermal photon number of 0.054. This result shows good qualitative agreement with the Monte Carlo simulations by Raithel *et al* [68]. The positions of the dips are preserved at increased pumping strength, as predicted. The reduction in visibility occurs for two reasons: firstly, due to the narrowing of the peaks which occurs for increased pump rates (see figures 8 and 9) and, secondly, due to increased incidence of collective atom effects which act to reduce the visibility of the trapping state.

As the arrival times of the ground-state atoms were also collected in this experiment, it was possible to use equation (4.4) to extract the lower-state statistics of atoms leaving the cavity. The evaluation of this parameter from the experimental data is presented in the bottom plot of figure 10. For most of the positions where there is a trapping state sub-Poissonian statistics are also found. As the atom statistics and photon statistics are related, this is to be expected

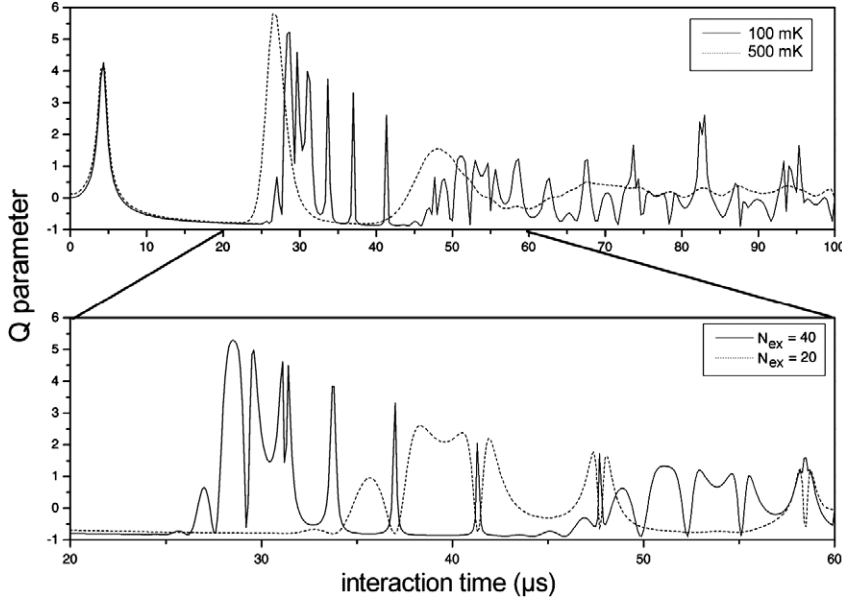


**Figure 9.** One-atom maser at low temperature and high temperature. Same as figure 8, but here the  $Q$  parameter is plotted. Note, in particular, that in the bottom plot the trapping states are manifested as regions of sub-Poissonian statistics with super-Poissonian regions on either side (this is seen more clearly in the lower-pump-rate curve).

if the photon field is truly sub-Poissonian. One finds a good qualitative relationship with the rapidly varying  $Q$  parameter in the plots of figure 9. Note that the vacuum is a coherent state and therefore the lower-state atom statistics should be Poissonian, as they are.

The trapping condition given in equation (4.5) is only accurate when the atoms are resonant with the cavity field. With detuning  $\Delta \neq 0$ , the vacuum emission probability is given by

$$P_g(\Delta, t_{\text{int}}) = \frac{4\Omega^2}{\Delta^2 + \Omega^2} \sin^2\left(\frac{1}{2}\sqrt{\Delta^2 + 4\Omega^2} t_{\text{int}}\right). \quad (4.6)$$

This exhibits oscillatory behaviour that results from Rabi flopping, but, since there is detuning, the observed flopping frequency is higher than that of the vacuum Rabi frequency. When detuning is used in an off-resonant situation, much more periods are thus observed than would occur when the experiment is performed on resonance.

If the flux is increased, the average photon number in the cavity will increase as well since a steady-state field will build up; the oscillations are nevertheless still visible, as can be seen in figure 11, where the left column shows a simulation for  $N_{\text{ex}} = 11$ . The results are shown for different interaction times. When the photon number passes through a minimum, this indicates that the trapping condition is fulfilled for this particular detuning. For the  $t_{\text{int}} = 80 \mu\text{s}$  and  $t_{\text{int}} = 70 \mu\text{s}$  results, all the minima correspond to the vacuum trapping state. The minimum at detuning  $\Delta = 0$  for  $t_{\text{int}} = 60 \mu\text{s}$  corresponds to the (1,1) trapping state whereas the minimum closest to the central maximum for  $t_{\text{int}} = 90 \mu\text{s}$  corresponds to the (2,1) trapping state. The corresponding experimental results are shown in the right column. Here the inversion is used, since it is a natural parameter making use of the full information available from the measurement of the observed number of detected atoms. This has twice the amplitude, but otherwise closely



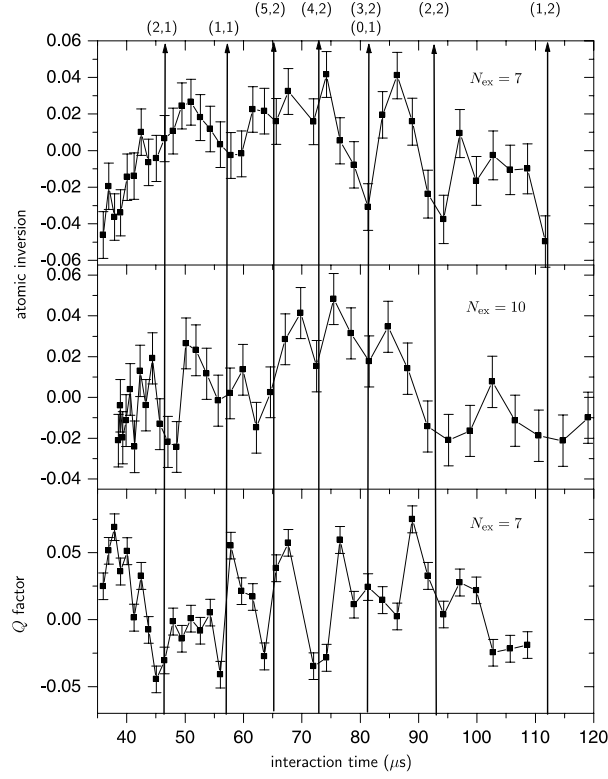


**Figure 10.** Experimental measurement of trapping states in the maser field. The various trapping states are labelled by their  $(n_k, k)$  pair of quantum numbers. Top and centre: trapping states appear as a reduced probability of finding a ground-state atom. Bottom: trapping states appear as regions of sub-Poissonian statistics between regions of super-Poissonian statistics. An exception is the vacuum trapping state, which is the ground state of a coherent field, and therefore the atom counting should have Poissonian statistics. (Reproduced from [50].)

corresponds to a photon number measurement. The agreement between experiment and theory is reasonable.

In previous experiments, trapping states, and thus the influence of Fock states, could be identified up to  $n = 5$  [50]. The set-up currently in use does not permit investigation of the purity of the Fock states obtained under the trapping condition. The dynamic generation of Fock states described in the next section, however, does allow the purity of Fock states to be measured.

#### 4.6. Trapping state stabilization

Trapping states are self-stabilizing in that any photon loss due to cavity decay is replaced by a new photon from the pump atoms and, when the cavity field is in the trapping state, the field distribution is localized to a Fock state, where it will remain for the time determined by the rate of entry of thermal photons into the cavity. As shown above, thermal photons destroy the trapping condition. The best stability is thus achieved by adding a new loss mechanism that can remove any build-up of a field beyond the trapping state. This could be done by adding either lower state atoms to the beam (ground states in the trapping states) or a feedback mechanism that reduces the pump rate to compensate for increased emission [101].



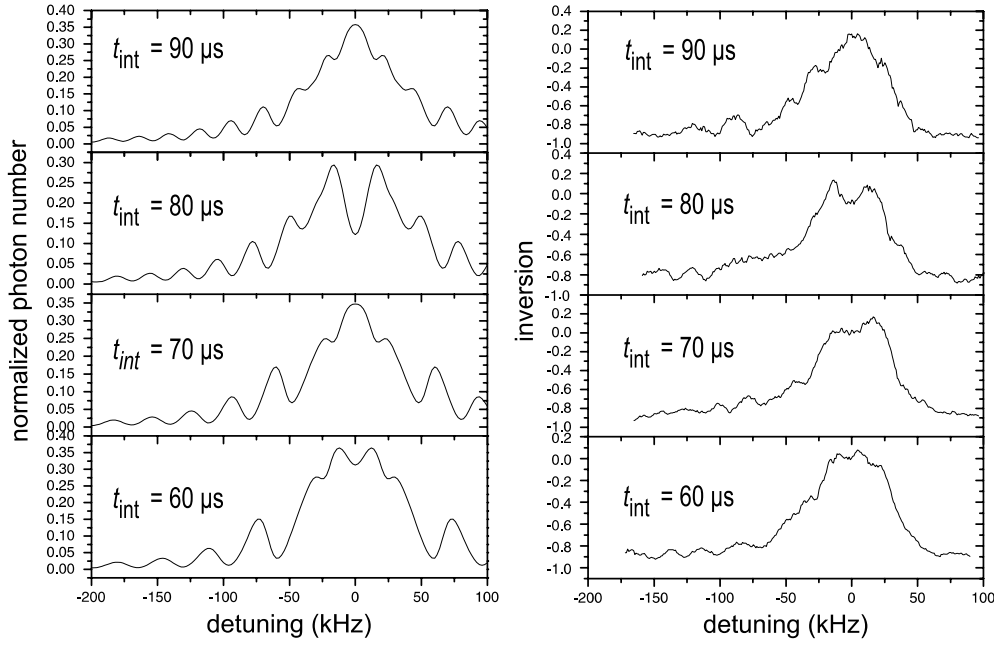


**Figure 11.** Maser resonance and trapping condition. The left column shows the results of a simulation. The oscillations are due to Rabi flopping. The right column shows the corresponding experimental results. The atom flux is  $N_{\text{ex}} = 11$ . The minimum at resonance for  $t_{\text{int}} = 80 \mu\text{s}$  corresponds to the vacuum trapping state. That for  $t_{\text{int}} = 60 \mu\text{s}$  is due to the (1,1) trapping state. The minima at larger detunings are due to Rabi flopping of the vacuum trapping state. For details see text. (Reproduced from [99].)

However, a simpler and ultimately highly effective method is to operate the micromaser in cyclic operation, where the pump atoms are turned on and off for short periods (in comparison with the rate of the build-up of the thermal field) for pump and relaxation cycles. During the pumping cycle the cavity begins to fill with photons, approaching the corresponding CW condition; the pump rate is then turned off for a period to allow the field to relax a little before the next pumping cycle, thus correcting for the entry of thermal photons and allowing the field to resume the trapping condition in the next pulse. After many such cycles the field reaches a steady state that is a combination of the pumping cycle and the relaxation cycle. In this mode of operation, the entry of thermal photons only affects a single pulse, after which the cavity is allowed to relax to a photon number below the steady-state value. In such an operation trapping states are a dominant feature of micromaser dynamics for a wide range of pump rates and thermal photon numbers.

The theoretical model for calculating the cyclically steady state of the maser (the steady state produced for a pulsed pump cycle) was developed to calculate photon distributions for the analytical analysis of Fock states in the experiment presented below and can be found in [92]. Figure 12 shows two sets of theoretical plots of the normalized average photon number ( $\langle n \rangle / N_{\text{ex}}$ ) versus the interaction time ( $T_{\text{int}}$ ) for cyclic and CW operation of the micromaser for a series of thermal photon numbers corresponding to temperatures from 100 mK to 1 K. The cyclic pulse widths were chosen to be  $t = \tau_{\text{cav}}/3$  pump time with  $t = \tau_{\text{cav}}$  between pulses. As this is a 1/3rd pump cycle, the atomic rate during the pump cycle for the cyclic operation was set accordingly in order to maintain the same long-term time average rate as with CW theory. In this way we compare like with like and indeed for low-temperature behaviour both plots are

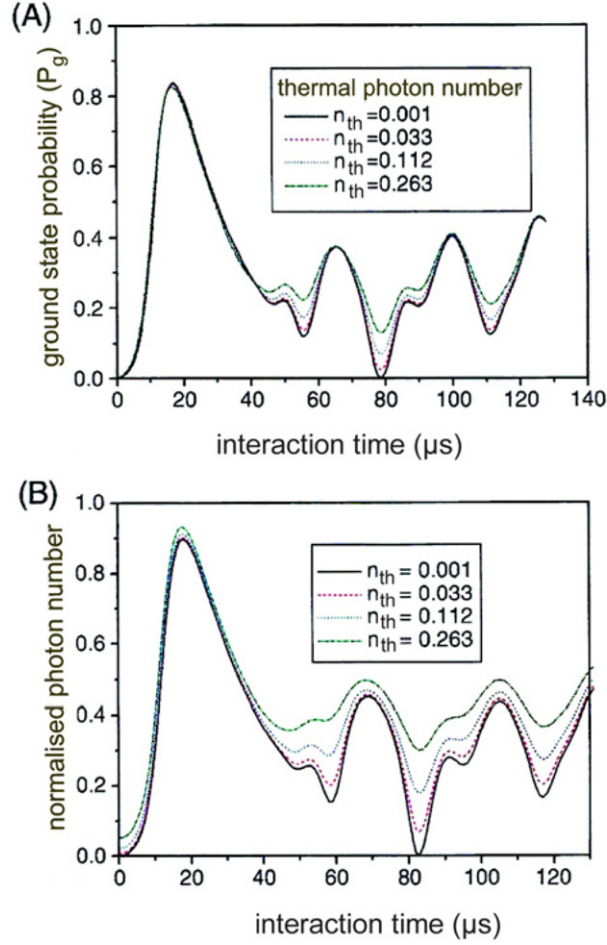


**Figure 12.** Theoretical simulation of the normalized photon number versus interaction time for a micromaser under normal operating conditions. (a) shows the CW photon distributions for the atom rate of  $750 \text{ atoms s}^{-1}$  during a pulse corresponding to a time average pump rate  $250 \text{ atoms s}^{-1}$ . (b) shows the same plot for the unpulsed (CW) normalized photon number for an atomic rate of  $250 \text{ atoms s}^{-1}$ . The improvement in visibility introduced by pulsing the laser is quite clear.

identical; it is only as the temperature of the cavity is increased that the difference becomes quite remarkable. In figure 12(a) the visibility of trapping states (which show up as dips in the curve) remain almost unaltered, whilst they lose visibility rapidly in figure 12(b).

In calculating these plots, additional effects such as interaction time averaging and detuning fluctuations have not been included in the theoretical calculations. The intention here was to show that in the cyclically steady-state trapping states are a more robust feature. This remains true even in the face of increased fluctuations.

The results of this experiment are shown in figure 13. It shows an experimental plot of trapping states that is obtained when the cyclically steady state is used, which when compared with the results of [50] is a substantial improvement in visibility.

The consequences of this are that pulsed operation allows us to find trapping states with greater ease than has ever been previously suspected. This enables us to calibrate an experimental apparatus that is operated under conditions in which trapping states would never

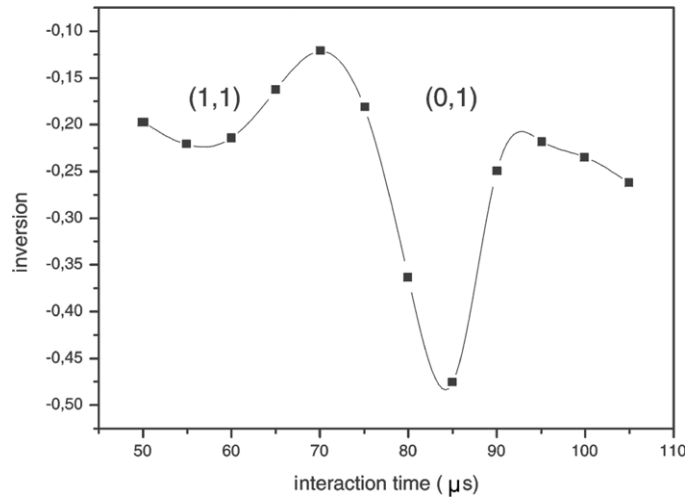


**Figure 13.** Experimental realization of trapping states occurring in the cyclically steady-state micromaser. It is easy to see that in comparison with the results of figure 10 the trapping states have a very high visibility. This is an important result because it shows that trapping states are much more stable than has ever been predicted and could readily be observed even in systems that are less suitable for observing CW trapping states. The figure is taken from [98].

have been suspected to be present and is now routinely used to calibrate the vacuum Rabi frequency at the start of experimental scans. This also shows us how trapping states can be used to stabilize a cavity field and produce Fock states on demand [99, 100] (see below). The ease with which this method enables us to find trapping states has allowed us to make use of these states to perform accurate calibrations of the apparatus, thus significantly improving the operation of the micromaser.

#### 4.7. Fock states on demand

In recent years there has been increasing interest in systems capable of generating photon fields containing a preset number of photons. This has chiefly arisen from applications requiring single photons, such as secure quantum communication and quantum cryptography. Fock states are also useful for generating multiple-atom entanglements in systems such as the micromaser. In the micromaser the generated field and the pumping atoms are in an entangled state. This entanglement can be transferred by the field to subsequent atoms, leading to applications such as basic quantum logic gates.

A basic requirement for *reliably* preparing a field in a preset quantum state is the ability to choose the field state in a controllable manner [51]. Trapping states provide this means. Under trapping-state conditions, quantum feedback between the atoms and the field acts to control the cavity photon number. Trapping states can thus be used to provide photons on demand. Under ideal conditions, the micromaser field in a trapping state is a Fock state, but when the micromaser is operated in a continuous-wave mode, the field state is very fragile and highly sensitive to external influences and experimental parameters. However, in pulsed operation, as opposed to continuous-wave operation, trapping states are more stable and more practical and can be used over a much broader parameter range than in continuous-wave operation [100]. An additional advantage is that the number of photons generated can be investigated by a probe atom after preparation.

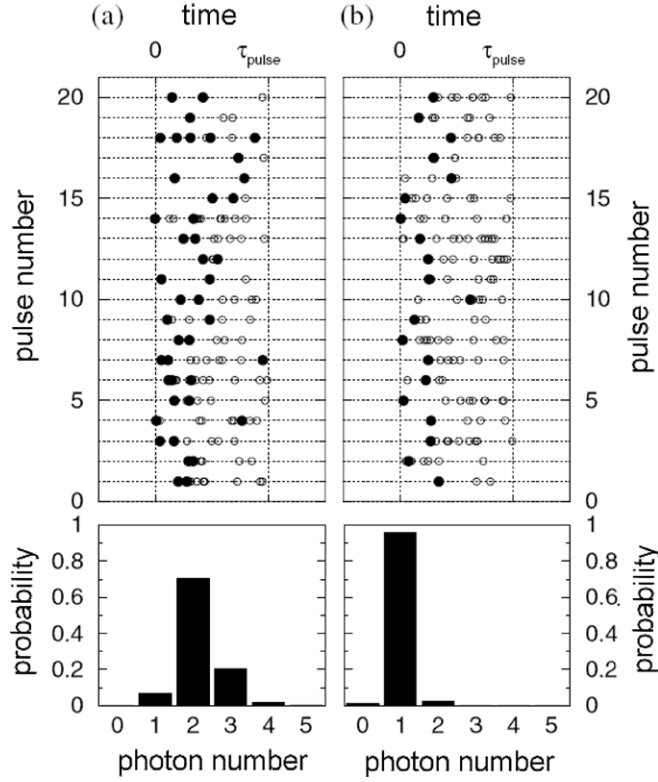


**Figure 14.** A simulation of a subset of 20 successive pulses of the excitation laser and the associated probability distribution for photons or lower-state atom production (solid circles represent lower-state atoms and blank circles represent excited-state atoms). The start and finish of each pulse is indicated by the vertical dotted lines marked 0 and  $\tau_{\text{pulse}}$ , respectively. The two operating conditions are (a) outside the trapping-state conditions ( $gt_{\text{int}} = 1.67$ ), resulting in a broad photon number distribution and (b) the (1,1) trapping state ( $gt_{\text{int}} = 2.2$ ) with a near-Fock-state distribution. Both distributions are sub-Poissonian but they are readily distinguishable experimentally. The size of the atoms in this figure is exaggerated for clarity. The figure is taken from [100].

To demonstrate the principle of Fock state preparation, figure 14 shows a simulation of a sequence of 20 pulses of the pumping atoms in which an average of seven excited atoms per pulse are present. Two operating conditions are present to compare conditions outside trapping conditions ( $gt_{\text{int}} = 1.67$ ) with the (1,1) trapping states ( $gt_{\text{int}} = 2.2$ ). Below the pulse sequences, two distributions show the probability of finding 0–5 atoms (and hence photons) per pulse in the cavity.

Under the trapping condition, only a single emission event occurs, which produces a single lower-state atom, leaving a single photon in the cavity. As during an atom pulse the atom–cavity system is in the trapping condition, the emission probability is reduced to zero after that and the photon number is stabilized. The variation in time when an emission event occurs during the atom pulses in figure 14 is due to the Poissonian spacing of upper-state atoms entering the cavity and the stochasticity of the quantum process. The lower part of figure 14 shows the photon number distribution resulting from this process. In figure 14(a) the broader photon number distribution is due to the absence of a feedback stabilization.

#### 4.8. Dynamical preparation of $n$ -photon states in a cavity

In this section we describe an alternative method of generating number states that also permits the analysis of the purity of the states generated to be unambiguously determined. We start the discussion of the method with some general remarks.

When the atoms leave the cavity in a one-atom maser experiment, they are in an entangled state with the field. If the field is in an initial Fock state  $|n\rangle$  then the interaction of an atom with the cavity leaves the cavity field in a superposition of the states  $|n\rangle$  and  $|n+1\rangle$  and the atom in a superposition of the internal atomic states  $|e\rangle$  and  $|g\rangle$ . The entangled state can be described by

$$|\Psi\rangle = \cos(\phi)|e\rangle|n\rangle - i \sin(\phi)|g\rangle|n+1\rangle, \quad (4.7)$$

where the phase parameter  $\phi$  depends on the interaction time. The state-selective field ionization measurement of the internal atomic state reduces the field to one of the states  $|n\rangle$  or  $|n+1\rangle$ . State reduction is independent of the interaction time, hence a ground-state atom always projects the field onto the  $|n+1\rangle$  state independently of the time spent in the cavity. This results in an *a priori* probability of the maser field being in a specific but unknown number state [102]. If the initial state is the vacuum,  $|0\rangle$ , then a number state is created in the cavity equal to the number of ground state atoms that were collected within a suitably small fraction of the cavity decay time. This is the essence of the method of preparing Fock states by the state reduction proposed by Krause *et al* [102].

In a system such as the micromaser there is no dissipative loss during the interaction and an atom in the cavity undergoes Rabi oscillations. That is, the relative populations of the excited and ground states of the atom oscillate at frequency  $\Omega\sqrt{n+1}$ . As mentioned above, the atomic inversion has been experimentally investigated. In the presence of dissipation, a fixed photon number  $n$  in a particular mode is not observed and the field always evolves into a mixture of such states. The inversion is therefore generally given by

$$I(t_{\text{int}}) = - \sum_n P_n \cos(2\Omega\sqrt{n+1}t_{\text{int}}), \quad (4.8)$$

where  $P_n$  is the probability of finding  $n$  photons in the mode.

The method used in this experiment corresponds to a pump–probe experiment in which pump atoms prepare a quantum state in the cavity which is subsequently measured by a probing atom by studying the Rabi nutation. The signature that the quantum state of interest has been prepared is simply the detection of a definite number of ground-state atoms. To verify that the correct quantum state has been projected onto the cavity, a probe atom is sent into the cavity with a variable, but well-defined, interaction time in order to allow measurement of the Rabi nutation. As the formation of the quantum state is independent of the interaction time, we need not change the relative velocity of the pump and probe atoms, thus reducing the complexity of the experiment. In this sense, we are performing a reconstruction of a quantum state in the cavity using a method similar to that described by Bardoff *et al* [103]. This experiment reveals the maximum amount of information on the cavity photon number that can be found.

The laser beam populating the upper state was pulsed to create short excitation pulses with only a small probability of exciting one atom; thus, when two were observed (i.e. the pump and probe), it is highly probable that not more than two were excited. In fact, to create and detect an  $n$  photon number state in the cavity,  $n+1$  atoms are required. That is,  $n$  atoms to create the number state and the final atom as a probe of the state. With 40% detector efficiency and the assumption that the probability of missing a count is statistically independent, there is an approximately 1% probability of the state preparation being incorrect because an atom escapes detection. Figures 15(a)–(c) displays three Rabi cycles obtained by measuring the inversion of a probe atom that followed the detection of  $n = 0, 1$  and  $2$  ground-state atoms, respectively.

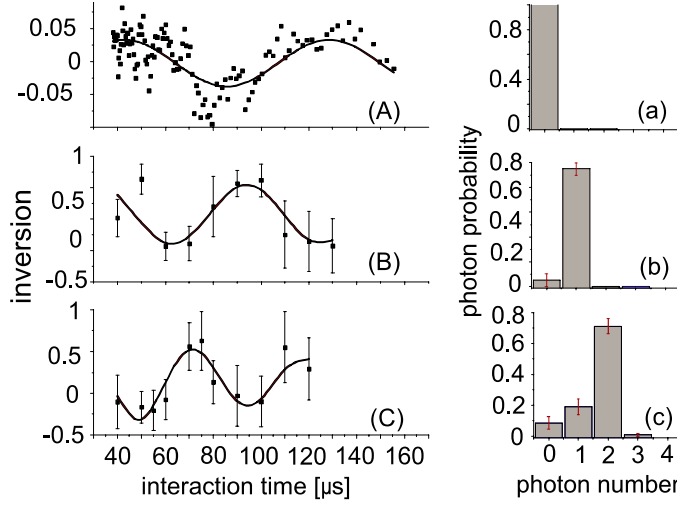


**Figure 15.** Plots (A), (B) and (C) on the left present three Rabi oscillations for the number states  $n = 0, 1$  and  $2$ . Plots (a), (b) and (c) on the right plots display the coefficients  $P_n$ . The photon distribution  $P_n$  was calculated for each Rabi cycle by fitting equation (4.7) to each plot for the set of photon numbers,  $n = 0$  to  $n = 3$ . The relative phase of the Rabi oscillation was fixed since all the atoms enter in the excited state of the maser transition. In each fit, the highest probability was obtained for the target number state. Unlike the  $n = 1$  and  $n = 2$  Rabi cycles, the  $n = 0$  oscillation of plot (A) was obtained in the steady-state operation of the micromaser in a very low-flux regime. The fit to this curve was performed for Rabi cycles from  $n = 0$  to  $n = 2$ . The low visibility of this curve was due to the low flux (one atom per second) which was required to reduce the steady-state operation of the micromaser to below-threshold behaviour; hence detector dark counts become comparable to the real count rates and therefore contribute to a large background. During the Rabi cycle the cavity photon number changes periodically. At the maxima there is one photon more than at the minima. (Reproduced from [51].)

Because of the long waiting times for three atom events, the  $n = 2$  Rabi data were more difficult to collect than the other two measurements. The data collection time became substantially longer as the interaction time was increased, and then background effects have a higher impact on the data. The fit to the  $n = 2$  data includes an exponentially decreasing weight, so that measurements obtained for longer interaction times have less significance than those at short times.

The fact that pure number states were not obtained here is due to dissipation in the time interval between production and analysis of the cavity field. The simulations described in the following demonstrate that one could generate number states with a purity of 99% for the  $n = 1$  state and 95% for the  $n = 2$  state at the time of generation, which is then modified by dissipation between production and measurement.

For the simulations two idealizing assumptions were made: thermal photons are only taken into account for the long-term build-up of the cyclically steady state and Gaussian averaging over the velocity spread of the atoms is considered to be about 3%. Included in the calculations are the exponential decays for the cavity field during the pulse when either one photon (for  $n = 1$ ) or two photons were deposited one by one (for  $n = 2$ ), changing the photon number distribution. The simulations also average over the Poissonian arrival times of the atoms. Details of the calculation are discussed in [92]. They are compared with the experimental results in figures 16(a) and (b).

As dissipation is the most essential loss mechanism, it is interesting to compare the purity of the number states generated by the current method with that expected for trapping states

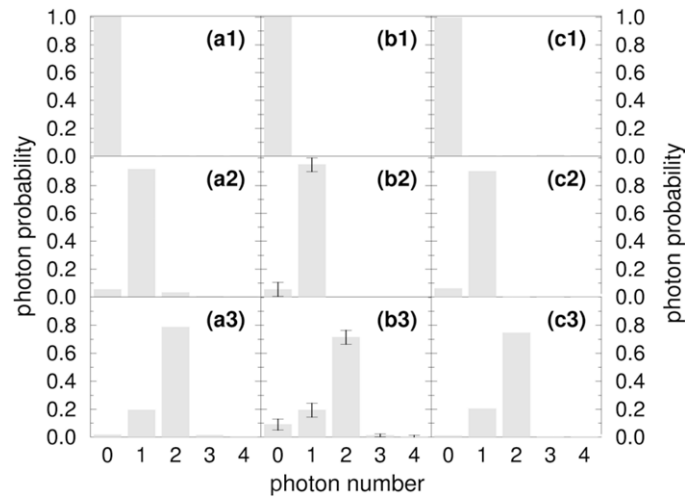


**Figure 16.** Comparison between theory and experimental results on the purity of number states. The columns represent photon distributions obtained from: (a) a theoretical simulation of the current experiment; (b) the current experimental results; and (c) a theoretical model that extends the current experiment to the steady state at the positions of the trapping states. The agreement between the two theoretical results and the experimental result is remarkable, indicating that dissipation is the most likely loss mechanism. Without dissipation, i.e. at the moment of generation the purity of the states is 99% for  $n = 1$  and 95% for  $n = 2$ . (Reproduced from [51].)

(cf figure 16(c)). The agreement of the purity of the number states is striking. The trapping state photon distribution is generated in steady state, which means that whenever the loss of a photon occurs the next incoming atom will restore the old field with a high probability. The non-zero amplitudes of the states  $|0\rangle$  in figure 16(c2) and  $|1\rangle$  in figure 16(c3) are due to dissipative losses before restoration of a lost photon which is not replaced immediately but after a time interval dependent on the atom flux. The atom rate used in these calculations was 25 atoms per cavity decay time, or an average delay of 1 ms. This can be compared with the delay between the preparation and probe atoms in the present experiment. In the steady-state simulation loss due to cavity decay determines the purity of the number state; in the limit of zero loss the state measurement is perfect. It can therefore be concluded that dissipative loss due to cavity decay in the delay to a probe atom largely determines the measured deviation from a pure number state. There is, of course, the question of the influence of the thermal field on the photon distribution. By virtue of the selection process in the current experiment we reduce the influence of the thermal field by only performing measurements of the field state following a trigger of ground-state atoms. Hence the state of the field is well known. The simulations for the steady-state case were therefore performed for a temperature of 100 mK, which makes the influence of the thermal field on the steady state correspondingly low. While this is not the first observation of Fock states in general (the  $n = 1$  Fock state having been observed earlier [66]), it is the most detailed study of the interaction of an atom with a quantized mode that has been carried out to date. Here we see the creation of a field state by state reduction and the observation of the interaction of this state with a probe atom.

The unambiguous generation of Fock states of the radiation field described in the previous chapter allows an interesting observation concerning the decay of the photons. Quantum fields decay discretely. This can be neatly observed by looking at the variation of the Rabi frequency in time observed after the Fock state generation. The results are shown in figure 17. The



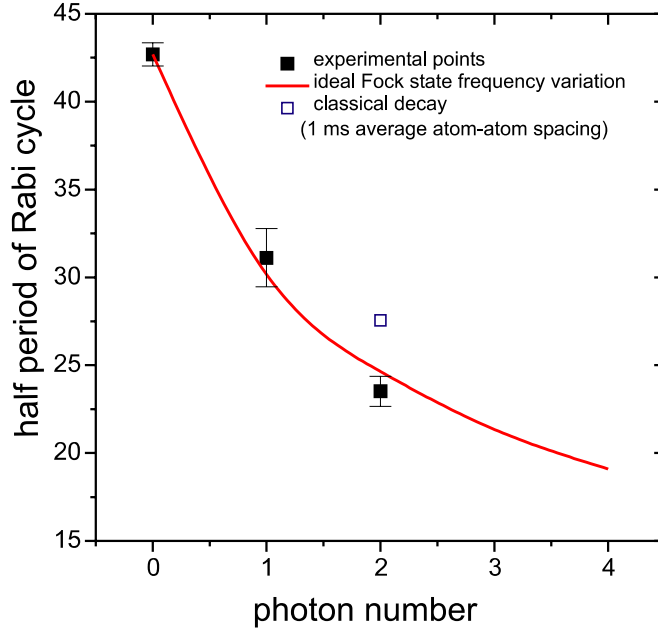


**Figure 17.** Dependence of the Rabi frequency on the photon number. A single sine fit to each of the three Fock states is plotted versus the theoretical variation of frequency as a function of photon number. The coupling constant  $36.8 \text{ krad s}^{-1}$  is the optimum fit to the data. The figure is taken from [98].

discrete decay follows the solid curve in the figure, whereas a classical and continuous decay would result in a larger period of the Rabi frequency given by the square at photon number state  $n = 2$  [98].

#### 4.9. The one-atom maser spectrum

The properties of the micromaser we have discussed so far were all connected with the population of the maser levels or with the diagonal elements of the radiation-density matrix. In the following we would like to discuss a feature—the micromaser spectrum—which depends on the nondiagonal elements [104].

The micromaser spectrum is determined by the decay of the expectation value of the electric field [105] of the maser field

$$\langle E(t) \rangle \sim \sum_{n=0}^{\infty} (n+1)^{1/2} \rho_{n,n+1}(t). \quad (4.9)$$

In order to calculate the spectrum and the linewidth  $D$  of the micromaser an analytical approach was used [104] whereby two novel features, quite distinct from the familiar Schawlow–Townes linewidth [105], show up. As can be seen in figure 18 (i) the trapping states impress sharp resonances onto  $D$  as a function of the pump parameter  $\Theta$ , (ii) for large values of  $\Theta$  the linewidth  $D$  decreases and can even oscillate, a phenomenon alien to the monotonic dependence of the Schawlow–Townes linewidth.

Figure 18 is based on the equation for the linewidth [104]:

$$D = 4r \sin^2 \left[ \frac{g\tau}{4\sqrt{\langle n \rangle}} \right] + \frac{\gamma(2n_{th} + 1)}{4\langle n \rangle}. \quad (4.10)$$



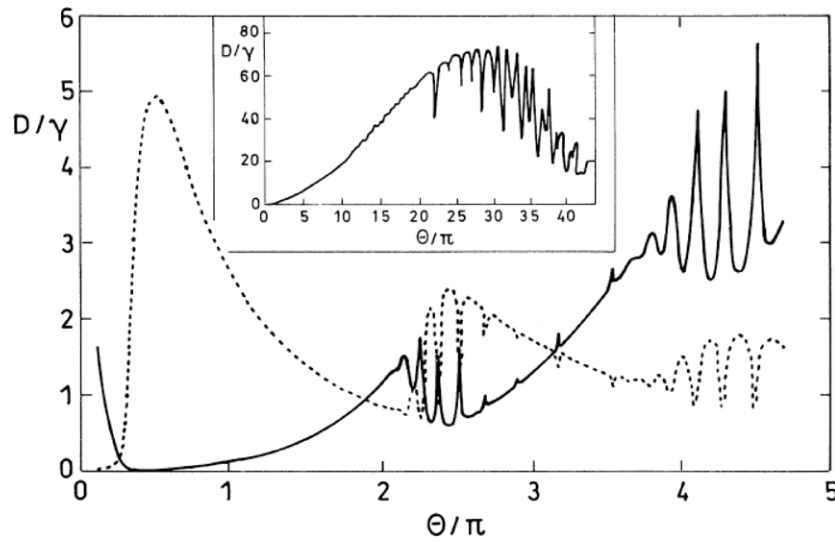


**Figure 18.** The relative linewidth  $D/\gamma$  based on equation (4.10) (solid curve and mean photon number  $\langle n \rangle/10$  (.....)) as a function of the pump parameter  $\Theta = N^{1/2}g\tau$  for  $N = 50$  and mean thermal photon number  $n_b = 10^{-4}$ . The inset shows the exact relative linewidth  $D/\gamma$  based on a numerical solution of the density matrix for large pump parameter  $\Theta$  for  $N = 20$  and  $n_{th} = 1$ .

This equation is derived from the exact spectrum using a detailed balance condition and the fact that the equation of motion for the density matrix elements  $\rho_{n,n}$  only couples to the nearest neighbours  $\rho_{n,n+1}$  and  $\rho_{n,n-1}$ . For the exact numerical treatment of the relevant density-matrix equations see [106, 107]

In figure 18 the detailed behaviour of the phase diffusion constant  $D$  is depicted (solid line) as a function of the pump parameter  $\Theta = \sqrt{N}g\tau$  for  $N = 50$  and  $n_{th} = 10^{-4}$  thermal photons. The sharp resonances in the monotonic increase of  $D$  are reminiscent of the trapping states. To bring out this similarity in the same figure, the average photon number as a function of  $\Theta$  (dotted curve) is shown. We note that the phase diffusion is especially large when the maser is locked to a trapping state, that is, when  $\langle n \rangle$  is caught in one of those sharp minima. Equation (4.10) for  $D$  reveals this behaviour in the limit of short interaction times or large photon numbers, that is, when  $g\tau/4\langle n \rangle^{1/2} \ll 1$ . If the sine function is expanded, the familiar Schawlow–Townes linewidth [105] is obtained

$$D = \frac{\alpha + \gamma(2n_{th} + 1)}{4\langle n \rangle}, \quad (4.11)$$

where  $\alpha = \gamma(N^{1/2}g\tau)^2 = \gamma\Theta^2$ .

The complicated pattern of the micromaser linewidth results from the complicated dependence of  $\langle n \rangle$  on the pump parameter indicated in figure 18 by the dotted curve which enters the denominator. We emphasize that the maser linewidth for the micromaser goes beyond the standard Schawlow–Townes linewidth. The sine function in the formula for  $D$  suggests in the limit of large  $\Theta$  values an oscillatory behaviour of the linewidth. The exact numerical result shown in the inset of figure 18 confirms that.

The experimental investigation of the micromaser spectrum is of great fundamental interest. As the nondiagonal field elements are involved, their measurement is not so easy

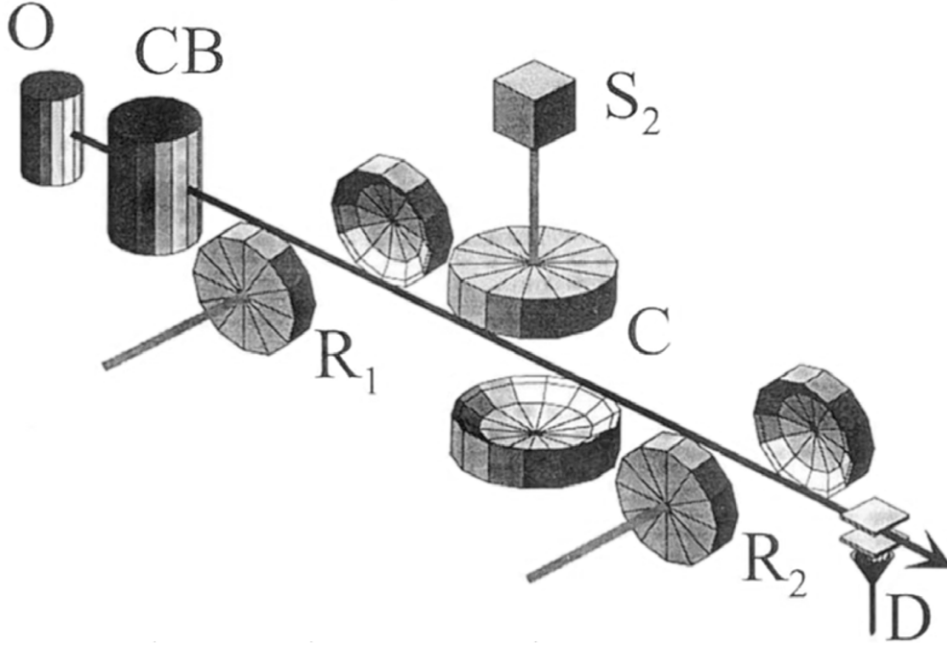


**Figure 19.** Cavity-QED set-up used by the group of Haroche and co-workers at the ENS. This figure is taken with small modifications from [34].

to perform with the present set-up as the holes in the cavity for the atomic beam may perturb the nondiagonal contributions. Therefore several methods have been proposed allowing us to measure the phase diffusion despite these perturbing effects [108–110]. All those methods are based on a heterodyne scheme. The maser field is displaced by an injected field and then measured by a probe atom. In this way a reconstruction of the field is possible just by the determination of the atomic inversion.

## 5. Other microwave cavity experiments

In the following, we briefly review the cavity QED work performed by the group of S Haroche and co-workers at Ecole Normale Supérieure (ENS) in Paris.

The cavity of the ENS group has an open geometry made of two spherical superconducting mirrors in a Fabry–Perot configuration marked by C in figure 19. The transitions investigated by this group are at 51.1 GHz, corresponding to a transition between circular Rydberg states with principal quantum numbers 51 and 50. The circular states are characterized by maximum orbital and magnetic quantum numbers. The valence electron is a thin torus centred on the atom's core. They are produced in the CB unit using velocity-selective laser excitation. The velocity-selected atoms cross the cavity perpendicularly to the axis; the interaction length is about 6 mm in diameter. The decay time of the cavity is typically 1 ms (corresponding to  $Q = 3 \times 10^8$ ). The entire set-up is cooled to about 1 K to minimize thermal noise [56, 57, 111]. At the thermal equilibrium the cavity mode contains about 0.7 thermal photons on average, originating from the thermal field leaks. In order to remove this field at the beginning of each sequence atoms prepared in the lower state are transmitted through the cavity to absorb the thermal photons. At the end of this cooling sequence the mean photon number

is reduced to 0.1 per mode. Detection of the Rydberg atoms is performed as in the Munich set-up by field ionization which can be done state-selectively (D, figure 19). Experiments are also performed where superpositions of the states are investigated. The set-up has, for this purpose, two additional classical fields  $R_1$  and  $R_2$  coupled to the atoms via two spherical cavities to allow the Ramsey-type two-field interaction ([36]). The signal fringes can be investigated to study changes in the phase and amplitude of the interaction between the atom and cavity [34].

With this set-up a variety of experiments on the atom–cavity interaction were performed. A survey is given in the following. For a detailed review see [112].

### 5.1. Collapse and revival of the Rabi oscillations in an injected coherent field

As discussed above, the quantum dynamics depends on the photon statistics of the interacting field. We have already described the measurement of the dynamics in a thermal field in the micromaser cavity [52] and in a number state field up to  $n = 2$  [51]. Further experiments have been performed with the spherical cavity and an injected coherent field with an average photon number of  $n = 2$  [86]. The expected collapse and revivals [84] were observed.

Revivals of the Rabi oscillations can also be induced by a time reversal pulse [116]. The technique was first proposed by Morigi *et al* [121] and is suitable for distinguishing contributions from coherent and incoherent processes in the evolution of the system. For this purpose the system is exposed to a short electromagnetic pulse after a free evolution during the time  $T$  leading to a reversal of the system's unitary evolution. At time  $2T$  the system then resumes the initial state if no decoherence is present. This scheme was applied to investigate the atomic Rabi oscillations in a mesoscopic coherent field [116] with an average of 13 photons. The oscillation undergoes a collapse due to the dispersion of the Rabi frequencies. This effect is unitary and reversible. After a time proportional to the field amplitude, the oscillation is expected to revive. When a  $\pi$  phase shift is applied to the atomic coherence after the collapse time, an early induced Rabi revival is observed. The amplitude of this echo signal is sensitive to non-unitary decoherence processes.

### 5.2. Atom–photon and atom–atom entanglement

It has already been mentioned that quantum Rabi oscillations provide a simple and flexible tool to entangle atoms and photons (see section 4.2). If the Rabi oscillation in vacuum is interrupted mid-way ( $\pi/2$  pulse) between the upper and lower atomic states, the final state of the atom–cavity field system is a maximally entangled state. In the event of the Rabi oscillation lasting twice as long ( $\pi$ -pulse) the cavity and atom exchange their energy with maximum probability. An atom initially in the lower state of the transition when it enters the cavity containing one photon will end up with high probability in the upper state, leaving the cavity empty. This process can be used to transform an atom–field entanglement into an atom–atom one. When in the experiments two atoms cross the cavity one after the other, the first is initially in the upper level and the second in the lower one. The first atom undergoes a  $\pi/2$  Rabi pulse and gets entangled with the cavity. The second is subjected to a  $\pi$  pulse, copying the cavity state and getting entangled in the process with the first atom. This entanglement was checked in various measurements on the final states of the two atoms and in studying their correlations [54,55]. See also [112] in connection with the generation of EPR pairs. For related work on entanglement with the micromaser see [95]. The generation of a GHZ state and EPR tests in the micromaser is described in [113,114].

### 5.3. Atom–photon phase gate

An atom–photon phase gate can be realized since after a full cycle of quantum Rabi oscillation ( $2\pi$  Rabi pulse) the system reaches the initial state, but the phase of the wave function of the atom has undergone a  $\pi$ -shift. See also [115]. An atom initially in the lower state of the transition with one photon in the cavity therefore emerges in the same state, the photon being left in the cavity with high probability but with the sign of the wavefunction of the atom being changed. If the cavity is initially empty, the sign of the atomic state is unaltered. When photon and atom are considered quantum-bits carrying binary information, the  $2\pi$  Rabi pulse couples them according to the conditional dynamics of a quantum phase gate [111].

### 5.4. Quantum nondestructive-measurement of a photon

The principle of a quantum phase gate described above can also be used for nondestructive measurement of single photons in a cavity [56]. The phase change of the wavefunction of the atom occurring when exposed to a  $2\pi$  Rabi pulse can be transferred into an inversion of the phase of the fringe pattern of a Ramsey interferometer sandwiching the microwave cavity (figure 19). When the interferometer is adjusted to a fringe maximum, the photon number 0 or 1 is correlated to the final state of the atom. The method, however, does not allow one to measure deviations from a single photon state (see section 4.6). See also [115].

Recently, it was also demonstrated that an experiment analogous to the photon detection described is also possible for nondestructive Rydberg atom counting using a mesoscopic field in a cavity [117]. The state-dependent atomic index of refraction being proportional to the atomic number shifts the classical field phase, which is changed into intensity information by a phase-sensitive homodyne procedure. This method may open the possibility of using Rydberg atoms for more applications in quantum information processing.

### 5.5. Wigner function of a one-photon state

Rydberg atoms are sensitive probes of a microwave cavity field that make it possible to determine its quantum state through determination of quasi-probability distributions which contain information on the field density distribution. Furthermore, they exhibit the quantum properties of the field if present. The Husimi  $Q$  and Wigner functions have been measured for atom cavity systems [118]. For direct determination of the Wigner function of a one-photon Fock state, by a method proposed in [115] (see also Bertet *et al* [119]). Lougovski *et al* [120] showed that the Fresnel transform of measured Rabi oscillations provides an especially simple means of determining the Wigner function, being a much faster method than depending on the dispersive interaction between atoms and field. For the reconstruction of the Wigner function in the one-atom maser see [108, 109].

### 5.6. Multiparticle entanglement

When quantum Rabi pulses of variable duration and auxiliary Ramsey pulses are applied to successive atoms crossing a set-up of the kind displayed in figure 19, one can generate and analyse entangled states involving more than two particles. Such a procedure was demonstrated for the entanglement of up to three atoms [57]. The disadvantage of the experiment is that the atomic coherences cannot exit cavity C, which was modified in relation to figure 19 by an additional ring structure to increase the photon lifetime. A further limitation is that circular atoms are prepared with Poissonian statistics with a low mean value, requiring long data acquisition times. For a review on the multiparticle entanglement in the micromaser see [95].

### 5.7. Schrödinger cats and decoherence

For this experiment a small coherent field containing an average of 3 to 10 photons is prepared in cavity C (figure 19) by coupling it to an external coherent source. This field interacts with a single atom in a state superposition (produced by a  $\pi/2$  pulse in cavity R). The atomic transition and the cavity frequency are slightly off resonance so that the atom and the field cannot exchange energy but undergo dispersive frequency shifts. The atom–field coupling during the interaction time produces atomic-level-dependent dephasing of the field and generates an entangled state with phase  $\phi = g^2 t / \delta$  ( $t$ : interaction time,  $\delta$ : detuning). After leaving field C the atom undergoes another  $\pi/2$  pulse in cavity  $R_2$  identical to R (figure 19). The signal in the field ionization detector shows Ramsey fringes [36] since the transition monitored can occur either in field  $R_1$  or  $R_2$  and these two ‘paths’ are indistinguishable. The fringe contrast depends on  $\phi$  and decreases with increasing  $\phi$  due to decoherence since the ‘distance’ between the interfering states varies as  $D = 2\sqrt{n} \sin \phi$ . The result obtained for the decoherence time is shorter than the photon decay time in the cavity [122]. The result agrees with simple decoherence theories. The open cavity C leads to a rather strong coupling to the environment, and so investigations with a better closed cavity would be desirable and this is being pursued by the ENS group.

## 6. Slow atoms

### 6.1. Jaynes–Cummings dynamics for slow atoms

In standard micromaser experiments, the kinetic energy of the atoms is of the order of  $10^{-1}$  eV, and the atom–photon interaction energy is  $\hbar g \sqrt{n+1}$  if  $n$  excitations are involved, where  $\hbar g \simeq 3 \times 10^{-11}$  eV. Under these circumstances, the atom’s centre-of-mass motion is essentially classical, so that the position dependence of the atom–photon coupling translates into a time dependence in accordance with the atom’s (mean) velocity—recall the time-dependent  $g(t)$  of equations (4.1) and (4.2). Indeed, it can be shown that predictions are not changed when first-order (WKB) corrections are included [123].

Matters are much different for ultraslow atoms whose kinetic energy is comparable to the atom–photon interaction [124, 125]. Then the relevant terms in the Hamilton operator are

$$H = \frac{p^2}{2M} + \hbar \omega a^\dagger a + \hbar(\omega + \Delta) \sigma^\dagger \sigma - \hbar g(z)(a^\dagger \sigma + \sigma^\dagger a), \quad (6.1)$$

where the Jaynes–Cummings coupling  $\propto \hbar g(z)$  is supplemented by the kinetic energy  $p^2/(2M)$ . The local Rabi frequency  $g(z)$  is proportional to the mode function of the privileged cavity mode; it vanishes outside the resonator (i.e.  $z < 0$  and  $z > L$ ), and we assume  $g(z) > 0$  inside (i.e.  $0 < z < L$ ). On resonance ( $\Delta = 0$ ), the equivalent form

$$H = \frac{p^2}{2M} + \hbar \omega (a^\dagger \sigma + \sigma^\dagger a)^2 - \hbar g(z)(a^\dagger \sigma + \sigma^\dagger a) \quad (6.2)$$

shows that the dressed states with  $a^\dagger \sigma + \sigma^\dagger a > 0$  experience the atom–photon interaction as an attractive potential, whereas those with  $a^\dagger \sigma + \sigma^\dagger a < 0$  see a repulsive potential. For ultraslow atoms, this repulsive potential may, in fact, be a potential barrier that prevents the atoms from entering the resonator.

To be specific, we recall that  $|\pm, n\rangle$ , for instance, stands for ‘atom excited and  $n$  photons in the cavity’)

$$|\gamma_0\rangle = |\mp, 0\rangle, \quad |\gamma_n^{(\pm)}\rangle = \frac{1}{\sqrt{2}}(|\pm, n-1\rangle \pm |\mp, n\rangle) \quad (6.3)$$

are the dressed states in question, since

$$(a^\dagger \sigma + \sigma^\dagger a)|\gamma_0\rangle = 0, \quad (a^\dagger \sigma + \sigma^\dagger a)|\gamma_n^{(\pm)}\rangle = \pm\sqrt{n}|\gamma_n^{(\pm)}\rangle, \quad (6.4)$$

for  $n = 1, 2, 3, \dots$

As an example, consider an excited atom incident upon an empty resonator. Using  $z$  wave functions for the centre-of-mass motion and ket vectors to describe the internal atomic and photon states, the initial state

$$|\pm, 0\rangle\psi(x) = \frac{1}{\sqrt{2}}(|\gamma_1^{(+)}\rangle + |\gamma_1^{(-)}\rangle)\psi(x) \quad (6.5)$$

is a superposition of the dressed states  $|\gamma_1^{(+)}\rangle$  and  $|\gamma_1^{(-)}\rangle$ . The branch  $|\gamma_1^{(+)}\rangle\psi(x)$  propagates through the attractive potential well and is predominantly transmitted, whereas the evolution of  $|\gamma_1^{(-)}\rangle\psi(x)$  is governed by the repulsive potential barrier and may be reflected with a large probability. These matters are illustrated in figure 20, where one clearly sees how the attracted branch is first accelerated and then decelerated as it traverses the resonator, and how the repulsed branch is reflected.

The cavity parameter values in figure 20 are roughly those of the Garching micromaser experiments. Yet, an interaction time of several seconds is not small on the scale set by the photon lifetime (a few hundred milliseconds have been achieved [92]). A more realistic calculation must therefore take photon dissipation into account during the atom-photon interaction. For the initial state (6.5), there is at most one photon in the resonator. As soon as it disappears, the interaction is turned off and the atom continues to move with the velocity it just happens to have. Somewhat surprisingly, photon dissipation may therefore lead to a net increase in the atom's kinetic energy. This is the case if the photon disappears after the attracted branch has been accelerated but before it gets decelerated again for which instant (b) in figure 20 is the extreme example.

The outcome of a calculation with dissipation is presented in figure 21. The reflection probability is markedly reduced, from 50% in figure 20 to just 4.8% now. This is easily understood upon realizing that it takes more than four photon lifetimes to get from instant (a) to instant (b) in figure 20, so that the repulsed branch has a good chance to enter the force-free motion period, after the photon is dissipated and before the velocity turns negative. Then, although slowed down, the atom will get across the resonator rather than being reflected. We also note that as a result of the random nature of the photon dissipation, the velocity distribution is considerably smeared out.

If there is a sizeable detuning,  $\Delta$ , between the photon frequency and the natural frequency of the atomic transition, we can replace equation (6.2) by

$$H = \frac{p^2}{2M} + \hbar\omega(a^\dagger \sigma + \sigma^\dagger a - \sigma_3 \tan \phi)^2 - \hbar g(z)(a^\dagger \sigma + \sigma^\dagger a - \sigma_3 \tan \phi) - \hbar\omega(\tan \phi)^2 + \frac{1}{2}\hbar\Delta, \quad (6.6)$$

where the  $z$ -dependent angle parameter  $\phi$  is given by

$$\tan \phi(z) = \frac{\Delta}{2g(z)}, \quad (6.7)$$

so that we have

$$\phi = \begin{cases} \pi/2 & \Delta > 0, \\ -\pi/2 & \Delta < 0, \end{cases} \quad (6.8)$$

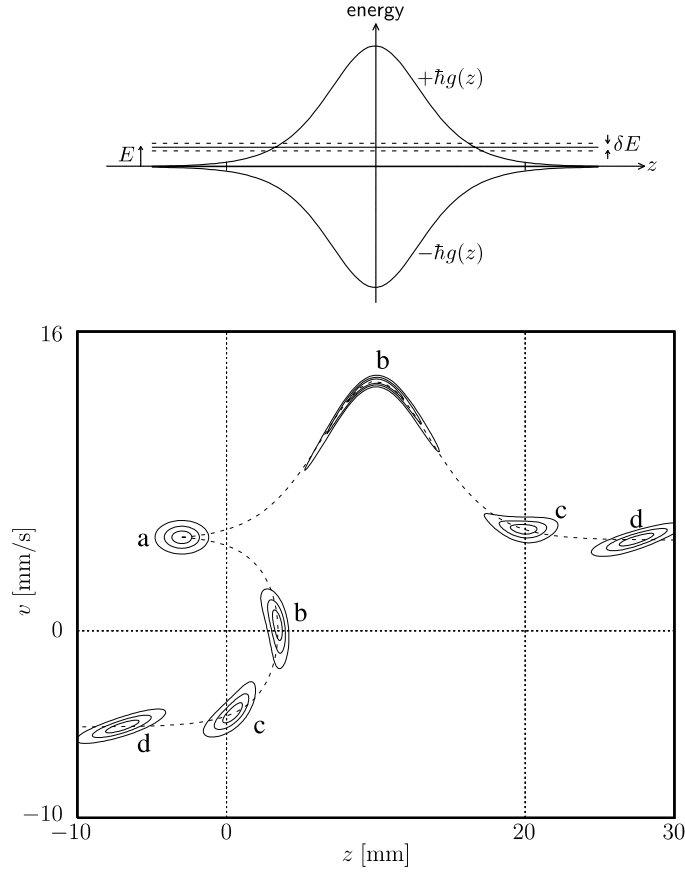


**Figure 20.** Ultraslow excited atom (mass  $M = 1.4 \times 10^{-22}$  g) incident upon an empty resonator (on resonance, no photon damping). The atom is inside the resonator for  $0 < z < L = 20$  mm. The top plot shows the attractive and repulsive potentials for the dressed states  $|\gamma_1^{(\pm)}\rangle$  derived from  $g(z) = \frac{1}{2}\epsilon\bar{g}[\cosh(\epsilon(z/L - \frac{1}{2}))]^{-2}$  with  $\bar{g} = 44 \text{ krad s}^{-1}$  and  $\cosh(\epsilon/2) = \sqrt{27}$ . The extrema correspond to an energy of  $\pm 6.75 \times 10^{-11}$  eV. The bottom plot shows the Wigner function [126] of the evolving atomic centre-of-mass distribution. The contour lines enclose 20%, 50% and 80% of the total probability. Dashed curves mark the classical phase space trajectories. The initial distribution (a) has a mean position  $\langle z \rangle = -3$  mm with a spread of 1 mm and a mean velocity  $\langle v \rangle = \langle p \rangle / M = 5 \text{ mm s}^{-1}$  with a spread of  $0.5 \text{ mm s}^{-1}$ , so that the energy is  $E = 1.09 \times 10^{-11}$  eV with a relative spread of  $\delta E / E = 0.2$ . The various instants are (a) before the interaction ( $t = 0$ ), (b) during the interaction ( $t = 1.8$  s), (c) at the end of the interaction ( $t = 3$  s) and (d) after the interaction ( $t = 4.5$  s). (Adapted from [127]).

outside the resonator, where  $g = 0$ . The relevant dressed states are now the eigenstates of  $a^\dagger \sigma + \sigma^\dagger a - \sigma_3 \tan \phi$ . These are  $|\gamma_0\rangle$  of equation (6.3) to eigenvalue  $\tan \phi$  and, for  $n = 1, 2, 3, \dots$ ,

$$|\gamma_n^{(\pm)}\rangle = |\pm, n-1\rangle \cos(\pi/4 \pm \theta_n/2) \pm |\mp, n\rangle \sin(\pi/4 \pm \theta_n/2) \quad (6.9)$$

to eigenvalues  $\pm \sqrt{n + (\tan \phi)^2}$ , respectively, with  $\theta_n(z)$  determined by

$$\sin \theta_n = \frac{\tan \phi}{\sqrt{n + (\tan \phi)^2}}, \quad \cos \theta_n = \sqrt{\frac{n}{n + (\tan \phi)^2}}. \quad (6.10)$$

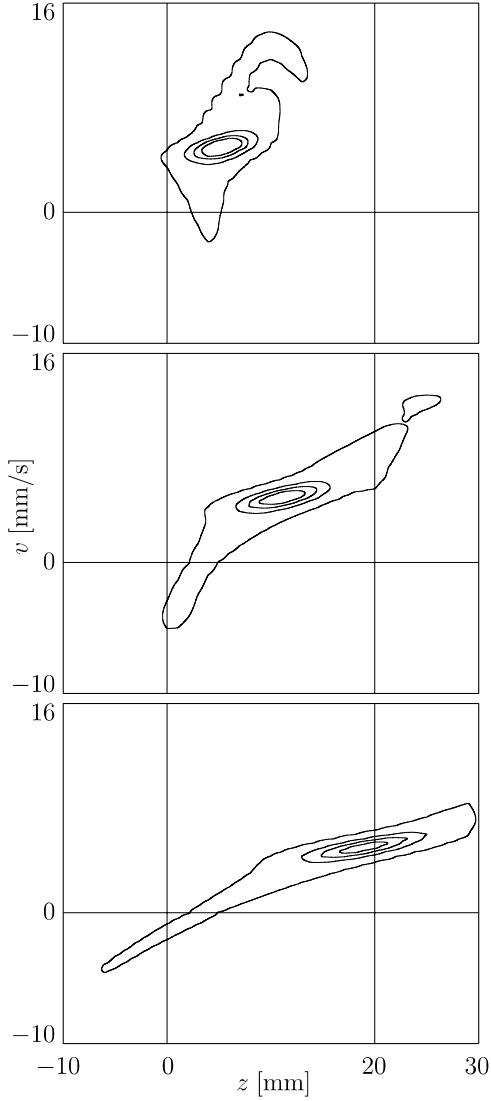


**Figure 21.** Ultraslow atom incident upon an empty resonator (on resonance, with photon dissipation). The parameters are the same as in figure 20, except that a finite photon lifetime of 400 ms is taken into account. For the initial distribution of figure 20 we show the evolved distributions at instants (a)  $t = 1.8$  s, (b)  $t = 3$  s and (c)  $t = 4.5$  s. The contour lines correspond to 20%, 13%, 6% and 0.4% of the maximal value at  $t = 0$ . The ranges for  $z$  and  $v = p/M$  are the same as in figure 20. (Adapted from [127].)

In particular, for  $\Delta > 0$ , this states that

$$|\gamma_n^{(\pm)}\rangle \rightarrow \begin{cases} |\mp, n\rangle, \\ |\mp, n-1\rangle, \end{cases} \quad \text{as } g \rightarrow 0. \quad (6.11)$$

So the initial state of equation (6.2) begins here as  $|\gamma_1^{(-)}\rangle$ , and if the detuning is large enough to ensure an adiabatic passage, the system will remain in this dressed state all the time and



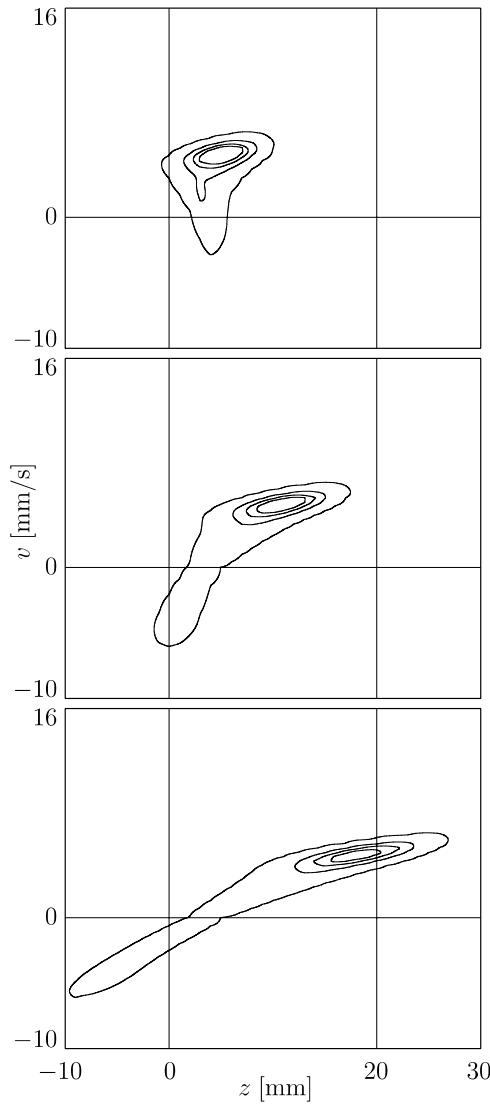


**Figure 22.** Ultraslow atom incident upon an empty resonator (off resonance, with photon dissipation). The parameters are the same as in figure 21, except that a detuning of  $\Delta = 100 \text{ rad s}^{-1}$  is taken into account. For the initial distribution of figure 20 we show the evolved distributions at the instants (a)  $t = 1.8 \text{ s}$ , (b)  $t = 3 \text{ s}$  and (c)  $t = 4.5 \text{ s}$ . The contour lines correspondingly have the same significance as in figure 21. (Adapted from [127]).

will thus end in  $|\neq, 0\rangle$  as well. Then only the repulsed branch in figure 20 is there so that the atom will be reflected with certainty. Here, too, matters change drastically as soon as the finite photon lifetime is accounted for (see figure 22). The comparison with figure 21 identifies the two main effects of the detuning: (i) it increases the reflection probability to 9.1%, i.e. roughly by a factor of two; (ii) it suppresses the large  $v$  contribution in the transmitted part, so that there is no gain in kinetic energy here, as we could have anticipated. Thus, photon dissipation reduces the reflection probability by a factor of ten, both on resonance (4.8% rather than 50%) and off resonance (9.1% rather than 100%).

### 6.2. The mazer

If the circumstances are such that dissipation can be ignored during the atom–photon interaction—which, as we state above, is very difficult to achieve in the microwave regime but might be possible in the optical domain—a particularly transparent description employs the formalism of the simple scattering theory. It focuses on the atomic centre-of-mass motion outside the resonator and uses a scattering matrix, of transmission and reflection coefficients, to account for the net effect of the atom–photon interaction.

For simplicity, we assume that there is no detuning, so that the dressed states  $|\gamma_0\rangle$ ,  $|\gamma_n^{(\pm)}\rangle$  are of the  $z$ -independent kind (6.3). Owing to this position independence, the atom–photon interaction introduces no coupling between the dressed states. The probability amplitudes  $\psi_0(z, t)$ ,  $\psi_n^{(\pm)}(z, t)$  therefore obey the one-dimensional decoupled Schrödinger equations,

$$\begin{aligned} i\hbar \frac{\partial}{\partial t} \psi_0(z, t) &= -\frac{\hbar^2}{2M} \frac{\partial^2}{\partial z^2} \psi_0(z, t), \\ i\hbar \frac{\partial}{\partial t} \psi_n^{(\pm)}(z, t) &= \left[ -\frac{\hbar^2}{2M} \frac{\partial^2}{\partial z^2} + \hbar\omega n \mp \hbar g(z)\sqrt{n} \right] \psi_n^{(\pm)}(z, t). \end{aligned} \quad (6.12)$$

They summarize in a formal way what has been observed above:  $\psi_0$  propagates as a free-particle amplitude does, and the amplitudes  $\psi_n^{(\pm)}(z, t)$  correspond to motion under forces derived from the potential energies  $\mp \hbar g(z)\sqrt{n}$ .

Upon switching to the time-independent amplitudes that refer to energy  $(\hbar k)^2/(2M) + n\hbar\omega$

$$\begin{aligned} \psi_0(z, t) &= \int_0^\infty dk \exp\left(-i\frac{\hbar k^2 t}{2M}\right) A_0(k, z), \\ \psi_n^{(\pm)}(z, t) &= \int_0^\infty dk \exp\left(-i\frac{\hbar k^2 t}{2M} - in\omega t\right) A_n^{(\pm)}(k, z), \end{aligned} \quad (6.13)$$

we incorporate the initial condition ‘atom approaching from the left’ by the ansatz

$$\begin{aligned} A_0(k, z) &= \alpha_0(k) \exp(ikz), \\ A_n^{(\pm)}(k, z) &= \alpha_n^{(\pm)}(k) \times \begin{cases} \exp(ikz) + \rho_n^{(\pm)} \exp(-ikz) & \text{for } z < 0 \text{ (‘to the left’),} \\ \tau_n^{(\pm)} \exp(ik(z-L)) & \text{for } z > L \text{ (‘to the right’),} \end{cases} \end{aligned} \quad (6.14)$$

where  $\rho_n^{(\pm)}$  are the reflection coefficients and  $\tau_n^{(\pm)}$  are the transmission coefficients, and the  $z$ -independent amplitudes  $\alpha_0(k)$ ,  $\alpha_n^{(\pm)}(k)$  are determined by the initial (i.e.  $t = 0$ ) wave functions  $\psi_0(z, 0)$ ,  $\psi_n^{(\pm)}(z, 0)$ .

The scattering coefficients  $\rho_n^{(\pm)}$ ,  $\tau_n^{(\pm)}$  depend on the shape of  $g(z)$ . For the idealized mesa function shape,

$$g(z) = \begin{cases} g & \text{if } 0 < z < L \text{ (‘inside’),} \\ 0 & \text{if } z < 0 \text{ or } z > L \text{ (‘outside’),} \end{cases} \quad (6.15)$$

they have well-known analytical forms [124, 128],

$$\begin{aligned} \tau_n^{(\pm)} &= \left[ \cos(k_n^{(\pm)} L) - \frac{i}{2} (k_n^{(\pm)}/k + k/k_n^{(\pm)}) \sin(k_n^{(\pm)} L) \right]^{-1}, \\ \rho_n^{(\pm)} &= \frac{i}{2} (k_n^{(\pm)}/k - k/k_n^{(\pm)}) \tau_n^{(\pm)}, \end{aligned} \quad (6.16)$$

which involve the modified wave numbers

$$k_n^{(\pm)} = \sqrt{k^2 \mp (2Mg/\hbar)\sqrt{n}} \quad (6.17)$$

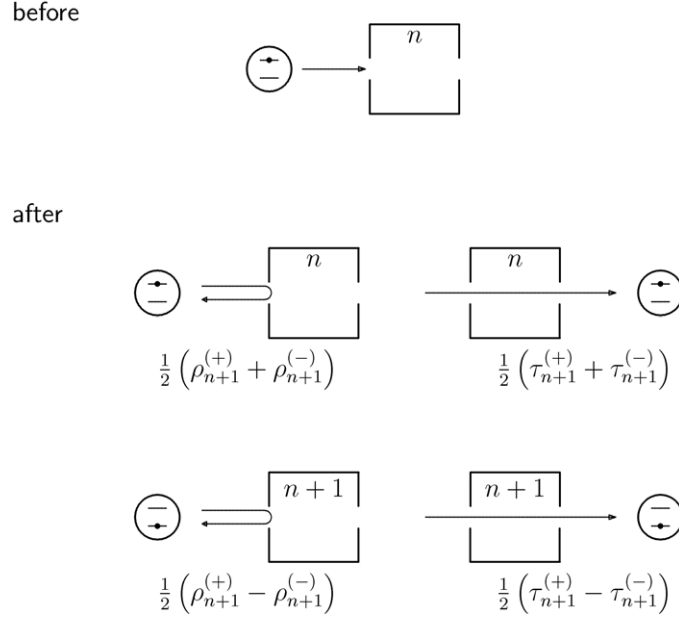


**Figure 23.** An excited atom is incident upon a cavity that contains  $n$  photons, so that there are  $n + 1$  excitations in the system. The atom is either reflected (left) or transmitted (right) with (top) or without (bottom) emitting another photon into the resonator. The respective probability amplitudes are indicated. (Adapted from [130].)

that apply inside the resonator. The coefficients corresponding to an attractive potential have  $k_n^{(+)} > k$ , which is always positive; but those corresponding to repulsion,  $k_n^{(-)}$ , can be imaginary, which happens for  $k^2 < (2Mg/\hbar)\sqrt{n}$ , i.e. when the interior of the cavity is a classically forbidden region and transmission occurs only as a result of tunnelling. It should be clear that these general features are equally true of shapes of  $g(z)$  other than the very simple mesa function (6.15), and explicit calculations confirm this [129], in particular also for the ‘cosh<sup>-2</sup> shape’ potential used for figures 20–22.

As sketched in figure 23 there are four possibilities open to an excited atom incident upon a cavity with  $n$  photons. We have  $|\mp, n\rangle = 2^{-1/2}(|\gamma_{n+1}^{(+)}\rangle + |\gamma_{n+1}^{(-)}\rangle)$ , and both dressed states can be reflected or transmitted, or put differently, the atom can be transmitted or reflected with or without emitting another photon into the resonator. Since  $|\mp, n+1\rangle = 2^{-1/2}(|\gamma_{n+1}^{(+)}\rangle - |\gamma_{n+1}^{(-)}\rangle)$ , the total emission probability is given by

$$P_{\text{emit}}(n) = \frac{1}{4} |\rho_{n+1}^{(+)} - \rho_{n+1}^{(-)}|^2 + \frac{1}{4} |\tau_{n+1}^{(+)} - \tau_{n+1}^{(-)}|^2, \quad (6.18)$$

which, of course, depends on  $k$  and must be integrated over the (small)  $k$  range specified by the initial centre-of-mass wave function of the approaching atom.

If all relevant  $k$  values are large on the scale set by the interaction energy,  $k^2 \gg (2Mg/\hbar)\sqrt{n}$ , then the shape of  $g(z)$  does not matter and one gets

$$P_{\text{emit}}(n) = \sin^2 \left( g \frac{L}{v} \sqrt{n+1} \right), \quad (6.19)$$

the familiar probability for Rabi oscillations, where  $v$  is the velocity associated with a typical  $k$  value ( $\hbar k = Mv$ ) of the small  $k$  range in question. Thus we arrive at the emission probability  $\mathcal{A}_n$  of the standard micromaser theory of section 4.2.

The other extreme is the limit of ultraslow atoms for which

$$P_{\text{emit}}(n) = \frac{1}{4} \frac{1 + 2 \sin(2\kappa_n L)}{1 + (\kappa_n/2k)^2 \sin^2(\kappa_n L)} \quad (6.20)$$

with  $\kappa_n^2 = (2Mg/\hbar)\sqrt{n+1}$  applies [130]; this approximation is valid for  $k^2 L \ll \kappa_n$  and  $\exp(\kappa_n L) \gg 1$ . Rather than being periodic in  $(g/v)L(n+1)^{1/2}$ , as the Rabi oscillations of equation (6.19) are, equation (6.20) is periodic in  $(2Mg/\hbar)^{1/2} L(n+1)^{1/4}$ . In fact, the emission probability (6.20) resembles the Airy function of classical optics,  $[1 + F \sin^2(\Delta/2)]^{-1}$ , for the transmitted intensity in a Fabry–Perot interferometer with finesse  $F$  and phase difference  $\Delta$ , where  $F = (\kappa_n/2L)^2$  and  $\Delta = 2\kappa_n L$  establish the correspondence.

There is an implicit assumption in the derivation of equation (6.20) that we need to comment on. It is helpful to recall, as typical values, the parameters of the Garching micromaser experiments ( $g = 44 \text{ krad s}^{-1}$ ,  $M = 1.4 \times 10^{-22} \text{ g}$ ,  $L = 2.5 \text{ mm}$ ) for which we have  $\kappa_n \simeq 10^5 \text{ cm}$  for  $n$  of the order of 1–10. Thus, in order to have a significant effect upon the centre-of-mass motion, the atom should have a velocity  $v$  of a few millimetres per second at most, corresponding to temperatures of about 100 nK. State-of-the-art cooling techniques [131] enable one to reach such temperatures but that alone is not enough. For the transition from equation (6.16) to equation (6.20) one also needs the velocity spread  $\delta v$  to be small on the scale set by the arguments of the trigonometric functions,  $\delta v/v \simeq 10^{-3}$  being a typical constraint that has to be obeyed [129]. This, however, requires velocity control beyond the present-day techniques. We must therefore average the squared amplitude differences of equation (6.18) over a small, but not tiny, velocity range [124] which replaces equation (6.20) by [129]

$$P_{\text{emit}} = \frac{1}{2} \left[ 1 - \frac{\sqrt{\kappa_n^2 + k^2} - k}{\sqrt{\kappa_n^2 + k^2} + k} \frac{\kappa_n^2}{2k\sqrt{\kappa_n^2 - k^2 - 2k^2 + \kappa_n^2}} \right], \quad (6.21)$$

with  $k$  now standing for the mean velocity. As a consequence of this averaging, the sharp resonances of the Fabry–Perot type that were present in equation (6.20) are smeared out and the emission probability (equation (6.21)) is independent of  $L$ . Indeed, as we see in figure 24, there is also very little dependence on  $n$ , the number of photons present upon arrival of the atom.

There is also no trace of the Rabi oscillations of equation (6.18), which are of such great importance for the dynamics of the micromaser. In the new velocity regime, in which the quantum properties of the atom's centre-of-mass motion are significant, we speak of 'microwave amplification via z-motion-induced emission of radiation'—it is the *mazer* regime. Clearly, micromazer dynamics is quite different from micromaser dynamics.

In view of what we remarked about the velocity regime, the realization of an actual mazer cannot be achieved by just operating an ordinary micromaser with very slow atoms, even if we continue to disregard the damaging effects of dissipation. The gravitational pull increases the velocity of the atoms by about  $10^4 \text{ mm s}^{-1}$  within a second, so that we leave the mazer regime before the atom had a chance to get through the cavity (the  $z$  direction would have to be vertical, of course). So either one turns to the optical domain, where parameters are more encouraging [129], or one makes use of cavities of rather different geometries, such as re-entrant resonators [132], for which a microwave experiment appears feasible too [129]. For details concerning these matters and other properties of the mazer, such as the spectrum of the radiation that builds up when many successive ultraslow atoms are sent through the cavity, the reader should consult the pertinent literature [128–130, 133–138].

## 7. Cavity QED experiments in the visible spectral region

The QED experiments in the optical region aimed at achieving strong coupling between atom and cavity field started in the early 1990s with experiments involving atomic beam transits

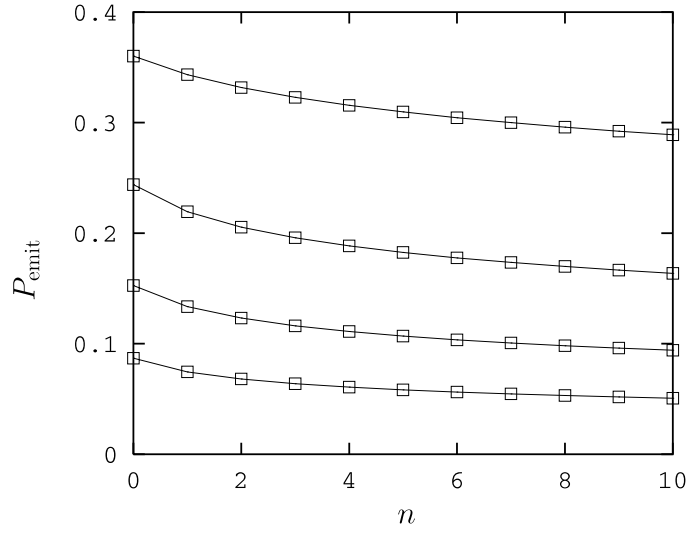


**Figure 24.** Emission probability (6.21) for  $n = 0, \dots, 10$ . The lines connecting the integer  $n$  values are drawn just to guide the eye. From top to bottom, the four sets of probabilities refer to  $k/(2Mg/h)^{1/2} = 0.5, 0.2, 0.1, 0.05$ , respectively.

through the mode of a high-finesse cavity [140, 58]. The flux of atoms was small enough to make the average intracavity number roughly one. The one-atom vacuum Rabi splitting for the Cs transition ( $6S_{1/2}, F = 4 \rightarrow 6P_{3/2}, F' = 5'$ ) was observed. Similar observations were made by Feld *et al* using Ba atoms [141]. The brief interaction time was a limitation in these experiments, and so subsequent experiments with clouds of cold atoms cooled to sub-Doppler temperatures were prepared in a magneto-optical trap (MOT) located a few millimeters above the cavity and released into the cavity. It was possible to observe in real time their individual trajectories and the duration of their transits [142]. This technique was used to extract the vacuum Rabi spectrum from the transmission of a weak probe.

### 7.1. The one-atom laser

The one-atom laser is the optical analog of the one-atom maser. It has been theoretically discussed in many papers [143–148, 195–198]. The gain medium is a single atom which couples photons into the resonant mode of the optical cavity. As expected, it is very different from a conventional and semiclassical laser and shows a variety of quantum properties.

The first laser oscillation with a single atom was observed by An *et al* [49]. In this experiment a beam of Ba atoms transverses a single mode cavity with a finesse of  $8 \times 10^5$ . The atoms are excited by a  $\pi$ -pulse from the  $^1S_0$  ground state to the  $^3P_1$  excited state before they enter the cavity. The mean number of photons inside the cavity was 0.14–11.

In a recent experiment [149, 150] a Raman-type transition was investigated where a pump beam from the ( $6S_{1/2}, F = 3$ ) ground state of the Cs atom to the ( $6P_{3/2}, F' = 3'$ ) excited state is applied perpendicular to the cavity. The atomic population is transferred to ( $6S_{1/2}, F = 4$ ) via strong coupling to the cavity emitting a single excitation in the laser mode. A repumping beam is necessary to bring the population in the  $6S_{1/2} F = 4$  state back to the ground state. With the set-up thresholdless lasing is observed. Furthermore, the one-atom laser exhibits photon antibunching and sub-Poissonian photon statistics. For further work on the one-atom laser see section 7.4.

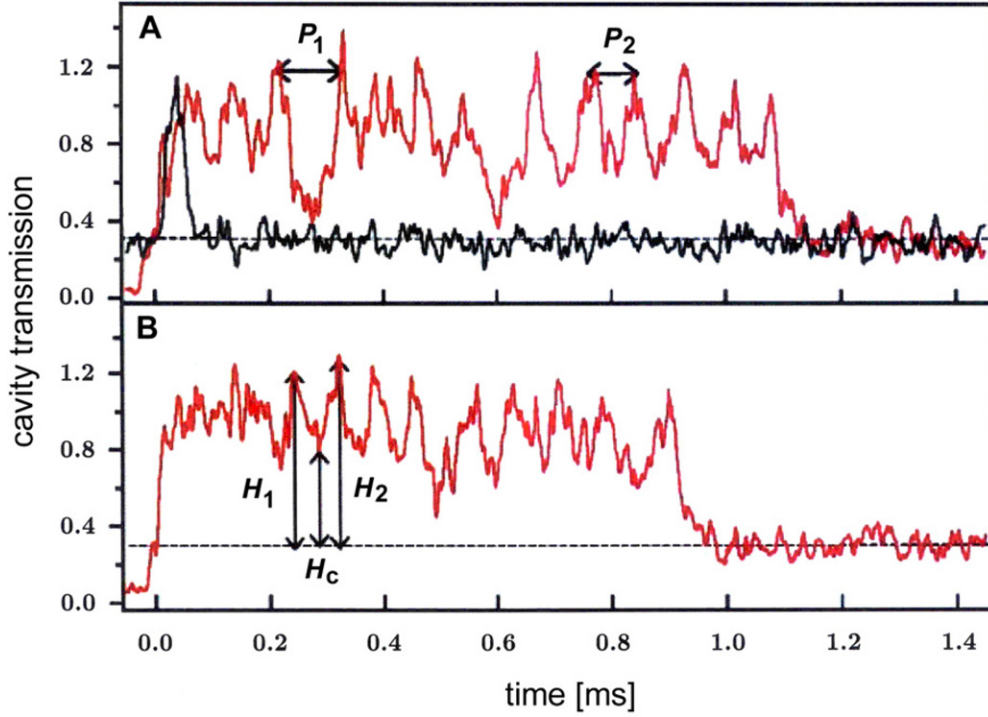


**Figure 25.** Single atom observed while traversing an optical resonator in the CalTech experiment. The cavity transmission is shown as a function of time while an atom traverses the optical resonator. The dashed lines in A and B indicate the system's response when there is no atom in the cavity. For comparison, the solid line in B refers to an atom that does not get trapped in transit. The trapped atoms oscillate in the transverse directions, with longer periods and larger amplitudes ( $P_1$  in A) or shorter periods and smaller amplitudes ( $P_2$  in A). A normalized amplitude parameter  $A = (H_1 + H_2 - 2H_c)/(H_1 + H_2)$  can be extracted as indicated in B, and it agrees reasonably well with theoretical values; for details consult [139] from which the figure has been adapted.

## 7.2. Atoms pushed by a few photons

The attractive potential in which the dressed states  $|\gamma_n^{(+)}\rangle$  of section 6.1 move suggests that one could trap neutral atoms in potential wells of this kind, thereby exploiting the forces of just a few photons. This has indeed been suggested in [125]. The gravitational pull just mentioned is, however, much too strong. It cannot be compensated for by the forces that a few microwave photons could provide, and so one would need the microgravity environment of a satellite experiment to demonstrate the reality of these forces.

Circumstances are much more favourable in the optical domain. The light field of a small high-finesse optical resonator can catch a slowly moving atom. This was recently demonstrated in two experiments, one performed with caesium atoms at Caltech [139], the other with rubidium atoms at Garching [151]. The non-technical report by Rempe on these experiments is recommended reading [152].

In both experiments, single atoms were trapped by one or a few photons and, very impressively, the motion of the atom was tracked by analysing the light transmitted through the resonator; see figures 25 and 26. If one thinks of individual light quanta that enter the resonator through one highly reflective mirror, leave through the other, and bounce back and

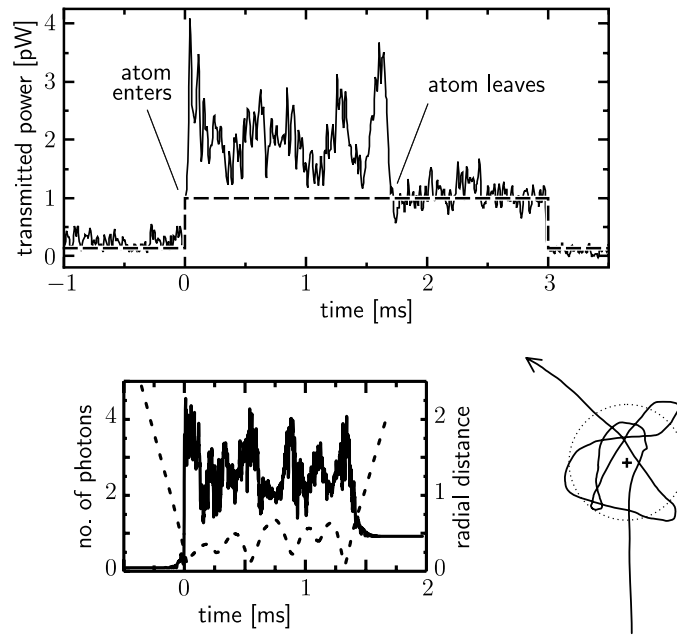


**Figure 26.** Single atom observed while traversing an optical resonator at Garching. Top: atom enters the resonator and stays inside for about 1.6 ms. The transmitted power is markedly increased by the atom; it drops to the empty-cavity value (---) after the atom leaves. Bottom: a simulated atom trajectory is shown on the right. The cross indicates the axis of the resonator; the dashed circle shows the beam waist. The solid line on the left shows the corresponding mean photon number in the resonator; the dashed curve shows the atom's distance from the resonator axis (in units of the diameter of the circle on the right). These plots are adapted from [151].

forth in the meantime in order to create the trapping potential, then these quanta complete ‘an almost record-breaking number of round trips’ [152].

The actual atom-light interaction in these experiments is considerably more complicated than what we sketched above. For example, one needs to take into account the fact that the atoms may scatter the photons out of the resonator, which gives rise to dissipative forces and creates the need for continuous feeding of low-intensity radiation into the resonator. A further discussion of such details is beyond the scope of this paper. We must not fail to mention, however, that the experimenters can control the experimental parameters so well that they are able to study quantitatively the radiation-induced interaction between two atoms that happen to get into the trapping potential at the same time [153].

This is a rapidly developing and intense field of research, both experimentally and theoretically, and we refer the interested reader to the pertinent publications of recent years [139, 151–159]. Let us just note that, in addition to the passive observation of the kind reported in figures 25 and 26, active feedback has been successfully implemented [159], allowing the experimenters to prolong the storage time of the atom substantially.

While atomic confinement with quantized QED field offers an important advance in obtaining well-localized, trapped atoms, it remains preferable to decouple the trap from the QED interaction. A number of groups [161–164] have therefore realized optical dipole force traps, also known as far off-resonant traps or FORTs. They use a far-detuned optical beam inducing a dissipative, attractive force on an atom and since they are operated far



off-resonance, they cause practically no atomic excitation. Examples where FORT traps were used in QED experiments are [161, 163, 165]. Using these arrangements allows one to keep an atom inside the cavity for a longer period, as was done in the experiments on single-photon generation [166] or on the one-atom laser [167].

Some considerable progress was recently made concerning the trapping time of an atom in a cavity [168]. In this paper it was shown that an orthogonal arrangement of cooling laser, trapping laser and cavity vacuum field gives rise to a combination of friction forces that act along all the three directions so that a single atom can be cooled in a high-finesse cavity, resulting in a trapping time of up to 17 s. In a subsequent paper [169] using the same set-up atoms were repetitively moved out and back into the cavity mode with a repositioning precision of 135 nm. This makes it possible either to selectively address one atom or a string of atoms by the cavity field or to simultaneously couple two precisely separated atoms to a higher mode of a cavity.

Raman transitions have also been used to cool atoms in a cavity. This method was used to investigate the vacuum Rabi spectrum for one and the same atom, as opposed to other experiments using a FORT [58, 170, 171] requiring averaging over a large ensemble of atoms. In the experiment investigating the Rabi splitting a single atom loaded into the FORT is irradiated with a probe beam whose frequency is varied over a range near the atom-cavity resonance, and the transmission of the probe beam is measured. This measurement cycle has to be interated with Raman cooling periods. The result agrees very well with the solution of the steady-state master equation of the system [172].

### 7.3. Single-photon sources

The controlled production of single photons is of fundamental and practical interest; they represent the lowest excited quantum states of the radiation field and have applications in quantum cryptography [173] and quantum information processing [174]. Common approaches use the fluorescence of single ions [175], single molecules [176, 177], colour centres [178, 179] and semiconductor quantum dots [180–184]. However, the lack of control over such irreversible emission processes precludes the use of these sources in applications (such as quantum networks [185]) that require coherent exchange of quantum states between atoms and photons. The necessary control may be achieved, in principle, in cavity quantum electrodynamics. In these systems the directed emission can be controlled through the modes of the cavity.

Sources of this kind have been proposed by different authors, e.g. [186–189]. All these schemes are based on a technique known as STIRAP (stimulated Raman scattering involving adiabatic passage) [190, 191] or variants thereof. The first observation of stimulated Raman scattering from a  $\Lambda$ -type three-level atom where the vacuum field of a high-finesse optical cavity is involved was realized by Hennrich *et al* [156]. This scheme produces from a single atom one intracavity photon by means of an adiabatic passage sequence consisting of pump laser and cavity field. This photon is transmitted through a less reflecting mirror of the cavity. The transitions used were between hyperfine levels of the  $^{85}\text{Rb}$  atom. The atoms used were pre-cooled in a MOT and released into the cavity. The experiment produced at most one photon per passing atom but did not operate as a single photon source, since the continuous driving scheme simply mapped the random (Poissonian) atom statistics to the photons. This was later improved in a further experiment where pulsed driving was used together with pulsed recycling to allow a stream of several single-photon pulses to be produced on demand from one and the same atom, triggered by the detection of a first photon emitted from the cavity [192].

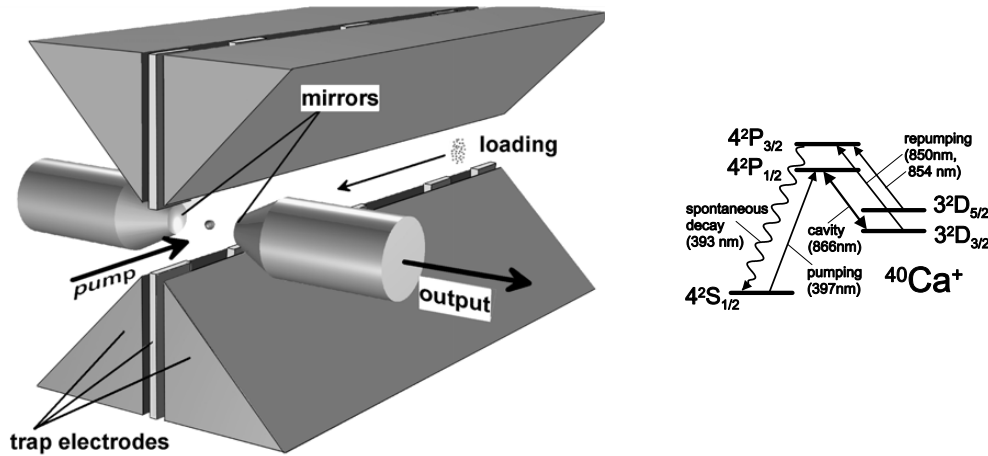


**Figure 27.** Left: set-up of the  $^{40}\text{Ca}^+$  ion trap laser at Garching. The loading trap at the rear is used to catch ions and cool them. A single ion is then transferred to the front trap between the mirrors of the optical cavity, where the ion is pumped and emits into the resonant resonator mode. (Reproduced from [160].) Right: level scheme. The lasing transition is  $4^2\text{P}_{1/2} \rightarrow 3^2\text{D}_{3/2}$ ; the major pump transition is  $4^2\text{S}_{1/2} \rightarrow 4^2\text{P}_{1/2}$ ; the (re-)pumping from levels  $3^2\text{D}_{3/2}$  and  $3^2\text{D}_{5/2}$  to  $4^2\text{P}_{3/2}$  prevents the accumulation of population in dead ends; spontaneous decay from  $4^2\text{P}_{3/2}$  to the  $4^2\text{S}_{1/2}$  ground state closes the cycle.

#### 7.4. Single-atom laser using an ion trap

The ultimate limit of ultra-slowly moving atoms are atoms at rest. A single atom that stays put inside a high- $Q$  resonator will interact with the cavity mode for a long time and, provided the atom is suitably driven, may play the role of the active medium of a laser. This is the situation of the *one-atom laser*. Theoretical studies [193–195] eventually confirmed that it is indeed possible to get laser operation with a single atom, as discussed in section 7.1. Actual realization would require appropriate mechanical forces to keep the atom in place and such forces are not easily provided.

A much more practical variant of this idea is therefore the *ion-trap laser* [196], where the active medium is a single ion trapped in a standard ion trap around which one positions the mirrors of the optical resonator; see figure 27. Careful studies [197–200] demonstrate that the  $^{40}\text{Ca}^+$  ion is well suited to this purpose. One finds, for example, that a mean number of 5–10 photons builds up in the resonator (which corresponds to about  $5 \times 10^5$  photons coupled out per second) and that, in some parameter ranges, the photon statistics may be sub-Poissonian. Experiments for actual realization of an ion-trap laser of this kind are well under way at Garching.

The strength of the ion-photon coupling depends on the location of the ion relative to the nodes and anti-nodes of the mode function in question. It is therefore mandatory to have good control of the ion's position. In fact, the experimenters are able to push the ion around at will (or, equivalently, to change the mirror positions), as demonstrated by the measurement reported in figure 28. This plot shows a two-dimensional map of the mode function obtained by recording the fluorescence light while scanning the ion's position across a plane perpendicular to the resonator axis. The trapped ion can thus serve as a high-resolution probe of the optical field inside the cavity [160]. Owing to the rest motion of the trapped ion a resolution of the order of 40 nm has been achieved. The permanent and fully controllable coupling of a particle to the field with a well-defined strength is a unique property of the ion-trap cavity quantum

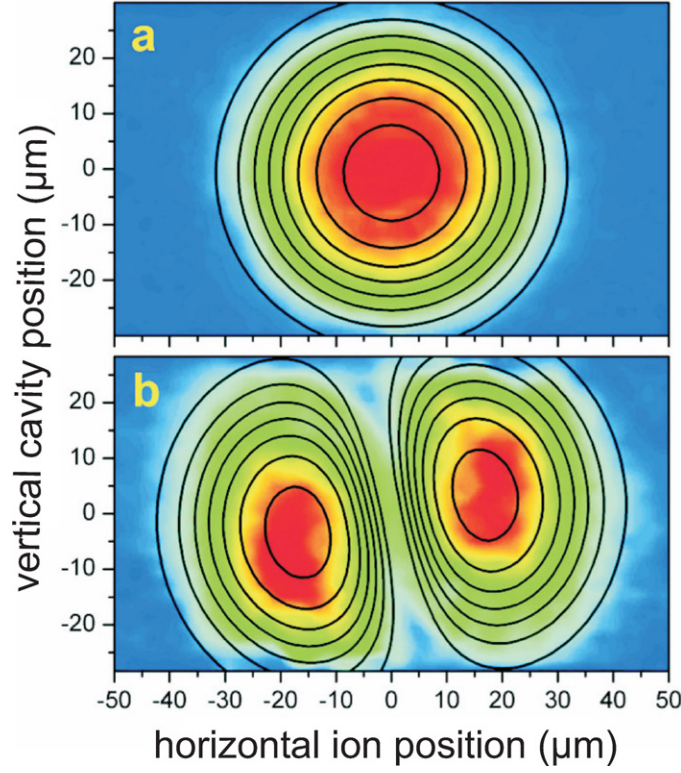


**Figure 28.** Two-dimensional images of the cavity field taken over an area of  $100 \times 60 \mu\text{m}^2$ . (a) TEM<sub>00</sub> mode. (b) TEM<sub>01</sub> mode. In the horizontal direction the ion was moved, while vertically the cavity position was changed relatively to the ion. False colors represent the measured fluorescence count rate; the contour lines indicate the theoretical fluorescence pattern. This figure is taken from [201].

electrodynamics and provides the basis for the ion-cavity experiments described here. In the following, we would like to discuss a single photon source on the basis of a trapped single ion, see figure 29.

The first step of the protocol for generating a single-photon pulse is to apply radiation at 397 and 866 nm for  $3 \mu\text{s}$  from the side of the cavity to laser-cool the ion and thus ensure its proper localization. Subsequently, the initial electronic state  $S_{1/2}$  is prepared by optical pumping at 866 nm for  $0.5 \mu\text{s}$ . A single photon is produced by driving a cavity-assisted Raman transition to the  $D_{3/2}$  level by means of a pump pulse at 397 nm with a predefined intensity profile of up to  $6 \mu\text{s}$  duration. The sequence is repeated at a rate of 100 kHz. The photon pulse is emitted from the cavity through one mirror with a transmissivity of 600 ppm, 100 times larger than that of the opposite mirror. The Gaussian mode emanating from this mirror is focused on an avalanche photodiode (APD) after passing a series of four optical filters and a spatial filter. In this manner, light from an auxiliary laser used for locking the cavity length and from other sources of stray light is reduced to a level well below the dark-count rate of the detectors used.

With the position of the ion and hence the ion-field coupling fixed, the distribution of photon detection times exactly follows the shape of the single-photon pulse. By tailoring the intensity profile of the driving pulse, we can imprint an arbitrary temporal structure on the waveform of the photon, which is then precisely reproduced in every emission event. The

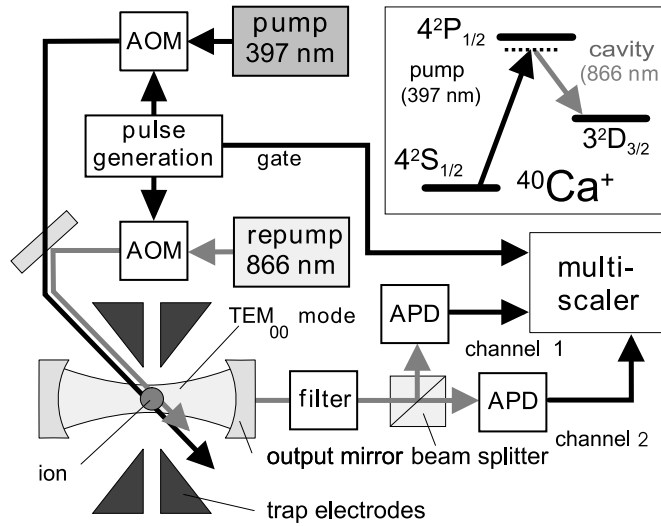


**Figure 29.** Experimental set-up outlining the excitation and detection scheme for single photons. Not shown is an additional laser at 894 nm which is resonant with a cavity mode not coupled to the ion and which is used for stabilizing the cavity length. In the path to the detectors, this locking beam is suppressed by a series of filters, providing an attenuation of  $10^{11}$  at 894 nm. The laser intensities are controlled with acousto-optic modulators (AOMs). The inset shows the relevant levels of the  $^{40}\text{Ca}^+$  ion used for single-photon production. The pump laser and cavity are red-detuned with respect to the  $P_{1/2}$  level. This figure is taken from [201].

single-photon pulse shape is extracted from the time records by accumulating the probability distribution of photon arrival times relative to the pump-pulse trigger. Experimental data obtained for intense Gaussian pumping based on the evaluation of over 400 000 photons continuously generated from a single ion are presented in figure 30(a). Because the photon pulses are identical, the time distributions obtained constitute a measurement of the waveform of a single photon. This is confirmed by comparing the data with calculated single-photon pulse shapes, based on coherent Raman coupling of a calcium ion to a single cavity mode [201].

Figure 30(b) shows a symmetric Gaussian output pulse generated with a weak Gaussian pump pulse. The arbitrary control of the photon pulse shape in the set-up is limited only by the time constants associated with ion and cavity dynamics. This is apparent from the response of the system to a pump pulse with a square profile (figure 30(c)). The trailing edge of the pulse decreases exponentially at the cavity decay rate, whereas the onset of the pulse is delayed by the time required to excite the electronic transition. As an example of a more complex pulse shape, we generated a twin-peaked single-photon pulse (figure 30(d)). The photon detection times are distributed over two well-separated maxima, reflecting the structure of the pump pulse. Spreading a single photon over two distinct time bins may be exploited as a way to encode quantum information in the time domain [202].

Apart from the control of the photon's waveform and the suppression of two-photon events, an important accomplishment for applications in quantum information processing is the continuous, uninterrupted operation of our source, allowing correlations to be measured on very long time scales. Figure 31(a) shows a measurement of correlations sampled over a time of 90 min. The linear decrease in the envelope of the correlation function is a consequence of the finite duration of the measurement. No individual lines are resolved on the time scale shown, but when an arbitrary point on the time axis is zoomed in, the same peak structure is found as in figure 32 on either side of the origin. As an example, figure 31(b) shows correlations between

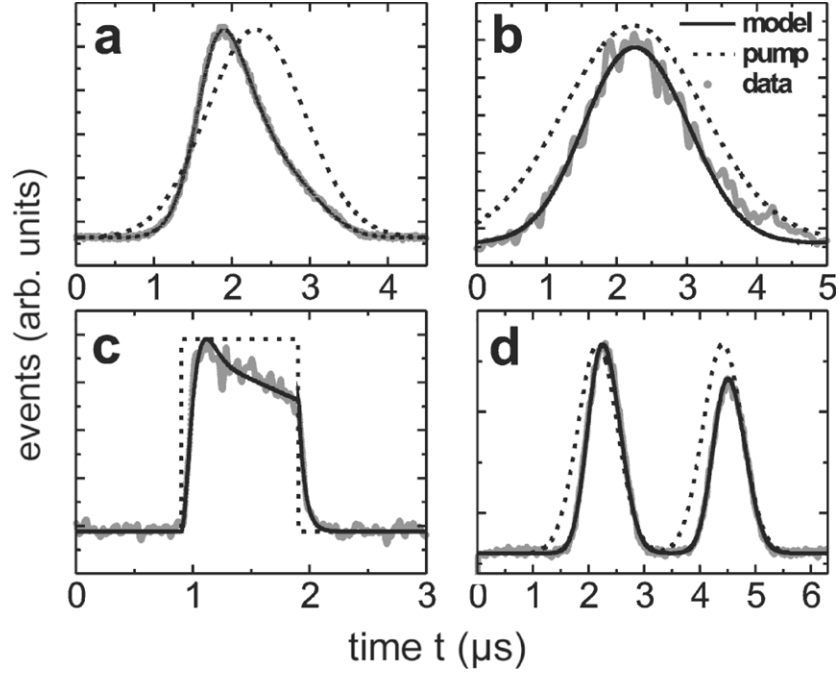


**Figure 30.** Single-photon pulse shapes (grey line) for different pump laser profiles, indicated by the dotted line (not to scale). (a) Strong Gaussian pump. (b) Weak Gaussian pump. (c) Square-wave pump. (d) Double-peaked pump. The superimposed black curves show the results of a density-matrix calculation, taking into account the full Zeeman structure of the  $^{40}\text{Ca}^+$  levels, as well as the polarization of the optical fields. Plots (a) and (d), obtained with the best statistics, demonstrate the nearly perfect agreement between the model and the experimental data, confirming that the waveform of a single photon can be deterministically controlled. In (a) and (d) the experimental and theoretical curves are practically identical so that they do not show up as separate curves. This figure is taken from [201].

photons detected 20 min apart. The operation of the system for 90 min represents the longest continuous generation of single photons from an atomic source [203]. With ion trapping times of many hours, single-photon emission in the described system can be maintained for even longer periods.

The striking feature of this new single photon source is the fact that it is possible not only to generate a photon on demand or deterministically but also to preselect the duration of the generated photon wavepacket. The latter means that the coherence length of the photon can be preselected. These properties of the single photon source described here will make it a unique source for many applications. The coupling of ions and photons in a controlled way is required in schemes linking optical long-distance quantum communication with ion-trap quantum processors, both of which have been successfully demonstrated in the past. The result could be a quantum version of the internet in which local processing sites are connected with each other by photonic channels.

## 8. Conclusions and outlook

This paper reviews the work on cavity quantum electrodynamics with free atoms. Emphasis is placed on the work performed with the one-atom maser in our laboratory, but a survey on the

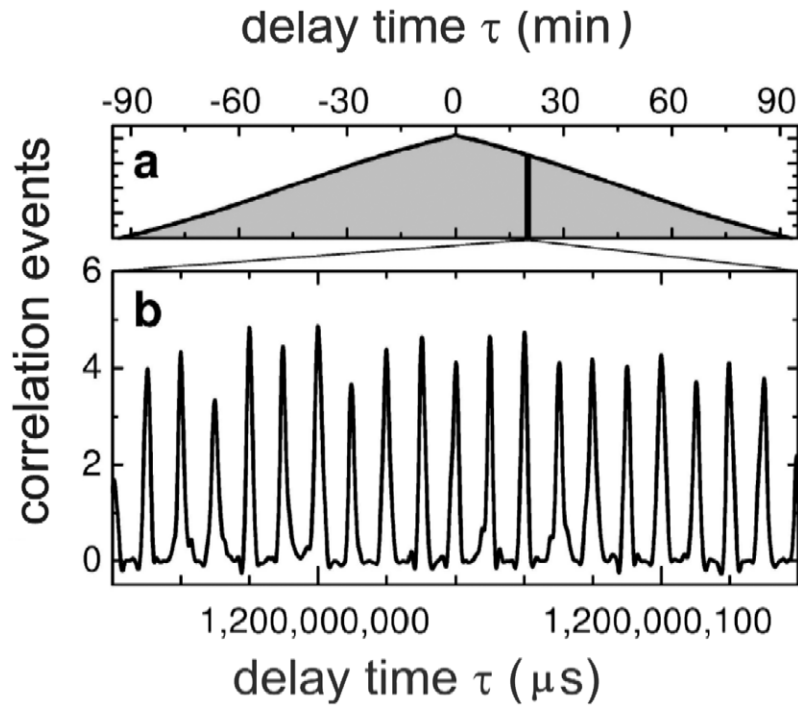


**Figure 31.** Long-term correlations of photon arrival times at the two detectors. (a) Envelope of two-photon correlations recorded over the entire sampling interval, demonstrating the continuous emission of single photons in our system. (b) Zooming in at a delay of  $\tau = 20$  min reveals individual peaks as in figure 32 for  $\tau \neq 0$ . This figure is taken from [201].

work done in other laboratories is also given in order to show the large variety of problems being treated with the very fundamental system of an atom interacting with a single mode of a cavity.

The experiments on cavity quantum electrodynamics started with studies of free atoms, but meanwhile the field has expanded to include solid-state systems, as briefly discussed in the review. Furthermore, new applications are emerging in various directions. First, there are interesting developments of new cavity structures which are leading to new possibilities [204, 205, 206]. A further active field is cavity quantum electrodynamics in semiconductors in combination with quantum dots or semiconductor microcavity structures [64, 207]. The latter systems promise application in many areas of optical communication and possibly also in quantum information processing.

The experiments with free atoms will also be further developed. Interesting results may be expected especially in connection with studies of decoherence. The cavity quantum electrodynamic systems with free atoms seem to be the only ones where the phenomenon can be investigated in detail and free of perturbing influences. Furthermore, in connection with the one-atom maser another interesting problem under study is the investigation of the phase diffusion of the maser field.

Phase diffusion of a maser or laser determines the natural linewidth of these systems. In the standard maser/laser, this is caused by spontaneous transitions. In the one-atom maser, spontaneous transitions play no role; there it is the thermal noise which determines the phase diffusion. As this parameter can easily be controlled by changing the cavity temperature, this phenomenon can be properly investigated. The exploration of phase diffusion is also interesting



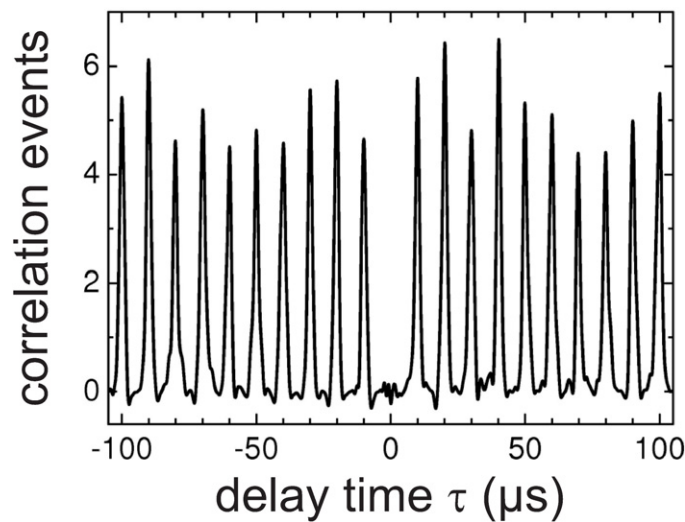


**Figure 32.** Cross-correlations of photon arrival times at the two detectors (counts in 100 ns time bins) around zero delay. Dark-count events were eliminated with the help of an independent measurement for data including dark-counts). The absence of a peak at  $\tau = 0$  confirms that the source emits single photons. This figure is taken from [201].

in the vicinity of trapping states, which were described in section 4.5. As shown, the trapping states display the quantum states of the maser field. The behaviour of phase diffusion should therefore follow the amplitude-phase uncertainty when the field approaches a trapping state. This phenomenon should be measurable with the available set-up [104].

From the few examples given in this outlook it is obvious that the field of cavity quantum electrodynamics will continue in the future to be as interesting and lively as it has been in the past.

### Acknowledgments

The one-atom maser and the trapped ion work is supported by the European Community and the Quantum Information Highway A8 project of the State of Bavaria, Germany. BGE wishes to acknowledge the very kind hospitality extended to him by the Quantum Optics Institute in Garching.

### References

- [1] Berestetskii V B, Lifshitz E M and Pitaevskii L P 1982 *Quantum Electrodynamics* (Oxford: Pergamon)
- [2] Barton G 1970 *Proc. R. Soc. Lond. A* **320** 251–75
- [3] Stehle P 1970 *Phys. Rev. A* **2** 102–6
- [4] Drexhage K H 1974 *Progress in Optics* vol 12 ed E Wolf (Amsterdam: North Holland) pp 165–229
- [5] Milonni P W and Knight P L 1973 *Opt. Commun.* **9** 119–22
- [6] Power E A and Thirunamachandran T 1982 *Phys. Rev. A* **25** 2473–84
- [7] Haroche S and Raimond J M 1985 *Advances in Atomic, Molecular and Optical Physics* vol 20, ed D Bates and B Bederson (New York: Academic) pp 350–411
- [8] Gallas J A C, Leuchs G, Walther H and Figger H 1985 *Advances in Atomic, Molecular and Optical Physics* vol 20, ed D Bates and B Bederson (New York: Academic) pp 413–66
- [9] Purcell E M 1946 *Phys. Rev.* **69** 681 (note B10)



- [10] Power E M 1964 *Introductory Quantum Electrodynamics* (New York: Elsevier)
- [11] De Martini F, Innocenti G, Jacobovitz G and Mantolini P 1987 *Phys. Rev. Lett.* **59** 2955–8
- [12] Gabrielse G and Dehmelt H 1985 *Phys. Rev. Lett.* **55** 67–70
- [13] Hulet R G, Hilfer E and Kleppner D 1985 *Phys. Rev. Lett.* **55** 2137–40
- [14] Jhe W, Anderson A, Hinds E A, Meschede D, Moi L and Haroche S 1987 *Phys. Rev. Lett.* **58** 666–9
- [15] Kleppner D 1981 *Phys. Rev.* **47** 233–6
- [16] Goy P, Raimond J M, Gross M and Haroche S 1983 *Phys. Rev. Lett.* **50** 1903–6
- [17] Heinzen D J, Childs J L, Thomas J and Feld M S 1987 *Phys. Rev. Lett.* **58** 1320–3
- [18] Heinzen D J and Feld M S 1987 *Phys. Rev. Lett.* **59** 2623–6
- [19] Yamamoto Y, Machida S, Igeta K and Björk G 1991 Controlled spontaneous emission in microcavity semiconductor lasers *Coherence, Amplification and Quantum Effects in Semiconductor Lasers* ed Y Yamamoto (New York: Wiley) pp 561–615
- [20] Yablonovitch E 1987 *Phys. Rev. Lett.* **58** 2059–62
- [21] Yablonovitch E, Gmitter T J and Bhat R 1988 *Phys. Rev. Lett.* **61** 2546–9
- [22] Yablonovitch E and Gmitter T J 1989 *Phys. Rev. Lett.* **63** 1950–3
- [23] Bethe H A 1947 *Phys. Rev.* **72** 339–41
- [24] Casimir H B G and Polder D 1948 *Phys. Rev.* **73** 360–72
- [25] Casimir H B G 1948 *Proc. Koninkl. Ned. Akad. Wetenschap* **51** 793–5
- [26] Hinds E A 1991 *Advances in Atomic, Molecular and Optical Physics* vol 28, ed D Bates and B Bederson (New York: Academic) pp 237–89
- [27] Meschede D 1992 *Phys. Rep.* **211** 201–50
- [28] Barton G 1987 *Proc. R. Soc. Lond. A* **410** 141–74
- [29] Hinds E A 1994 Perturbative cavity quantum electrodynamics *Supplement 2 to Advances in Atomic, Molecular, and Optical Physics* ed P R Berman (New York: Academic) pp 1–56
- [30] Lütken C A and Ravndal F 1985 *Phys. Rev. A* **31** 2082–90  
Haroche S 1992 Fundamental quantum systems in quantum optics *Proc. Les Houches Summer School Session LIII (Les Houches, France)* ed J Dallibard *et al* (Amsterdam: North-Holland)
- [31] Barton G 1987 *Proc. R. Soc. Lond. A* **410** 175–200
- [32] Dobiasch P and Walther H 1985 *Ann. Phys. Fr.* **10** 825–43
- [33] Sukenic C I *et al* 1993 *Phys. Rev. Lett.* **70** 560–3
- [34] Brune M *et al* 1994 *Phys. Rev. Lett.* **72** 3339–42
- [35] Marroco M, Weidinger M, Sang R T and Walther H 1998 *Phys. Rev. Lett.* **81** 5784–7
- [36] Ramsey N F 1956 *Molecular Beams* (New York: Oxford University Press)
- [37] Dirscherl J, Neizert B, Wegener T and Walther H 1992 *Opt. Commun.* **91** 131–9
- [38] The experimental scheme has already been outlined in Walther H 1993 Atom physics *ICAP XIII* ed H Walther *et al* (New York: AIP)  
Wegener T 1994 *PhD Thesis* LMU Munich
- [39] Barton G 1988 *Phys. Scr.* **T21** 11–17
- [40] Lamoreaux S K 1997 *Phys. Rev. Lett.* **78** 5–8
- [41] Mohideen U and Anushree R 1998 *Phys. Rev. Lett.* **81** 4549–52
- [42] Bressi G, Carugno G, Onofrio R and Ruoso G 2002 *Phys. Rev. Lett.* **88** 041804
- [43] Chen F and Mohideen U 2002 *Phys. Rev. Lett.* **88** 101801
- [44] Jaynes E T and Cummings F W 1963 *Proc. IEEE* **51** 89–109
- [45] Kimble H J, Carnal O, Georgiades N, Mabuchi H, Polzik E S, Thomson R J and Turchette Q A 1995 Quantum optics with strong coupling *Atomic Physics* vol 14, ed D J Wineland *et al* (New York: AIP) pp 314–35
- [46] Hood C J, Lynn T W, Chapman M S, Mabuchi H, Ye J and Kimble H J 1999 Cavity QED—where's the Q? *Confined Photon Systems* ed H Benisty *et al* (*Lecture Notes in Physics* vol 531) (Berlin: Springer) pp 298–309
- [47] Brune M, Raimond J M, Goy P, Davidovich L and Haroche S 1987 *Phys. Rev. Lett.* **59** 1899–902
- [48] Meschede D, Walther H and Müller G 1985 *Phys. Rev. Lett.* **54** 551–4
- [49] An K, Childs J J, Dasari R R and Feld M S 1994 *Phys. Rev. Lett.* **73** 3375–8
- [50] Weidinger M, Varcoe B T H, Heerlein R and Walther H 1999 *Phys. Rev. Lett.* **82** 3795–8
- [51] Varcoe B T H, Brattke S, Weidinger M and Walther H 2000 *Nature (London)* **403** 743–6
- [52] Rempe G, Walther H and Klein N 1987 *Phys. Rev. Lett.* **58** 353–6
- [53] Rempe G, Schmidt-Kaler F and Walther H 1990 *Phys. Rev. Lett.* **64** 2783–6
- [54] Hagley E, Maître X, Nogues G, Wunderlich C, Brune M, Raimond J M and Haroche S 1997 *Phys. Rev. Lett.* **79** 1–5

- [55] Maître X, Hagley E, Nogues G, Wunderlich C, Goy P, Brune M, Raimond J M and Haroche S 1997 *Phys. Rev. Lett.* **79** 769–72
- [56] Nogues G, Rauschenbeutel A, Osnaghi S, Brune M, Raimond J M and Haroche S 1999 *Nature (London)* **400** 239–42
- [57] Rauschenbeutel A, Nogues G, Osnaghi S, Bertet P, Brune M, Raimond J M and Haroche S 2000 *Science* **288** 2024–8
- [58] Thompson R J, Rempe G and Kimble H J 1992 *Phys. Rev. Lett.* **68** 1132–5
- [59] Wehner E, Seno R, Sterpi N, Englert B-G and Walther H 1994 *Opt. Commun.* **110** 655–69
- [60] Nogues G, Rauschenbeutel A, Osnaghi S, Brune M, Raimond J M and Haroche S 1999 *Nature (London)* **400** 239–42
- [61] Imamoglu A, Awschalom D D, Burkard G, DiVincenzo D P, Loss D, Sherwin M and Small A 1999 *Phys. Rev. Lett.* **83** 4204–7
- [62] Sherwin M, Imamoglu A and Montrag T 1999 *Phys. Rev. A* **60** 3508–14
- [63] Solomon G S, Pelton M and Yamamoto Y 2001 *Phys. Rev. Lett.* **86** 3903–6
- [64] Yamamoto Y, Tassone F and Cao H 2000 Semiconductor cavity quantum electrodynamics *Springer Tracts in Modern Physics* vol 169 (Berlin: Springer)
- [65] Oxborrow M and Sinclair A G 2005 *Contemp. Phys.* **46** 173–206
- [66] Hong C K and Mandel L 1986 *Phys. Rev. Lett.* **56** 58–60
- [67] Haroche S and Raimond J M 1994 Manipulation of nonclassical field states in a cavity by atom interferometry *Supplement 2 to Advances in Atomic, Molecular, and Optical Physics* ed P R Berman (New York: Academic) pp 123–69
- [68] Raitzel G, Wagner C, Walther H, Narducci L M and Scully M O 1994 The micromaser: a proving ground for quantum physics *Supplement 2 to Advances in Atomic, Molecular and Optical Physics* ed P R Berman (New York: Academic) pp 57–121
- [69] Varcoe B T H, Brattke S and Walther H 2000 *Fortschr. Phys.* **48** 679–87
- [70] Brattke S 2001 *Untersuchungen von Photonenzuständen mit dem Ein-Atom-Maser* (Garching: MPQ Report 260)
- [71] Varcoe B T H, Hall B, Johnson G, Johnson P, MacGillivray W R and Standage M C 2000 *J. Meas. Sci. Technol.* **11** N111–16
- [72] Reshetov V A and Yevseyev I V 2000 *Laser Phys.* **10** 916–22
- [73] Orszag M, Ramirez R, Retamal J C and Saavedra C 1994 *Phys. Rev. A* **49** 2933–7
- [74] Kolobov M E and Haake F 1997 *Phys. Rev. A* **55** 3033–41
- [75] Casagrande F, Garavaglia M and Lulli A 1998 *Opt. Commun.* **151** 395–405
- [76] Casagrande F, Lulli A and Ulzega S 1999 *Phys. Rev. A* **60** 133–41
- [77] Filipowicz P, Javanainen J and Meystre P 1986 *Phys. Rev. A* **34** 3077–87
- [78] Lugiato L A, Scully M O and Walther H 1987 *Phys. Rev. A* **36** 740–3
- [79] Meystre P and Sargent M III 1990 *Elements of Quantum Optics* (Berlin: Springer)
- [80] Scully M O and Zubairy M S 1997 *Quantum Optics* (Cambridge: Cambridge University Press)
- [81] Englert B-G 1994/2002 Elements of micromaser physics *Preprint* [quant-ph/0203052](https://arxiv.org/abs/quant-ph/0203052)
- [82] Fano U 1947 *Phys. Rev.* **72** 26–9
- [83] Mandel L 1979 *Opt. Lett.* **4** 205–7
- [84] Eberly J H, Narozhny N B and Sanchez-Mondragon J J 1980 *Phys. Rev. Lett.* **44** 1323–6
- [85] Elmfors P, Lautrup B and Skagerstam B-S 1996 *Phys. Rev. A* **54** 5171–92
- [86] Brune M, Schmidt-Kaler F, Maali A, Dreyer J, Hagley E, Raimond J M and Haroche S 1996 *Phys. Rev. Lett.* **76** 1800–3
- [87] Briegel H-J, Englert B-G, Sterpi N and Walther H 1994 *Phys. Rev. A* **49** 2962–85
- [88] Rempe G and Walther H 1990 *Phys. Rev. A* **42** 1650–5
- [89] Meystre P 1992 Cavity quantum optics and the quantum measurement process *Progress in Optics* vol 30, ed E Wolf (Amsterdam: North Holland) pp 261–355
- [90] Benson O, Raitzel G and Walther H 1994 *Phys. Rev. Lett.* **72** 3506–9
- [91] Raitzel G, Benson O and Walther H 1995 *Phys. Rev. Lett.* **75** 3446–9
- [92] Brattke S, Englert B-G, Varcoe B T H and Walther H 2000 *J. Mod. Opt.* **47** 2857–67
- [93] Bracher C 2000 private communication
- [94] Briegel H-J and Englert B-G 1993 *Phys. Rev. A* **47** 3311–29
- [95] Englert B-G, Löffler M, Benson O, Varcoe B T H, Weidinger M and Walther H 1998 *Fortschr. Phys.* **46** 897–926
- [96] Meystre P, Rempe G and Walther H 1988 *Opt. Lett.* **13** 1078–80
- [97] Zhu S-Y, Wang L Z and Fearn H 1991 *Phys. Rev. A* **44** 737–46
- [98] Varcoe B T H, Brattke S and Walther H (2004) *New J. Phys.* **6** 97

- [99] Brattke S, Varcoe B T H and Walther H 2001 *Opt. Express* **8** 131–44
- [100] Brattke S, Varcoe B T H and Walther H 2001 *Phys. Rev. Lett.* **86** 3534–7
- [101] Wiseman H and Milburn G 1993 *Phys. Rev. Lett.* **70** 548–51
- [102] Krause J, Scully M O and Walther H 1987 *Phys. Rev. A* **36** 4547–50
- [103] Bardoff P J, Mayr E and Schleich W P 1995 *Phys. Rev. A* **51** 4963–6
- [104] Scully M O, Walther H, Agarwal G S, Quang Tran and Schleich W 1991 *Phys. Rev. A* **44** 5992–6
- [105] Scully M O and Lamb W E Jr 1967 *Phys. Rev.* **159** 208–26  
See especially Sargent M, Scully M O and Lamb W E 1974 *Laser Physics* (Reading, MA: Addison-Wesley) p 292
- [106] Quang Tran, Agarwal G S, Bergou J, Scully M O, Walther H, Vogel K and Schleich W P 1993 *Phys. Rev. A* **48** 803–12
- [107] Vogel K, Schleich W P, Scully M O and Walther H 1993 *Phys. Rev. A* **48** 813–17
- [108] Bodendorf C T, Antesberger G, Kim M S and Walther H 1998 *Phys. Rev. A* **57** 1371–8
- [109] Kim M S, Antesberger G, Bodendorf C T and Walther H 1998 *Phys. Rev. A* **58** R65–8
- [110] Casagrande F, Ferraro A, Lulli A and Bonifacio R 2003 *Phys. Rev. Lett.* **90** 183601
- [111] Rauschenbeutel A, Nogues G, Osnaghi S, Bertet P, Brune M, Raimond J M and Haroche S 1999 *Phys. Rev. Lett.* **83** 5166–9
- [112] Raimond J M, Brune M and Haroche S 2001 *Rev. Mod. Phys.* **73** 565–82
- [113] Englert B-G and Walther H 2000 *Opt. Commun.* **179** 283–8
- [114] Löffler M, Englert B-G and Walther H 1996 *Appl. Phys. B* **63** 511–16
- [115] Englert B-G, Sterpi N and Walther H 1993 *Opt. Commun.* **100** 526–35
- [116] Meunier T, Gleyzes S, Maioli P, Auffeves A, Nogues G, Brune M, Raimond J M and Haroche S 2005 *Phys. Rev. Lett.* **94** 010401
- [117] Maioli P, Meunier T, Gleyzes S, Auffeves A, Nogues G, Brune M, Raimond J M and Haroche S 2005 *Phys. Rev. Lett.* **94** 113601
- [118] Raimond J M, Meunier T, Bertet P, Gleyzes S, Maioli P, Auffeves A, Nogues G, Brune M and Haroche S 2005 *J. Phys. B: At. Mol. Opt. Phys* **38** S535–50
- [119] Bertet P, Auffeves A, Maioli P, Osnaghi S, Meunier T, Brune M, Raimond J M and Haroche S 2002 *Phys. Rev. Lett.* **89** 200402
- [120] Lougovski P, Solano E, Zhang Z M, Walther H, Mach H and Schleich W P 2003 *Phys. Rev. Lett.* **91** 010401
- [121] Morigi G, Solano E, Englert B-G and Walther H 2002 *Phys. Rev. A* **65** 040102
- [122] Brune M, Hagley E, Dreyer J, Maître X, Maali A, Wunderlich C, Raimond J M and Haroche S 1996 *Phys. Rev. Lett.* **72** 4887–90
- [123] Englert B-G, Schwinger J and Scully M O 1990 Center-of-mass motion of masing atoms *New Frontiers in Quantum Electrodynamics and Quantum Optics* ed A O Barut (New York: Plenum) pp 513–19
- [124] Englert B-G, Schwinger J, Barut A O and Scully M O 1991 *Eur. Phys. Lett.* **14** 25–31
- [125] Haroche S, Brune M and Raimond J M 1991 *Eur. Phys. Lett.* **14** 19–24
- [126] See, e.g. Schleich W P 2001 *Quantum Optics in Phase Space* (Weinheim: Wiley-VCH)
- [127] Battocletti M and Englert B-G 1994 *J. Phys. II France* **4** 1939–53
- [128] Scully M O, Meyer G M and Walther H 1996 *Phys. Rev. Lett.* **76** 4144–7
- [129] Löffler M, Meyer G M, Schröder M, Scully M O and Walther H 1997 *Phys. Rev. A* **56** 4153–63
- [130] Meyer G M, Scully M O and Walther H 1997 *Phys. Rev. A* **56** 4142–52
- [131] See, e.g. Arimondo E, Philips W D and Strumia F (ed) 1992 *Laser Manipulations of Atoms and Ions* (Amsterdam: North-Holland)
- [132] Hansen W W and Richtmyer R D 1939 *J. Appl. Phys.* **10** 189–99
- [133] Schröder M, Vogel K, Schleich W P, Scully M O and Walther H 1997 *Phys. Rev. A* **56** 4164–74
- [134] Löffler M, Meyer G M and Walther H 1997 *Eur. Phys. Lett.* **40** 263–8
- [135] Löffler M, Meyer G M and Walther H 1998 *Eur. Phys. Lett.* **41** 593–8
- [136] Meyer G M, Löffler M and Walther H 1998 *Laser Phys.* **8** 649–52
- [137] Retamal J C, Solano E and Zagury N 1998 *Opt. Commun.* **154** 28–34
- [138] Benson O, Weidinger M, Löffler M and Walther H 1998 *Fortschr. Phys.* **46** 809–16
- [139] Hood C J, Lynn T W, Doherty A C, Parkins A S and Kimble H J 2000 *Science* **287** 1447–53
- [140] Miller R, Northup T E, Birnbaum K M, Boca A, Boozer A D and Kimble H J 2005 *J. Phys. B: At. Mol. Opt. Phys.* **38** S551–65
- [141] Childs J J, An K, Otteson M S, Dasari R R and Feld M S 1996 *Phys. Rev. Lett.* **77** 2901–4
- [142] Mabuchi H, Turchette Q A, Chapman M S and Kimble H J 1996 *Opt. Lett.* **21** 1393–5
- [143] Mu Y and Savage C 1992 *Phys. Rev. A* **49** 5944–54
- [144] Pellizzari T and Ritsch H 1994 *Phys. Rev. Lett.* **72** 3973–6

- [145] Horak P, Gheri K M and Ritsch H 1995 *Phys. Rev. A* **51** 3257–66
- [146] Meyer G M and Briegel H-J 1998 *Phys. Rev. A* **58** 3210–20
- [147] Jones B, Ghose S, Clemens J P, Rice P R and Pedrotti L M 1999 *Phys. Rev. A* **60** 3267–75
- [148] Kilin S Ya and Karlovich T B 2002 *JETP* **95** 805–19
- [149] McKeever J, Boca A, Boozer A D, Buck J R and Kimble H J 2003 *Nature* **425** 268–71
- [150] Boozer A D, Boca A, Buck J R, McKeever J and Kimble H J 2004 *Phys. Rev. A* **70** 023814
- [151] Pinkse P H W, Fischer T, Maunz P and Rempe G 2000 *Nature (London)* **404** 365–8
- [152] Rempe G 2000 *Phys. World* **13** 37–42
- [153] Münstermann P, Fischer T, Maunz P, Pinkse P W H and Rempe G 2000 *Phys. Rev. Lett.* **84** 4068–71
- [154] Doherty A C, Lynn T W, Hood C J and Kimble H J 2000 *Phys. Rev. A* **63** 013401
- [155] Pinkse P H W, Fischer T, Maunz P, Puppe T and Rempe G 2000 *J. Mod. Opt.* **47** 2769–87
- [156] Hennrich M, Legero T, Kuhn A and Rempe G 2000 *Phys. Rev. Lett.* **85** 4872–5
- [157] Fischer T, Maunz P, Puppe T, Pinkse P H W and Rempe G 2001 *New J. Phys.* **3** 11.1–11.20
- [158] Horak P, Ritsch H, Fischer T, Maunz P, Puppe T, Pinkse P H W and Rempe G 2002 *Phys. Rev. Lett.* **88** 043601
- [159] Fischer T, Maunz P, Pinkse P H W, Puppe T and Rempe G 2002 *Phys. Rev. Lett.* **88** 163002
- [160] Guthöhrlein G R, Keller M, Hayasaka K, Lange W and Walther H 2001 *Nature (London)* **414** 49–51
- [161] McKeever J, Buck J R, Boozer A D, Kuzmich A, Nägerl H-C, Stamper-Kurn D M and Kimble H J 2003 *Phys. Rev. Lett.* **90** 133602
- [162] Sauer J A, Fortier K M, Chang M S, Hamley C D and Chapman M S 2004 *Phys. Rev. A* **69** 051804
- [163] Maunz P, Puppe T, Schuster I, Syassen N, Pinkse P W H and Rempe G 2004 *Nature (London)* **428** 50–52
- [164] Ye J, Vernooij D W and Kimble H J 1999 *Phys. Rev. Lett.* **83** 4987–90
- [165] Kuhr S, Alt W, Schrader D, Müller M, Gomer V and Meschede D 2001 *Science* **293** 278–80
- [166] McKeever J, Boca A, Boozer A D, Miller R, Buck J R, Kuzmich A and Kimble H J 2004 *Science* **303** 1992–4
- [167] McKeever J, Boca A, Boozer A D, Buck J R and Kimble H J 2003 *Nature (London)* **425** 268–71
- [168] Nussmann S, Murr K, Hijkema M, Weber B, Kuhn A and Rempe G 2005 *Nature Phys.* **1** 122–6
- [169] Nussmann S, Hijkema M, Weber B, Rohde F, Rempe G and Kuhn A 2005 *Phys. Rev. Lett.* **95** 173602
- [170] Hood C J, Lynn T, Chapman M and Kimble H J 1998 *Phys. Rev. Lett.* **80** 4157–60
- [171] Maunz P, Puppe T, Schuster I, Syassen N, Pinkse P W H and Rempe G 2004 *Preprint* [quant-ph/045136](https://arxiv.org/abs/quant-ph/045136)
- [172] Boca A, Miller R, Birnbaum K M, Boozer A D, McKeever J and Kimble H J 2004 *Phys. Rev. Lett.* **93** 233603
- [173] Bennett C H and Brassard G 1984 *Proc. IEEE Int. Conf. on Computers, Systems, and Signal Processing (Bangalore, India)* (New York: IEEE) pp 175–9
- [174] Knill E, Laflamme R and Milburn G J 2001 *Nature (London)* **409** 46–52
- [175] Diedrich F and Walther H 1987 *Phys. Rev. Lett.* **58** 203–6
- [176] Basché T, Moerner W E, Orrit M and Talon H 1992 *Phys. Rev. Lett.* **69** 1516–19
- [177] Lounis B and Moerner W E 2000 *Nature (London)* **407** 491–3
- [178] Kurtsiefer C, Mayer S, Zarda P and Weinfurter H 2000 *Phys. Rev. Lett.* **85** 290–3
- [179] Brouri R, Beveratos A, Poizat J-P and Grangier P 2000 *Opt. Lett.* **25** 1294–6
- [180] Michler P *et al* 2000 *Science* **290** 2282–6
- [181] Santori C, Pelton M, Solomon G, Dale Y and Yamamoto Y 2001 *Phys. Rev. Lett.* **86** 1502–5
- [182] Moreau E *et al* 2001 *Appl. Phys. Lett.* **79** 2865–7
- [183] Yuan Z L *et al* 2002 *Science* **295** 102–5
- [184] Santori C, Fattal D, Vučković J, Solomon G and Yamamoto Y 2002 *Nature (London)* **419** 594–7
- [185] Cirac J I, Zoller P, Kimble H J and Mabuchi H 1997 *Phys. Rev. Lett.* **78** 3221–4
- [186] Parkins A S, Marte P, Zoller P and Kimble H J 1993 *Phys. Rev. Lett.* **71** 3095–8
- [187] Lange W and Kimble H J 2000 *Phys. Rev. A* **61** 63817
- [188] Law C K and Eberly J H 1996 *Phys. Rev. Lett.* **76** 1055–8
- [189] Kuhn A, Hennrich M, Bondo T and Rempe G 1999 *Appl. Phys. B* **69** 373–7
- [190] For a review, see Bergmann K and Shore B W 1995 *Molecular Dynamics and Stimulated Emission Pumping* ed H L Dai and R W Field (Singapore: World Scientific) pp 315–73
- [191] Kuhn A, Steuerwald S and Bergmann K 1998 *Eur. Phys. J. D* **1** 57–70
- [192] Kuhn A, Hennrich M and Rempe G 2002 *Phys. Rev. Lett.* **89** 067901
- [193] Smith A M and Gardiner C W 1990 *Phys. Rev. A* **41** 2730–48
- [194] Agarwal G S and Gupta S D 1990 *Phys. Rev. A* **42** 1737–41
- [195] Ginzl C, Briegel H-J, Martini U, Englert B-G and Schenzle A 1993 *Phys. Rev. A* **48** 732–8
- [196] Meyer G M, Briegel H-J and Walther H 1997 *Eur. Phys. Lett.* **37** 317–22
- [197] Löffler M, Meyer G M and Walther H 1997 *Phys. Rev. A* **55** 3923–30

- [198] Meyer G M, Löffler M and Walther H 1997 *Phys. Rev. A* **56** 1099–102
- [199] Meyer G M 1997 *Der Ionenfallenlaser: Einfluß von Dissipation und Pumpdynamik in mikroskopischen Vielniveausystemen* (Garching: MPQ Report 221)
- [200] Löffler M 1998 *Korrelationen und Bewegungsquantisierung im Ein-Atom-Maser und -Laser* (Garching: MPQ Report 235)
- [201] Keller M, Lange B, Hayasaka K, Lange W and Walther H 2004 *Nature* **431** 1075–8
- [202] Brendel J, Tittel W, Zbinden H and Gisin N 1999 *Phys. Rev. Lett.* **82** 2594–7
- [203] Duan L-M, Kuzmich A and Kimble H J 2003 *Phys. Rev. A* **67** 032305
- [204] see, e.g. Chang R K and Campillo A J 1996 Optical processes in microcavities *Advanced Series in Applied Physics* vol 3 (Singapore: World Scientific)
- [205] Vahala K 2004 Optical microcavities *Advanced Series in Applied Physics* vol 5 (Singapore: World Scientific)
- [206] Rarity J and Weisbuch C 1886 *Microcavities and Photonic Bandgaps* (Dordrecht: Kluwer)
- [207] Deveaud-Pledran B 2006 *The Physics of Semiconductor Microcavities* (New York: Wiley-VCH)